Design and Modification of Spinel Type Ferrites (MFe_2O_4, M = Zn & Ca) with Highly Efficient Photocatalytic Performance

Longfei Guo

Laboratory of Photon & Thermal Energy Conversion Materials
Division of Materials Science and Engineering
Graduate School of Engineering
Hokkaido University

September 2021

Table of Contents

Abstract

Organic pollutant in wastewater has become a severe environmental and safety problem. The semiconductor-based photocatalytic degradation is emerging as a high-efficiency and environmentally friendly approach because it only uses photocatalyst and solar energy. For the better utilization of visible light accounting for about 47.7% of solar energy, spinel type ferrites ($ZnFe_2O_4$ and $CaFe_2O_4$) with narrow bandgap (approximately 1.9 eV) are becoming emerging efficient photocatalysts. However, the serious photogenerated charges recombination limits the photocatalytic performance. To solve this problem, some modifications including forming heterojunction, fuel ratio adjustment, and shape modification have been carried out in this thesis.

In chapter 1, an overview of photocatalysis including photocatalytic dye degradation, water splitting, and CO_2 reduction was introduced first. Then a review on spinel type ferrite photocatalysts including common structure, and synthesis method was summarized. In the end, various modification methods of photocatalysts for enhanced photocatalytic properties were introduced.

In chapter 2, $ZnFe_2O_4/SnO_2$ (ZFO/SnO_2) composites were fabricated via a facile solution combustion synthesis (SCS) method for methylene blue (MB) degradation. The crystallite and morphology characterizations revealed that ZFO/SnO_2 composites have relatively small crystallite and particle size compared to pure ZFO. The introduction of SnO_2 remarkably improved the photocatalytic performance of pure ZFO catalyst. Specifically, ZFO-SnO_2 (10%) exhibited the highest photocatalytic degradation rate constant of 0.01970 min^{-1} in the composites, approximately 3.08 and 2.64 times higher than that of single ZFO (0.00640 min^{-1}) and SnO_2 (0.00747 min^{-1}), respectively. The band alignment analysis showed that the improvement of photocatalytic activity was due to the

improved charges separation efficiency in the ZFO/SnO_2 composite. ZFO-SnO_2 (10%) with H_2O_2 showed the highest photo-Fenton degradation rate constant of 0.05301 min^{-1} and could remove 95.2% of MB within 60 min under irradiation.

In chapter 3, $CaFe_2O_4$ (CFO) was fabricated by solution combustion synthesis (SCS) method using different fuels (urea and glucose) and fuel ratios (0.5, 1.0, and 1.5). CFO-Glucose shows a smaller crystallite size than CFO-Urea sample. CFO-1.0 presents the smallest crystallite size among various fuel ratios products. CFO-1.0 photocatalyst presents the best photocatalytic MB degradation with a kinetic constant of 0.00372 min^{-1} compared to CFO-Urea (0.00123 min^{-1}), CFO-0.5 (0.00176 min^{-1}), and CFO-2.0 (0.00249 min^{-1}). Based on the PL and XPS characterizations, the efficient photocatalytic performance of CFO-1.0 is attributed to the efficient charge separation and suitable photocatalyst surface state.

In chapter 4, $CaFe_2O_4$ nanorods (CFO NRs) and aggregated particles (CFO APs) were fabricated with and without the help of molten salt-assisted shape modification, respectively. CFO APs present inferior photocatalytic performance due to the plenty of grain boundaries which hinder photogenerated charges transfer and act as charge recombination sites. Molten salt-assisted modification can easily change the shape of CFO NRs and significantly suppresses the formation of grain boundaries, facilitating photogenerated charges separation and transfer for highly efficient photocatalytic degradation of methylene blue (MB). Surface state investigation indicates a decreased amount of unsuitable oxygen vacancies and defects in CFO NRs, which is beneficial in alleviating the recombination of photogenerated charges in CFO NRs. The CFO NRs show a ten-time increased kinetic constant of MB degradation from 0.0013 to 0.013 min^{-1} by virtue of the alleviative charge recombination.

In chapter 5, an overall conclusion of this dissertation was presented. Overall, this thesis performed a systematic research on the design and modification of spinel type ferrites with highly efficient photocatalytic performance. This work also shows forming semiconductor heterojunction structure with suitable band position is an efficient way to enhance the photocatalytic performance of photocatalysts. The fuel ratio of SCS has a great effect on the final product composition and photocatalytic performance. Meanwhile, molten salt-assisted shape modification of photocatalyst is also an efficient way to improve their photocatalytic properties.

Chapter 1 Introduction

1.1. Photocatalysis

With the increase of population and the development of industry, energy shortage and environmental pollution have become increasingly serious problems [1, 2]. Clean energy production by a sustainable approach is important for the future energy structure. Organic pollutant degradation by a novel method is also important for the sustainable development of cloth industry.

Since Fujishima and Honda first produced H_2 from TiO_2 photoelectrode through photoelectrochemical (PEC) water splitting in 1972 [3], the research on semiconductor-based photocatalytic reaction has attracted increasing attention. Specifically, the number of paper publications with the topic of photocatalytic obtained from Web of Science database has increased dramatically as shown in Figure 1.1. Solar energy as an inexhaustible clean energy can be used as an effective solution to energy and environmental problems. Compared with other methods, solar driven photocatalysis has plenty of advantages including cost-effective, environmentally friendly, without other energy source, highly effective, and high reusability. Photocatalytic reaction has been introduced to many fields including pollutants removal [4, 5], water splitting [6, 7], CO_2 reduction[8, 9], and selective organic synthesis [10, 11] and so on.

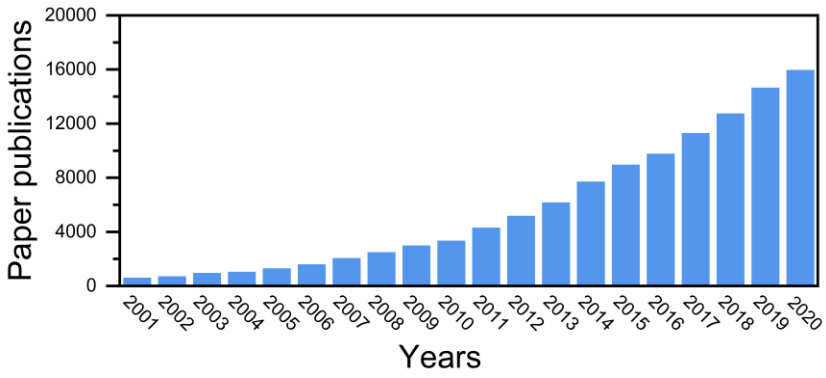

Figure 1.1 Paper publications with the topic of photocatalytic

Generally, photocatalysis occurs in the following three steps as shown in Figure 1.2: (1) absorption of photons with energy larger than that of band gap (E_g) to produce electron and hole pairs, (2) photoinduced charge pairs separation and transportation to the reactive sites on the surface, and (3) surface oxidation-reduction reaction by the photoinduced holes and electrons [12]. Therefore, there are the following principles when developing high-efficiency photocatalysts. Semiconductors with narrow bandgaps are more conductive to utilize more solar energy. Effective charges separation is also important to enhance photocatalytic performance.

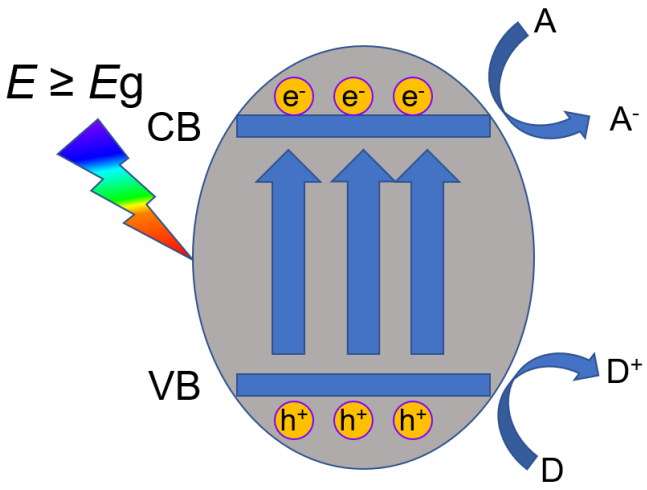

Figure 1.2 The generation, separation, and reaction of electron-hole pairs in a semiconductor.

1.1.1. Photocatalytic pollutant degradation

Due to the extensive use of organic dyes in the textile industry, a large amount of colored wastewater has become a serious problem, threatening environmental safety and human health [13, 14]. Chemical structures of common dyes are shown in Figure 1.3.

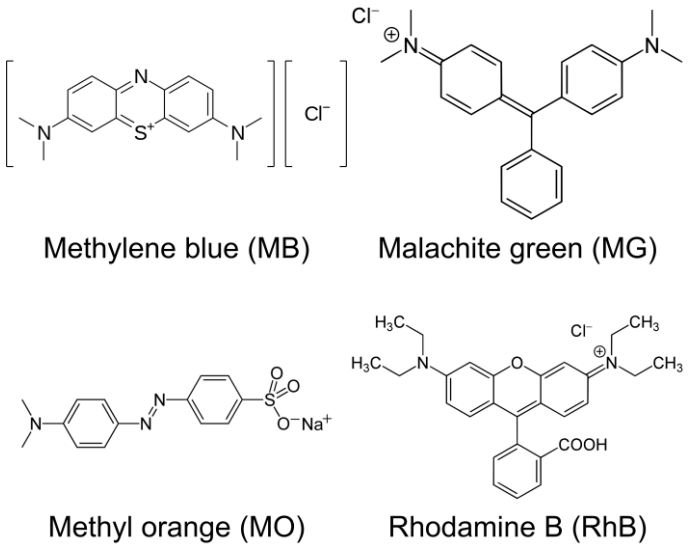

Figure 1.3 Common dyes chemical structure

Compared with many other methods to degrade organic pollutants, including biomass method, advanced oxidation method, and activated carbon, using photocatalysts to degrade organic dyes through photocatalytic method is a green and efficient method because it only uses environmentally stable photocatalyst and solar energy [15, 16].

Typically, when the semiconductor photocatalyst is under irradiation with the energy higher than the bandgap, a photogenerated electron (e^-) will excited from the valence band to conduction band, and there will be forming a photogenerated hole (h^+) in the valence band (equation (1.1)). After separation and diffusion, parts of photogenerated e^- and h^+ will transfer to the surface of semiconductor to take part in specific reaction. The photogenerated e^- at conduction band can be easily captured by dissolved oxygen in the solution to produce reactive superoxide free radical ($\cdot O_2^-$) through equation (1.2) [17]. Parts of will further react with hydrogen ion to form active free hydroxyl radical (·OH) and hydroxyl ion (H^+)as shown in equation (1.3). Meanwhile, h^+ on the surface of photocatalyst will react with water to form ·OH and H^+ according to equation (1.4). These active radicals can degrade the organic pollutant in the solution by photocatalytic reaction (equation (1.5)) [18].

$$\text{Semiconductor} + h\nu \rightarrow h^+ + e^- \quad (1.1)$$

$$2e^- + O_2 \rightarrow \cdot O_2^- \quad (1.2)$$

$$O_2^- + 2H^+ + 2e^- \rightarrow \cdot OH + OH^- \quad (1.3)$$

$$h^+ + H_2O \rightarrow \cdot OH + H^+ \quad (1.4)$$

$$\cdot OH/\cdot O_2^- + \text{Organic pollutant} \rightarrow \text{decomposed products} \quad (1.5)$$

1.1.2. Photocatalytic water splitting

Photocatalytic water splitting is a promising way to produce hydrogen from water under irradiation. A simple photocatalytic water splitting process with the help of co-catalysts can be illustrated in Figure 1.4 [19]. Common photocatalytic water splitting reaction can be presented as the following equations:

$$\text{Reduction reaction: } 2H_2O + 2e^- \rightarrow H_2 + 2OH^- \quad (1.6)$$

$$\text{Oxidation reaction: } H_2O + 2h^+ \rightarrow 2H^+ + 1/2O_2 \quad (1.7)$$

$$\text{Overall reaction: } H_2O \rightarrow H_2 + 1/2O_2\ (E^0 = 1.23\ V) \quad (1.8)$$

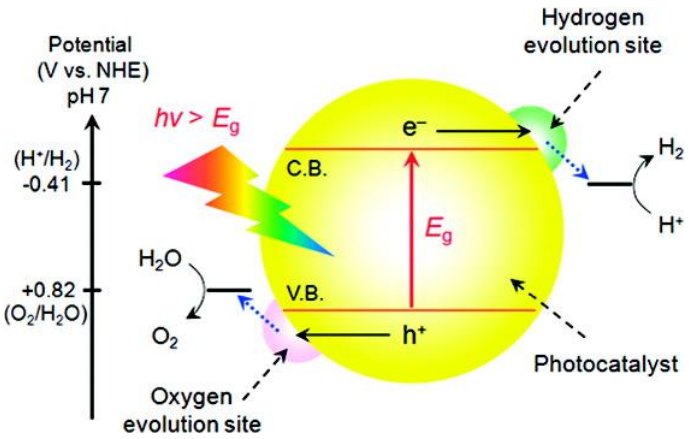

Figure 1.4 Schematic energy diagrams of photocatalytic water splitting [19]

1.1.3. Photocatalytic CO_2 reduction

The photocatalytic CO_2 reduction into valuable hydrocarbon fuels is a promising path to solve the increasing carbon dioxide emissions and energy shortage crisis. Due to the

diversity of reduction products, the photocatalytic CO_2 reduction still faces huge challenges. The standard potentials of CO_2 reduction to different products are summarized as below (vs. normal hydrogen electrode, NHE), pH = 0: [20]

$$CO_2 + 2H^+ + 2e^- \rightarrow HCOOH \ (E^0 = -0.2 \text{ V}) \quad (1.9)$$

$$CO_2 + 2H^+ + 2e^- \rightarrow CO + H_2O \ (E^0 = -0.12 \text{ V}) \quad (1.10)$$

$$CO_2 + 4H^+ + 4e^- \rightarrow HCHO + H_2O \ (E^0 = 0.07 \text{ V}) \quad (1.11)$$

$$CO_2 + 6H^+ + 6e^- \rightarrow CH_3OH + H_2O \ (E^0 = 0.03 \text{ V}) \quad (1.12)$$

$$CO_2 + 8H^+ + 8e^- \rightarrow CH_4 + 2H_2O \ (E^0 = 0.17 \text{ V}) \quad (1.13)$$

1.2. Spinel type ferrite photocatalysts

Titanium oxide, as the most widely studied photocatalyst, exhibits excellent photocatalytic performance in many fields [21-24]. Nevertheless, TiO_2 with wide bandgap (3.2 eV) only shows high photocatalytic efficiency under ultraviolet (UV) light irradiation [25]. As shown in Figure 1.5, UV light irradiation only accounts for 4.6% of the solar spectrum, but visible light irradiation accounts for 47.7% of the solar spectrum [26]. Therefore, it is necessary to develop visible-light-active and property stable semiconductor photocatalysts with narrow bandgap to take full advantage of solar irradiation. Spinel type ferrites are suitable photocatalysts with wide photocatalytic applications due to their narrow optical bandgap (<2.2 eV), low cost, and superior durability [27]. They are effective photocatalysts for organic pollutant degradation [28, 29] and water splitting [30]. However, their inferior charge separation efficiency, low electrical conductivity, and limited synthesis methods limit the further development of spinel type ferrites photocatalysts. Therefore, it is necessary to review the spinel type ferrites photocatalysts and find other modification methods.

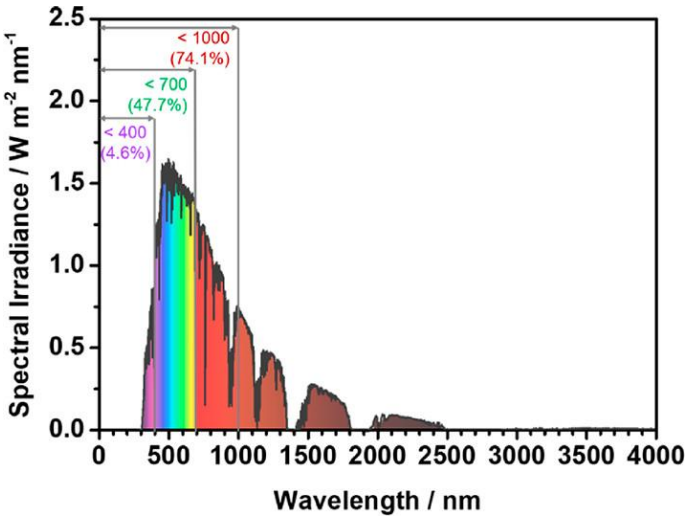

Figure 1.5 AM 1.5 G solar spectrum based on the ASTM G173-03 reference spectrum [26].

1.2.1. The structure of spinel type ferrites

Spinel type ferrites have a general formula $M_xFe_{3-x}O_4$, where M refers to the divalent metal (M = Ni, Co, Zn, Ca, Mg, Mn, and so on). They always show magnetic properties, which are significantly important for the recycle after photocatalytic application process. They are always used as photocatalysts for the photocatalytic degradation of organic pollutants [31, 32]. The common crystal structures of spinel type ferrites are shown in Figure 1.6. The structure of spinel ferrites is derived from the mineral spinel, $MgAl_2O_4$, by replacing the trivalent Al ion with Fe and Mg ion by other divalent metal ions. In normal spinel structure (Figure 1.6(a)), all M ions are in the tetrahedral sites, and all Fe ions are in the octahedral sites. Samples with normal spinel structure include $ZnFe_2O_4$, $CdFe_2O_4$, and so on. When few parts of Fe ions occupy the tetrahedral sites, the structure is called as inverse spinel structure as shown in Figure 1.6(b). Some other spinel ferrites, such as $CaFe_2O_4$ [33], $MgFe_2O_4$ [34], and $BaFe_2O_4$ [35], present orthorhombic structure as shown in Figure 1.6(c). Spinel ferrites photocatalysts always show super photo and chemical stability in aqueous systems [36]. Spinel ferrite like $ZnFe_2O_4$ is very stable in alkaline

solution system. Spinel ferrite like $CaFe_2O_4$ is very stable in acidic solution system.

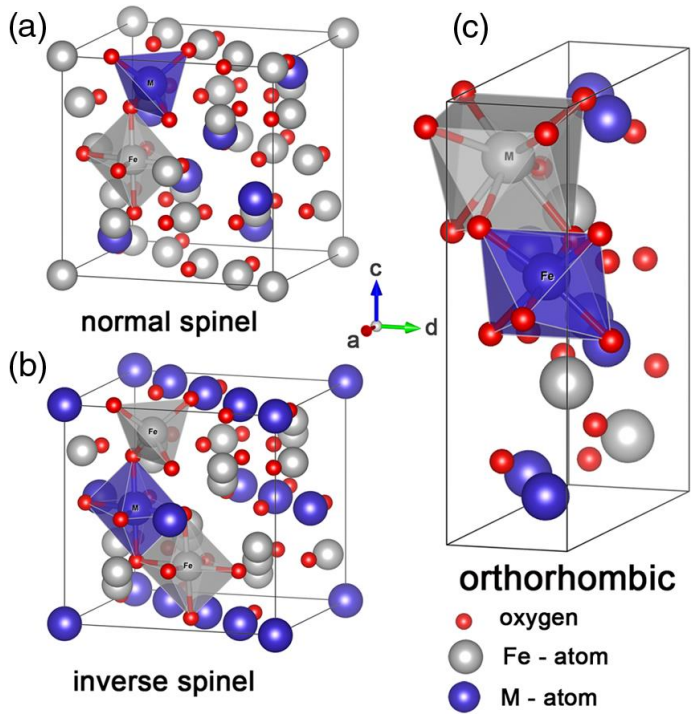

Figure 1.6 Crystal structures of spinel ferrites: (a) normal spinel, (b) inverse spinel, and (c) orthorhombic each demonstrating the three crystallographic sites [37].

Most of spinel ferrites are narrow bandgap semiconductors. Their band positions are shown in Figure 1.7.

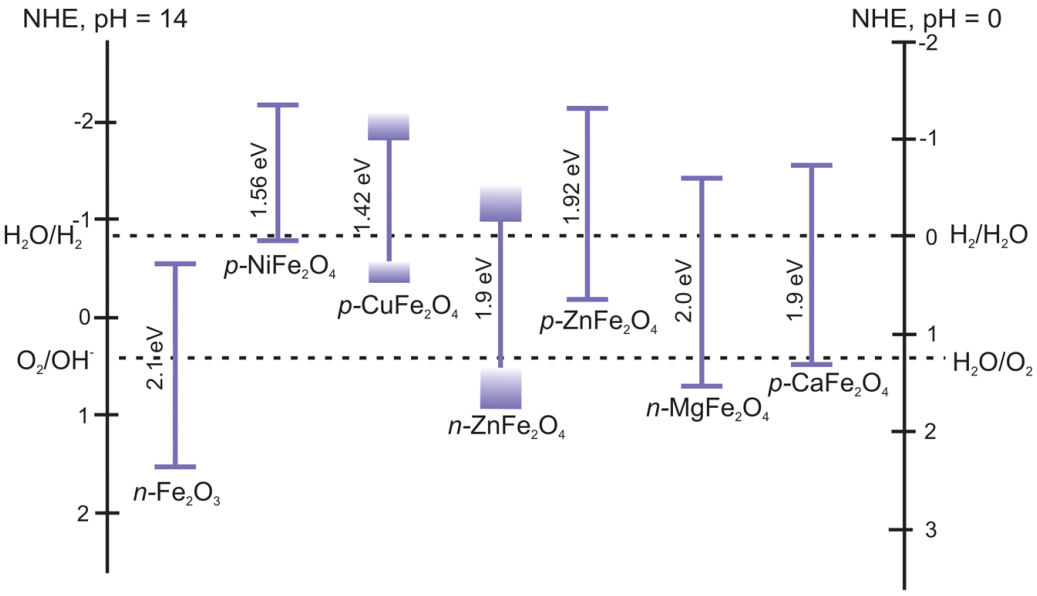

Figure 1.7 Band positions of spinel ferrites [37].

1.2.2. Synthesis methods

A number of different synthesis methods including solution combustion synthesis, thermal methods, and co-precipitation are used to fabricate spinel ferrite catalysts.

Solution combustion synthesis (SCS) is a facile method to produce spinel ferrite product using metal nitrates and fuels (such as urea, glycine, glucose, and citric acid). Some experimental factors such as fuel ratio, fuel kind, and calcination temperature have great effect on the final product [38, 39]. SCS method usually has energy saving, high efficiency, and high output characteristics. However, the products obtained by SCS method usually present aggregated morphology by multiple nanoparticles [40].

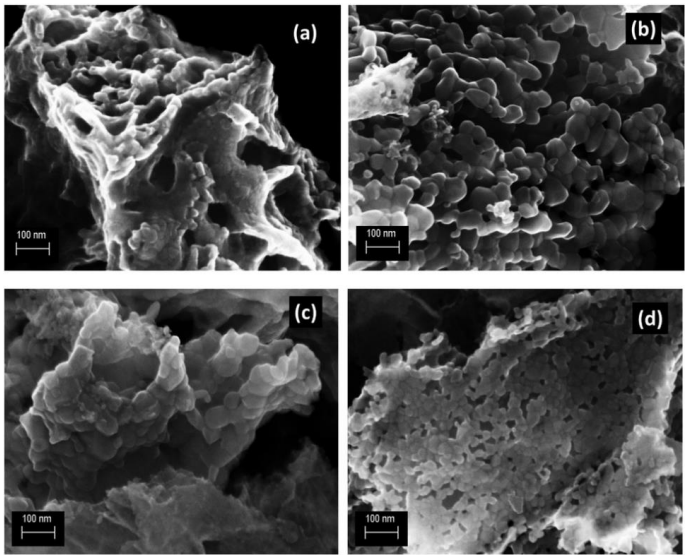

Equation 1.14 FESEM images of (a) $CoFe_2O_4$, (b) $Co_{0.5}Mn_{0.5}Fe_2O_4$, (c) $Co_{0.5}Ni_{0.5}Fe_2O_4$, and (d) $Co_{0.5}Zn_{0.5}Fe_2O_4$ [40]

The thermal synthesis methods for ferrites photocatalysts include hydrothermal, solvothermal, seed-hydrothermal, mechano-thermal, and microwave. In each method, an iron salt is often used, usually $Fe(NO_3)_3$ or $FeCl_3$, and another metal salt is used, such as $M(NO_3)_2$, MSO_4, or MCl_2. These salts are usually first dissolved in water or other solvents, and the pH is adjusted to an appropriate range according to different metal salt precursors. Then the mixed solution is placed in the reactor, usually at a temperature lower than 200

^{o}C and heated for 12-24 h. Finally, after cooling to room temperature, it is centrifuged and dried in a drying oven at approximately 85 ^{o}C overnight. The products obtained by thermal synthesis method usually show specific nano morphology. A yolk-shell $ZnFe_2O_4$ in was fabricated by solvothermal synthesis method using $Zn(NO_3)_2$, $Fe(NO_3)_3$, and dopamine as raw materials [41].

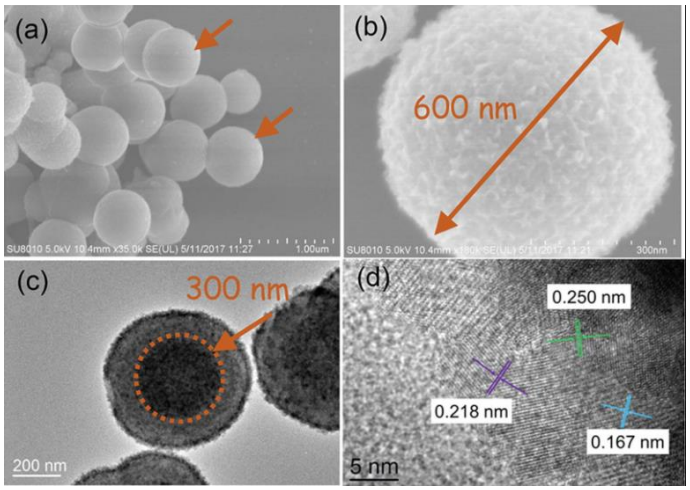

Equation 1.15 SEM images (a, b), TEM images (c), high resolution TEM image (d) of CN-$ZnFe_2O_4$ [41]

Co-precipitation method to prepare ferrites are similar to thermal methods. Fe(III) and metal salts are dissolved in water along with a surfactant, oleic acid, under stirring and gentle heating. The pH of the solution is adjusted to 7-10 to fabricate precipitation products usually with small size. The synthesized precipitation product is centrifuged and washed with water and then dried at 80-100 ^{o}C. Further, the as-synthesized product can be heated at different temperature and different heating rates to form product with different morphologies. [42, 43].

1.3. Modification of photocatalysts for enhanced performance

Common photoinduced formation of an electron-hole pair in a semiconductor with possible decay paths as shown in Figure 1.8 [44]. Generally, to overcome these decay paths, some modification methods have been introduced in photocatalysts for enhanced

performance, such as forming heterojunction, co-catalysts, doping, plasma, photodeposition, and flux modification.

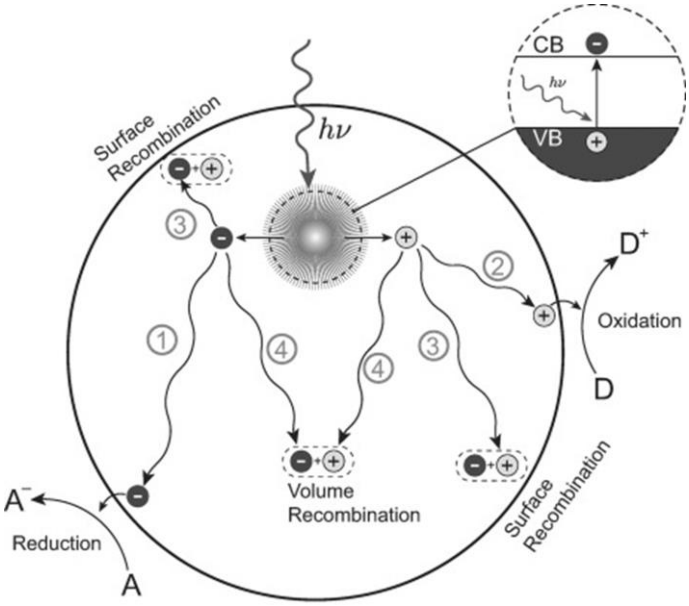

Figure 1.8 Schematic illustration of the basic mechanism of a semiconductor photocatalytic process. A = electron acceptor, D = electron donor. Pathways 1 and 2: donation of the carrier to the acceptor reactants on the surface, which results in the desired redox reactions. Pathway 3: carriers recombination occurs on the surface of a semiconductor. Pathway 4: carriers recombination occurs in the bulk of the semiconductor [44].

1.3.1. Heterojunction

The formation of heterojunction can cause band bending and internal electric field to promote effective separation of charges in space so that more photo-generated charges participate in the photocatalytic reaction. Generally, the types of semiconductor heterojunctions can be divided into four types, such as Schottky junction, Type I, Type II and Type III heterojunctions as shown in Figure 1.9. Among these heterojunctions, only Schottky junction and Type II can effectively improve the photo-generated charge separation rate and prolong the photo-generated charge lifetime.

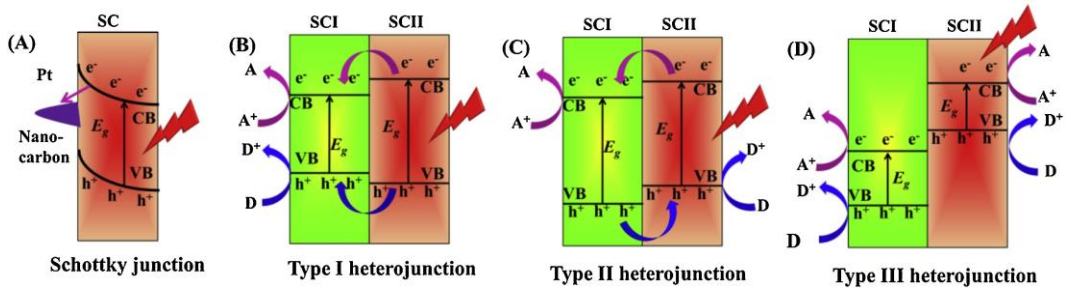

Figure 1.9 Spatial charge-separation mechanisms for four different types of semiconductor heterojunctions: (A) Schottky junction, (B) Type I, (C) Type II, and (D) Type III heterojunctions [45].

Up to now, the combination of spinel ferrites-based semiconductors, such as $NiFe_2O_4$/g-C_3N_4 [46], CdS/$NiFe_2O_4$ [47], PdO/$SrFe_2O_4$ [48], $CaFe_2O_4$/g-C_3N_4 [49], ZnO/$ZnFe_2O_4$ [50], and $CoFe_2O_4$-g-C_3N_4 [51], have been constructed for enhanced photocatalytic performance.

1.3.2. Doping

Generally, doping of exotic elements can enhance the visible light harvesting ability because of the formation of localized or delocalized electronic states. Additionally, the introduction of multiple impurities leads to disorder effects and thus form tail states (Urbach tails) in the electronic structure [52]. Jannat reported the nickel doped zinc ferrite ($ZnFe_{2-x}Ni_xO_4$) nano-composites were synthesized using a facile auto-combustion method using glycine as fuel for efficient methylene blue degradation [53].

1.4. Objectives and dissertation organization

In this dissertation, some modification methods have been applied to enhance the photocatalytic performance of ZFO and CFO semiconductor photocatalysts. **Chapter 1** gives basic introduction about photocatalysis, spinel type ferrite photocatalysts, and common modification methods for enhanced photocatalytic performance. **Chapter 2** introduces SnO_2 semiconductor to form a ZFO/SnO_2 heterojunction for enhanced photocatalytic MB degradation. **Chapter 3** shows the effect of fuel kinds and fuel ratios on

photocatalytic activity of CFO. **Chapter 4** introduces a molten salt-assisted shape modification method to enhance the photocatalytic performance of CFO NRs. **Chapter 5** gives some conclusions about this thesis and some future prospects.

References

1. M. R. Hoffmann, S. T. Martin, W. Choi, et al. Environmental applications of semiconductor photocatalysis. *Chemical Reviews*. **1995** (1) 69-96.
2. H. Tong, S. Ouyang, Y. Bi, et al. Nano-photocatalytic materials: Possibilities and challenges. *Advanced Materials*. **2012** (2) 229-251.
3. A. Fujishima and K. Honda. Electrochemical photolysis of water at a semiconductor electrode. *Nature*. **1972** (5358) 37-38.
4. C.-C. Wang, J.-R. Li, X.-L. Lv, et al. Photocatalytic organic pollutants degradation in metal-organic frameworks. *Energy & Environmental Science*. **2014** (9) 2831-2867.
5. M. N. Chong, B. Jin, C. W. K. Chow, et al. Recent developments in photocatalytic water treatment technology: A review. *Water Research*. **2010** (10) 2997-3027.
6. X. Li, J. Yu, J. Low, et al. Engineering heterogeneous semiconductors for solar water splitting. *Journal of Materials Chemistry A*. **2015** (6) 2485-2534.
7. X. Chen, S. Shen, L. Guo, et al. Semiconductor-based photocatalytic hydrogen generation. *Chemical Reviews*. **2010** (11) 6503-6570.
8. X. Li, J. Wen, J. Low, et al. Design and fabrication of semiconductor photocatalyst for photocatalytic reduction of CO_2 to solar fuel. *Science China Materials*. **2014** (1) 70-100.
9. J. Low, J. Yu, and W. Ho. Graphene-based photocatalysts for CO_2 reduction to solar fuel. *The Journal of Physical Chemistry Letters*. **2015** (21) 4244-4251.
10. H. Kisch. Semiconductor photocatalysis-Mechanistic and synthetic aspects. *Angewandte Chemie International Edition*. **2013** (3) 812-847.
11. X. Lang, X. Chen, and J. Zhao. Heterogeneous visible light photocatalysis for selective organic transformations. *Chemical Society Reviews*. **2014** (1) 473-486.

12. A. Naseri, M. Samadi, A. Pourjavadi, et al. Graphitic carbon nitride (g-C_3N_4)-based photocatalysts for solar hydrogen generation: Recent advances and future development directions. *Journal of Materials Chemistry A*. **2017** (45) 23406-23433.
13. M. A. Brown and S. C. De Vito. Predicting azo dye toxicity. *Critical Reviews in Environmental Science and Technology*. **1993** (3) 249-324.
14. S. A. Hassanzadeh-Tabrizi, M. M. Motlagh, and S. Salahshour. Synthesis of ZnO/CuO nanocomposite immobilized on γ-Al_2O_3 and application for removal of methyl orange. *Applied Surface Science*. **2016** 237-243.
15. H. Anwer, A. Mahmood, J. Lee, et al. Photocatalysts for degradation of dyes in industrial effluents: Opportunities and challenges. *Nano Research*. **2019** (5) 955-972.
16. H. Wang, L. Zhang, Z. Chen, et al. Semiconductor heterojunction photocatalysts: Design, construction, and photocatalytic performances. *Chemical Society Reviews*. **2014** (15) 5234-5244.
17. M. A. Henderson. A surface science perspective on TiO_2 photocatalysis. *Surface Science Reports*. **2011** (6) 185-297.
18. T. Lee, E. K. Jeon, and B.-S. Kim. Mussel-inspired nitrogen-doped graphene nanosheet supported manganese oxide nanowires as highly efficient electrocatalysts for oxygen reduction reaction. *Journal of Materials Chemistry A*. **2014** (17) 6167-6173.
19. K. Maeda and K. Domen. Photocatalytic water splitting: Recent progress and future challenges. *The Journal of Physical Chemistry Letters*. **2010** (18) 2655-2661.
20. E. Fujita. Photochemical carbon dioxide reduction with metal complexes. *Coordination Chemistry Reviews*. **1999** 373-384.

21. R. Daghrir, P. Drogui, and D. Robert. Modified TiO_2 for environmental photocatalytic applications: A review. *Industrial & Engineering Chemistry Research*. **2013** (10) 3581-3599.
22. L.-L. Tan, S.-P. Chai, and A. R. Mohamed. Synthesis and applications of graphene-based TiO_2 photocatalysts. *ChemSusChem*. **2012** (10) 1868-1882.
23. C. S. Uyguner Demirel, N. C. Birben, and M. Bekbolet. A comprehensive review on the use of second generation TiO_2 photocatalysts: Microorganism inactivation. *Chemosphere*. **2018** 420-448.
24. V. Etacheri, C. Di Valentin, J. Schneider, et al. Visible-light activation of TiO_2 photocatalysts: Advances in theory and experiments. *Journal of Photochemistry and Photobiology C: Photochemistry Reviews*. **2015** 1-29.
25. Y. Yang, L.-C. Yin, Y. Gong, et al. An unusual strong visible-light absorption band in red anatase TiO_2 photocatalyst induced by atomic hydrogen-occupied oxygen vacancies. *Advanced Materials*. **2018** (6) 1704479.
26. Q. Wang and K. Domen. Particulate photocatalysts for light-driven water splitting: Mechanisms, challenges, and design strategies. *Chemical Reviews*. **2020** (2) 919-985.
27. T. Vijayaraghavan, S. P. Suriyaraj, R. Selvakumar, et al. Rapid and efficient visible light photocatalytic dye degradation using AFe_2O_4 (A = Ba, Ca and Sr) complex oxides. *Materials Science and Engineering: B*. **2016** 43-50.
28. H. Y. He. Photocatalytic degradations of dyes on magnetically separable $Ni_{1-x}Co_xFe_2O_4$ nanoparticles synthesized by a hydrothermal process. *Particulate Science and Technology*. **2016** (2) 143-151.

29. K. K. Kefeni, B. B. Mamba, and T. A. M. Msagati. Application of spinel ferrite nanoparticles in water and wastewater treatment: A review. *Separation and Purification Technology*. **2017** 399-422.
30. J. L. Domínguez-Arvizu, J. A. Jiménez-Miramontes, J. M. Salinas-Gutiérrez, et al. Study of $NiFe_2O_4$ nanoparticles optical properties by a six-flux radiation model towards the photocatalytic hydrogen production. *International Journal of Hydrogen Energy*. **2019** (24) 12455-12462.
31. A. L. Tiano, G. C. Papaefthymiou, C. S. Lewis, et al. Correlating size and composition-dependent effects with magnetic, mössbauer, and pair distribution function measurements in a family of catalytically active ferrite nanoparticles. *Chemistry of Materials*. **2015** (10) 3572-3592.
32. D. S. Mathew and R.-S. Juang. An overview of the structure and magnetism of spinel ferrite nanoparticles and their synthesis in microemulsions. *Chemical Engineering Journal*. **2007** (1) 51-65.
33. R. A. Candeia, M. I. B. Bernardi, E. Longo, et al. Synthesis and characterization of spinel pigment $CaFe_2O_4$ obtained by the polymeric precursor method. *Materials Letters*. **2004** (5) 569-572.
34. D. Levy, V. Diella, M. Dapiaggi, et al. Equation of state, structural behaviour and phase diagram of synthetic $MgFe_2O_4$, as a function of pressure and temperature. *Physics and Chemistry of Minerals*. **2004** (2) 122-129.
35. R. A. Candeia, M. A. F. Souza, M. I. B. Bernardi, et al. Monoferrite $BaFe_2O_4$ applied as ceramic pigment. *Ceramics International*. **2007** (4) 521-525.
36. E. Casbeer, V. K. Sharma, and X.-Z. Li. Synthesis and photocatalytic activity of ferrites under visible light: A review. *Separation and Purification Technology*. **2012** 1-14.

37. H. T. Dereje, D. Ralf, C. U. Anna, et al. Photoelectrochemical and theoretical investigations of spinel type ferrites ($M_xFe_{3-x}O_4$) for water splitting: A mini-review. *Journal of Photonics for Energy*. **2016** (1) 1-25.

38. Y. Yang, Y. Jiang, Y. Wang, et al. Influences of sintering atmosphere on the formation and photocatalytic property of $BaFe_2O_4$. *Materials Chemistry and Physics*. **2007** (2) 154-156.

39. S. Xu, D. Feng, and W. Shangguan. Preparations and photocatalytic properties of visible-light-active zinc ferrite-doped TiO_2 photocatalyst. *The Journal of Physical Chemistry C*. **2009** (6) 2463-2467.

40. P. Bera, R. V. Lakshmi, B. H. Prakash, et al. Solution combustion synthesis, characterization, magnetic, and dielectric properties of $CoFe_2O_4$ and $Co_{0.5}M_{0.5}Fe_2O_4$ (M = Mn, Ni, and Zn). *Physical Chemistry Chemical Physics*. **2020** (35) 20087-20106.

41. J. Li, X. Li, X. Chen, et al. In situ construction of yolk-shell zinc ferrite with carbon and nitrogen co-doping for highly efficient solar light harvesting and improved catalytic performance. *Journal of Colloid and Interface Science*. **2019** 91-102.

42. J. Wolska, K. Przepiera, H. Grabowska, et al. $ZnFe_2O_4$ as a new catalyst in the C-methylation of phenol. *Research on Chemical Intermediates*. **2008** (1) 43-51.

43. Z. Zhu, X. Li, Q. Zhao, et al. Porous "brick-like" $NiFe_2O_4$ nanocrystals loaded with Ag species towards effective degradation of toluene. *Chemical Engineering Journal*. **2010** (1) 64-70.

44. S. N. Habisreutinger, L. Schmidt-Mende, and J. K. Stolarczyk. Photocatalytic reduction of CO_2 on TiO_2 and other semiconductors. *Angewandte Chemie International Edition*. **2013** (29) 7372-7408.

45. J. Wen, J. Xie, X. Chen, et al. A review on g-C_3N_4-based photocatalysts. *Applied Surface Science*. **2017** 72-123.

46. Y. Liu, Y. Song, Y. You, et al. $NiFe_2O_4$/g-C_3N_4 heterojunction composite with enhanced visible-light photocatalytic activity. *Journal of Saudi Chemical Society*. **2018** (4) 439-448.

47. C. Singh, Devika, R. Malik, et al. CdS nanorod-MFe_2O_4 (M = Zn, Co and Ni) nanocomposites: A heterojunction synthesis strategy to mitigate environmental deterioration. *RSC Advances*. **2015** (108) 89327-89337.

48. M. u. Haq, S. U. Din, S. Khan, et al. Ultrasensitive sensors based on PdO@$SrFe_2O_4$ nanosphere-modified fibers for real-time monitoring of ethanol gas. *ACS Applied Electronic Materials*. **2021** (4) 1732-1746.

49. S. Vadivel, D. Maruthamani, A. Habibi-Yangjeh, et al. Facile synthesis of novel $CaFe_2O_4$/g-C_3N_4 nanocomposites for degradation of methylene blue under visible-light irradiation. *Journal of Colloid and Interface Science*. **2016** 126-136.

50. R. Appiah-Ntiamoah, A. F. Baye, B. T. Gadisa, et al. In-situ prepared ZnO-$ZnFe_2O_4$ with 1-D nanofiber network structure: An effective adsorbent for toxic dye effluent treatment. *Journal of Hazardous Materials*. **2019** 459-467.

51. S. Renukadevi and A. P. Jeyakumari. A one-pot microwave irradiation route to synthesis of $CoFe_2O_4$-g-C_3N_4 heterojunction catalysts for high visible light photocatalytic activity: Exploration of efficiency and stability. *Diamond and Related Materials*. **2020** 108012.

52. H. Yaghoubi, Z. Li, Y. Chen, et al. Toward a visible light-driven photocatalyst: The effect of midgap-states-induced energy gap of undoped TiO_2 nanoparticles. *ACS Catalysis*. **2015** (1) 327-335.

53. J. Hammouche, M. Gaidi, S. Columbus, et al. Enhanced photocatalytic performance of zinc ferrite nanocomposites for degrading methylene blue: Effect of nickel doping concentration. *Journal of Inorganic and Organometallic Polymers and Materials*. **2021**

Chapter 2 Facile Synthesis of $ZnFe_2O_4/SnO_2$ Composites for Efficient Photocatalytic Degradation of Methylene Blue

2.0. Brief summary

In this chapter, $ZnFe_2O_4/SnO_2$ (ZFO/SnO_2) composites were fabricated via a facile solution combustion synthesis (SCS) method for methylene blue (MB) degradation. The crystallite and morphology characterizations revealed that ZFO/SnO_2 composites have relatively small crystallite and particle size compared to pure ZFO. The introduction of SnO_2 remarkably improved the photocatalytic performance of pure ZFO catalyst. Specifically, ZFO-SnO_2 (10%) exhibited the highest photocatalytic degradation rate constant of 0.01970 min^{-1} in the composites, approximately 3.08 and 2.64 times higher than that of single ZFO (0.00640 min^{-1}) and SnO_2 (0.00747 min^{-1}), respectively. The band alignment analysis showed that the improvement of photocatalytic activity was due to the improved charges separation efficiency in the ZFO/SnO_2 composite. ZFO-SnO_2 (10%) with H_2O_2 showed the highest photo-Fenton degradation rate constant of 0.05301 min^{-1} and could remove 95.2% of MB within 60 min under irradiation.

2.1. Introduction

In the last few decades, organic dye aqueous solution pollution treatment has been receiving great attention due to the increasing industry wastewater in leather, textile, and food industries [1, 2]. Conventional methods such as physical adsorption [3], biodegradation [4, 5], membrane separation [6], Fenton reaction [7], and photocatalytic degradation [8, 9] have been developed as promising technologies for organic dyes degradation. Among them, Fenton reaction and semiconductor photocatalytic degradation can be operated under mild conditions. H_2O_2 in the Fenton reaction can be activated to produce ·OH species with high reactivity and ferrous ion (Fe^{2+}) can be oxidized to ferric ion (Fe^{3+}) [10]. However, the sluggish recycling from Fe^{3+} to Fe^{2+} often limits the Fenton reaction process of catalysts [11]. Generally, the photocatalytic degradation of organic dye

pollutants includes three main reaction processes: transition of electron and forming of hole, separation of charge carrier pairs and diffusion to the semiconductor/solution interface, and degradation of dye molecules with reactive radicals on the surface [9]. However, the photocatalytic degradation performance of semiconductor was limited by some intrinsic properties of catalysts, such as narrow absorption range, lower charges separation efficiency and fast charges recombination in the bulk, consumption of charges on the surface [12]. As mentioned above, single Fenton reaction or photocatalytic process for dye degradation cannot meet the needs of practical application. The Fenton reaction process can be promoted by light irradiation due to the increasing of ·OH and Fe^{2+} from the reaction of Fe^{3+} and OH^-, which is called the photo-Fenton reaction [13]. Meanwhile, photogenerated electron will be captured by H_2O_2 in the photo-Fenton reaction, improving separation efficiency of charge carriers. Thus, these synergistic effects will lead to enhanced dye degradation efficiency in the photocatalyst/H_2O_2 system under irradiation.

Recently, spinel ferrites (MFe_2O_4) have drawn increasing attention by virtue of their suitable bandgap and remarkable durability under irradiation for solar fuel energy conversion and solar-induced environmental remediation [14, 15]. Among them, $ZnFe_2O_4$ (ZFO) is a promising n-type semiconductor catalyst for dye photocatalytic degradation due to its suitable bandgap (approximately 1.9 eV), superior durability, and natural abundance [16]. Unfortunately, fast charge recombination often limited its practical application [17]. Forming semiconductor composites with suitable band levels is a reliable and promising strategy due to its enhanced photogenerated charge separation efficiency. Recently, a lot of work has been investigated on ZFO/semiconductor composites, such as ZFO/ZnO [18], ZFO/Fe_2O_3 [19], ZFO/TiO_2 [20], ZFO/C_3N_4 [21], ZFO/$La_2O_2CO_3$ [22], and ZFO/$SnFe_2O_4$ [23]. Recently, a hollow microtubes SnO_2 has been fabricated by electrospinning with a

highly photocatalytic property for dyes degradation [24]. Some studies show that SnO_2 as a superior electron acceptor semiconductor [25] can form a composite with other semiconductors to achieve high photocatalytic activity like CdS/SnO_2 [26], ZnO/SnO_2 [27], TiO_2/SnO_2 [28]. However, there are few researchers studied the photocatalytic activity of ZFO/SnO_2 composites.

In this chapter, ZFO/SnO_2 composites were fabricated through a solution combustion synthesis (SCS) method. The photocatalytic degradation performance of catalysts was investigated through degradation of methylene blue (MB) aqueous solution under irradiation. The photo-Fenton degradation of MB was also studied under H_2O_2 condition. The optimization amount of SnO_2 in ZFO/SnO_2 composites was also investigated for MB photocatalytic degradation. The charge separation and transfer over ZFO/SnO_2 composite and possible MB degradation mechanism were proposed.

2.2. Experimental

2.2.1. Materials

Commercially available iron nitrate enneahydrate ($Fe(NO_3)_3 \cdot 9H_2O$, 99.0%), zinc nitrate hexahydrate ($Zn(NO_3)_2 \cdot 6H_2O$, 99.0%), urea ($CO(NH_2)_2$, 99.0%), tin chloride pentahydrate ($SnCl_4 \cdot 5H_2O$, 98.0%), and ammonium nitrate (NH_4NO_3, 99.0%) were directly used without further purification.

2.2.2. Synthesis of ZFO/SnO_2 composites

Pre-experiments were performed to show the effect of SCS precursor on final product composition. Solution precursor and gel precursor samples are prepared according to Figure 2.1. Stoichiometric number of reagents according to Equations (2.1) were dissolved with deionized water (30 mL) and stirred for 30 min to form transparent solution precursor. Then put it directly into the furnace, heat it up to 500 ^oC from room temperature, keep it

for 10 minutes, and cool it down to room temperature in the furnace. After carefully grinding, it is heated at 1000 ºC for 2 h. The final product is named as S500ZFO. Unlike the process of preparing solution precursor samples, gel precursor samples synthesis process also needs additional gel forming process before heating to 500 ºC. Then perform the same process and the final produce is named as G500ZFO.

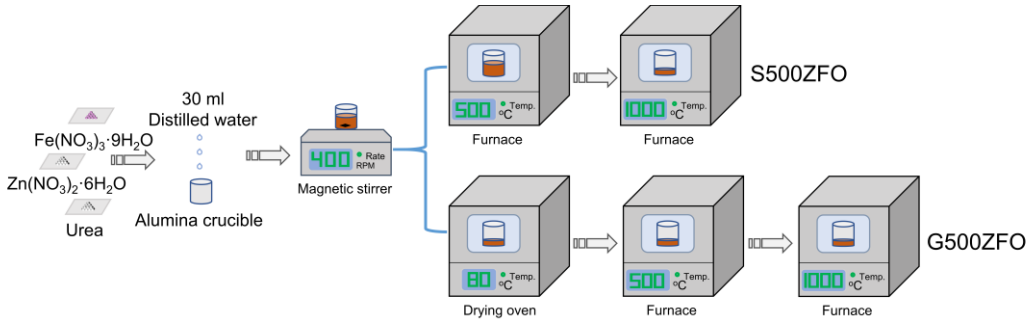

Figure 2.1 Schematic illustration of the $ZnFe_2O_4$ powders preparation procedure.

To further understand the SCS process of ZFO using different precursors. A lab-made temperature monitoring apparatus were made, as shown in Figure 2.2. The equipment is consisted of a heater, a stainless-steel bin with a long vertical stainless-steel mesh chimney and a thermocouple coupled with monitor.

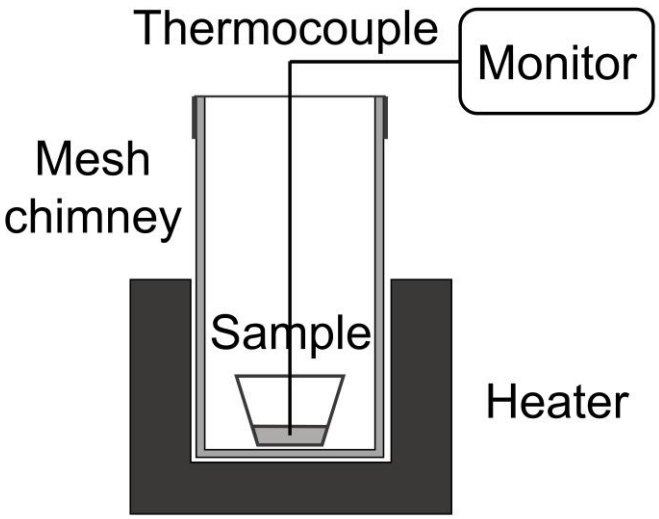

Figure 2.2 Temperature test equipment

Photocatalysts used in this study were fabricated by a SCS method using urea as fuel

according to the following reactions.

$$3Zn(NO_3)_2 + 6Fe(NO_3)_3 + 20CO(NH_2)_2 = 3ZnFe_2O_4 + 40H_2O + 32N_2 + 20CO_2 \quad (2.1)$$

$$SnCl_4 + 3NH_4NO_3 + CO(NH_2)_2 = SnO_2 + 4HCl + CO_2 + 6H_2O + 4N_2 \quad (2.2)$$

For synthesis of single ZFO or SnO_2, stoichiometric number of reagents according to Equations (2.1) and (2.2) were dissolved with deionized water and stirred for 30 min. Then put the transparent solution into a drying oven for 12 h at 80 ^oC. Then the mixture was underwent a two-step high temperature calcination process at 500 and 1000 ^oC for 10 and 120 min, respectively.

ZFO/SnO_2 composites with different SnO_2 mole ratios (5%, 10%, and 15%) were fabricated by performing the same process as single catalyst and were designed as ZFO-SnO_2 (5%), ZFO-SnO_2 (10%), and ZFO-SnO_2 (15%), respectively.

2.2.3. Characterization

X-ray diffraction (XRD) patterns were collected at a diffractometer (Miniflex 600, Rigaku) using the radiation source of Cu Kα. The size values of crystallite were calculated by the Debye-Scherrer equation [29]. A field emission scanning electron microscope (JEOL, JSM-7001FA) was performed to study the surface morphologies of samples. X-ray photoelectron spectroscopic (XPS) measurements were performed at an X-ray photoelectron spectrometer (JEOL, JPS-9200), which was operated at 10 kV and 10 mA using Mg Kα source. All the binding energies data in XPS spectra were calibrated with C 1s as the reference (284.8 eV). UV-Vis absorption spectra were collected on a UV-Vis spectrophotometer (JASCO 770) equipped with an integrating sphere attachment.

2.2.4. Photocatalytic and photo-Fenton activity measurements

The MB aqueous solution degradation experiments were performed to evaluate the photocatalytic degradation performance of as-obtained catalysts. Typically, the powder

photocatalysts of 50 mg were dispersed in a beaker containing 50 mL MB aqueous solution (20 ppm). To obtain adsorption equilibrium, the mixture solution in a shade cloth was magnetically stirred for 30 min. A Xe lamp as simulated solar light was applied to irradiate right above from the aqueous. During degradation process, 3 mL of the solution was drawn every 15 min. After centrifugation, the residual solution was analyzed by a UV-Vis spectrophotometer (JASCO, V-630). For photo-Fenton reaction, 100 μL H_2O_2 (34 wt%) was added into the solution after stirring in the dark. The degradation efficiency can be obtained from the following Equation (2.3)

$$\frac{C_0\text{-}C}{C_0}\times 100\% \tag{2.3}$$

where C_0 and C are the concentration of MB after stirring in the dark and under irradiation, respectively.

2.3. Results and discussion

2.3.1. The effect of SCS precursor on product composition

XRD patterns of S500ZFO and G500ZFO are shown in Figure 2.3. For solution precursor SCS synthesis, the final products include $ZnFe_2O_4$ and impure phase ZnO. For gel precursor SCS synthesis, the final product only includes pure $ZnFe_2O_4$ phase with high crystallinity without any impurities. Therefore, SCS synthesis with gel precursor is beneficial to pure phase samples production.

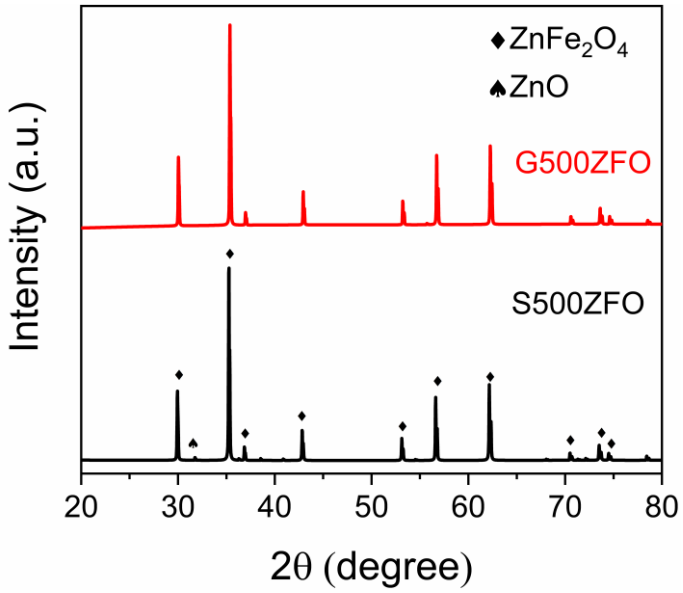

Figure 2.3 XRD patterns of solution and gel precursor samples

The possible reasons for this result were checked by testing temperature-time curves, as shown in Figure 2.4. For SCS synthesis process using solution precursor, there are two processes including water evaporation and combustion process. However, there is only combustion synthesis for gel precursor SCS synthesis process. Specifically, the highest temperature points for S500ZFO and G500ZFO are 350 and 460 ^{o}C, respectively. The high combustion temperature for G500ZFO is beneficial to the formation of pure phase product.

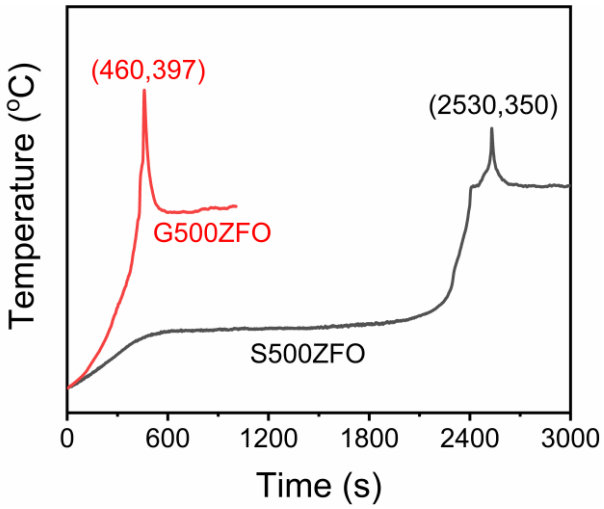

Figure 2.4 Temperature vs. time curves of solution-precursor and gel-precursor samples during SCS ignition process.

2.3.2. Crystalline structure and component composition

XRD patterns demonstrated in Figure 2.5 confirmed the composition of obtained catalysts. The diffraction peaks of ZFO can be ascribed to the crystal planes of cubic spinel $ZnFe_2O_4$ (PDF#01-082-1049) [30]. These sharp and strong peaks indicate high crystallinity of samples due to the high calcination temperature during the SCS process. The sharp diffraction peaks of pure SnO_2 also indicate its high crystallinity and tetragonal SnO_2 phase (JCPDS NO. 01-071-5324) [31]. There is the coexistence of diffraction peaks from ZFO and SnO_2 in the composites, indicating the successful formation of ZFO/SnO_2 composite. With increasing the amount of SnO_2, the diffraction peaks intensity of SnO_2 increased, while that of ZFO decreased. A new peak appeared at 33.26^o in the ZFO/SnO_2 composites. This peak can be ascribed to the (104) plane of Fe_2O_3 (JCPDS NO. 01-087-1166) [32], which is similar to the literature [17]. Meanwhile, the stability of catalysts can be affected by the crystallite size. Sample with smaller crystallite size often provides a more stable crystallite phase [33]. Based on the Debye-Scherrer equation [29], the average crystallite sizes of ZFO are estimated to be 116, 98, 89, and 93 nm in the ZFO, ZFO-SnO_2 (5%), ZFO-SnO_2 (10%), and ZFO-SnO_2 (15%) samples, respectively. Likewise, the average crystallite size of pure SnO_2 is estimated to be 42 nm. In the composites, the addition of SnO_2 resulted in the crystallite size of ZFO decreased and showed the smallest size when the addition amount of SnO_2 is 10% in the ZFO-SnO_2 (10%) sample.

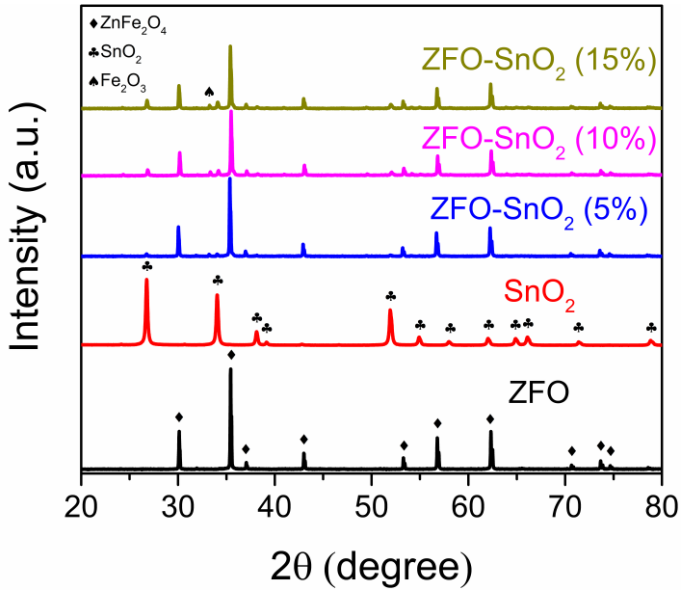

Figure 2.5 XRD patterns of ZFO, SnO_2, and ZFO-SnO_2 composites.

2.3.3. Surface morphology

The morphology and elemental distribution of samples were examined by the FE-SEM and EDS shown in Figure 2.6. The morphology image in Figure 2.6 shows that ZFO with smooth surface is aggregated of some nanoparticles due to the high calcination temperature. Compared to pure ZFO, ZFO/SnO_2 composites show decreased particle size shown in Figure 2.6b-d, which is possibly due to the incorporation of $SnCl_4$ as new nucleation sites during the SCS process. The particle size of the composite is decreased with an increase in the amount of SnO_2, resulting in the smallest particle size in ZFO-SnO_2 (10%). An excess amount of SnO_2 may lead to a greater particle size shown in Figure 2.6d. As shown in Figure 2.6e, SnO_2 has a smaller particle size around 40 nm compared to ZFO. The above SEM results agree with the XRD results. To clearly identify the formation configuration of the ZFO/SnO_2 composite, EDS measurements were performed to characterize the individual elemental mappings of ZFO-SnO_2 (10%) sample. As shown in Figure 2.6g-j, all the elements are uniformly distributed, indicating the homogeneous distribution of ZFO and SnO_2 in ZFO/SnO_2 composites.

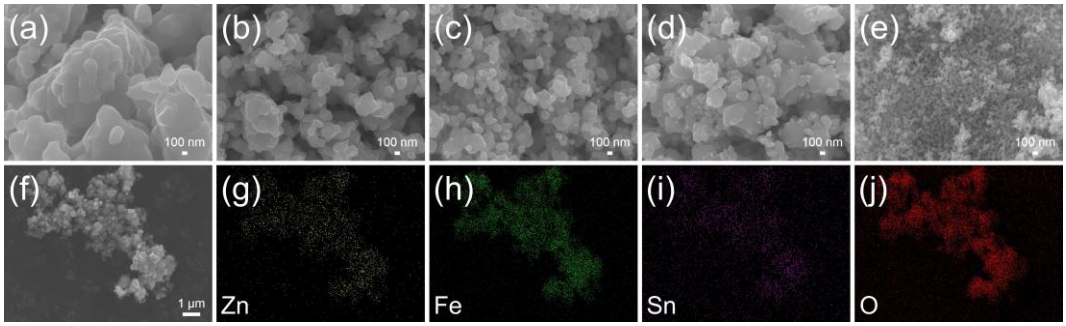

Figure 2.6 SEM images of (a) ZFO, (b) ZFO-SnO_2 (5%), (c) ZFO-SnO_2 (10%), (d) ZFO-SnO_2 (15%), and (e) SnO_2. EDS elemental mapping images of (f) ZFO-SnO_2 (10%) at (g) Zn, (h) Fe, (i) Sn, and (j) O.

2.3.4. Surface state analysis

The surface chemical composition and state of the obtained species were studied by XPS. Their detailed XPS spectra of Zn, Sn, and Fe elements in the ZFO-SnO_2 (10%) and O element of all samples are shown in Figure 2.7. As shown in Figure 2.7a, two peaks of binding energies at 1021.4 and 1044.4 eV of Zn 2p spectrum are corresponding to Zn $2p_{3/2}$ and Zn $2p_{1/2}$, respectively [34]. Figure 2.7b exhibits two expected peaks of Sn $2d_{5/2}$ and Sn $2d_{3/2}$ in the ZFO-SnO_2 (10%) sample and the corresponding binding energies are 486.2 and 494.8 eV, respectively, which is demonstrated as Sn(IV) state [35]. For Fe 2p spectrum in Figure 2.7c, two peaks with binding energies at around 711.0 and 724.7 eV can be ascribed to Fe $2p_{3/2}$ and Fe $2p_{1/2}$, respectively. There are two shakeup accompanying satellite signals (at around 717.5 and 724.1 eV), confirming the Fe(III) chemical state within the catalyst, which are consistent with the previous report [36]. The spectrum of Fe $2p_{3/2}$ can be deconvoluted into two peaks, the peaks with lower and higher binding energies are corresponding to octahedral and tetrahedral sites, respectively [37]. The chemical state of O element is significant important for the photocatalytic properties of catalyst. Broad peaks of O 1s spectra for all samples can be observed in Figure 2.7d. O 1s spectrum can be deconvoluted into two distinct peaks at approximately 529.9 and 531.3 eV corresponding to the metal-oxygen bonds from lattice (O_L) and oxygen vacancy/defect (O_V), respectively,

with different states for oxygen atoms [38]. On one hand, O_V in metal oxide semiconductors is usually incorporated into the photocatalysts to improve photocatalytic properties due to the adventitious energy levels and improved charge concentration [39-41]. On the other hand, unsuitable O_V incorporation may bring about defects state on the surface. These defects states will provide sites for the recombination of charge carriers, which is disadvantage for the efficient charge separation [42-44]. The ratios of O_L and O_V are calculated according to their area ratios in O 1s spectra. The number of O_V ratios in ZFO and SnO_2 may lead to a high charge recombination under irradiation, resulting in poor photocatalytic properties. The incorporation of SnO_2 results in a slight decrease of O_V ratio, which contributes to the improved photocatalytic properties discussed below.

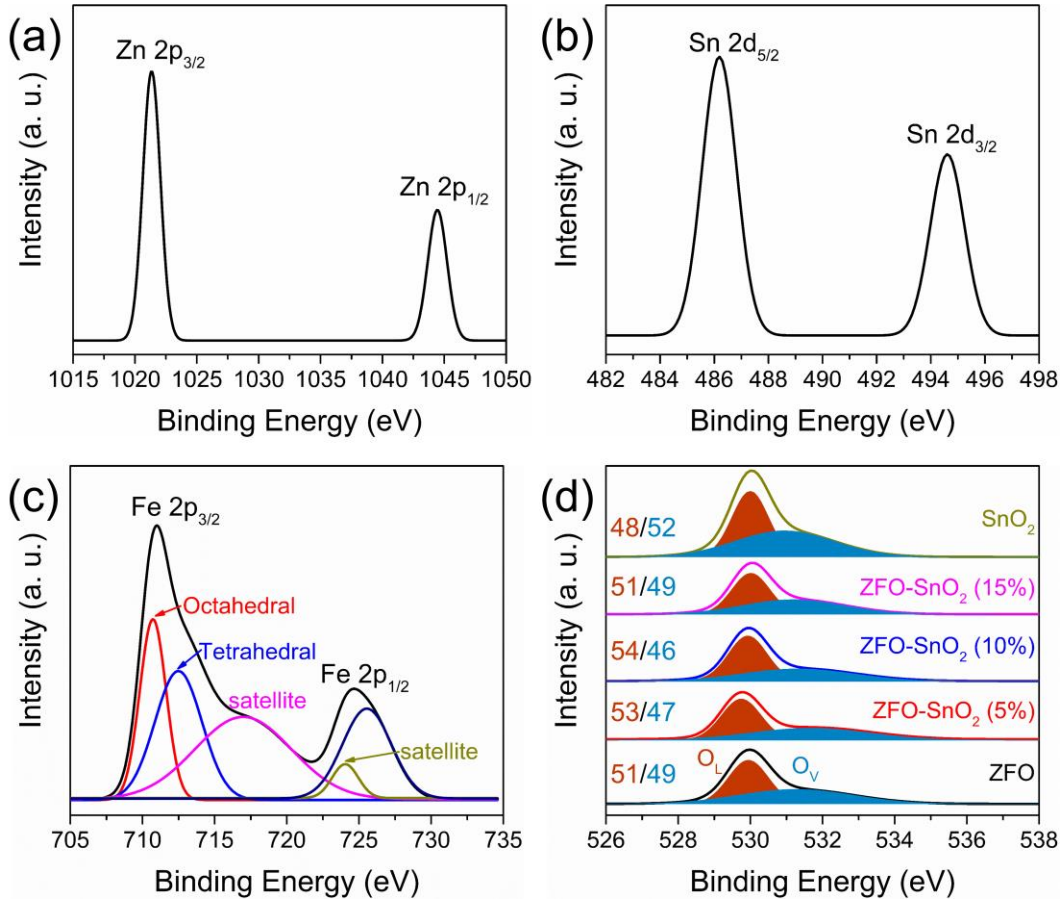

Figure 2.7 High-resolution XPS spectra of typical elements (a) Zn 2p, (b) Sn 3d, and (c) Fe 2p in the ZFO-SnO_2 (10%). (d) The fine structures of the XPS O 1s spectra for all samples. The area ratios of lattice-related (O_L, orange) and vacancy-related (O_V, blue) peaks are marked.

2.3.5. Optical properties

The optical absorption properties of the fabricated catalysts were characterized through UV-Vis absorption spectra shown in Figure 2.8. The absorption onsets for ZFO and SnO_2 are approximately 650 and 500 nm, respectively. Compared to pure ZFO, ZFO/SnO_2 composites show a decrease in the long-wavelength range and ZFO-SnO_2 (10%) sample shows the lowest absorbance position. This may be because of the decreased charge trapping effect on the sample surface due to the shallow energy level impurities [45].

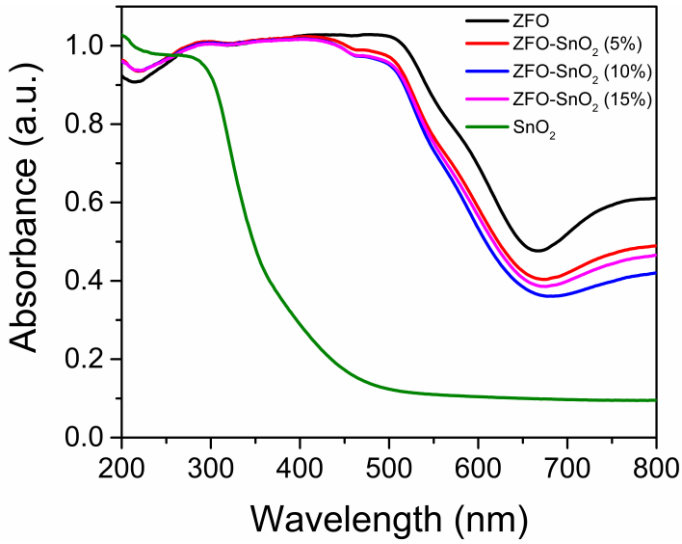

Figure 2.8 UV-Vis absorption spectra of ZFO, SnO_2 and ZFO-SnO_2 composites.

The energy band alignments over ZFO/SnO_2 composite were investigated before studying the photocatalytic properties of samples. Both direct (E_g^d) and indirect (E_g^i) bandgap energy values of ZFO, SnO_2, and ZFO/SnO_2 composites were calculated with the help of Tauc plots through Equation (2.4) [46]:

$$(\alpha h\nu)^{1/n} = A(h\nu - E_g) \quad (2.4)$$

where α is the absorption coefficient, h is the Planck constant, ν is the photon's frequency,

A is a constant, E_g is the optical bandgap energy of catalyst, and the n values are 1/2 and 2 for the direct and indirect transition bandgaps, respectively. As shown in Figure 2.9a, the E_g^d values for ZFO and SnO_2 are 1.99 and 2.62 eV, respectively. ZFO and SnO_2 show relatively small E_g^i values (1.22 and 1.86 eV) shown in Figure 2.9b. For the ZFO/SnO_2 composites, the E_g^d and E_g^i values in Figure 2.9c and d both show slightly increase, demonstrating 2.05 and 1.24 eV, respectively.

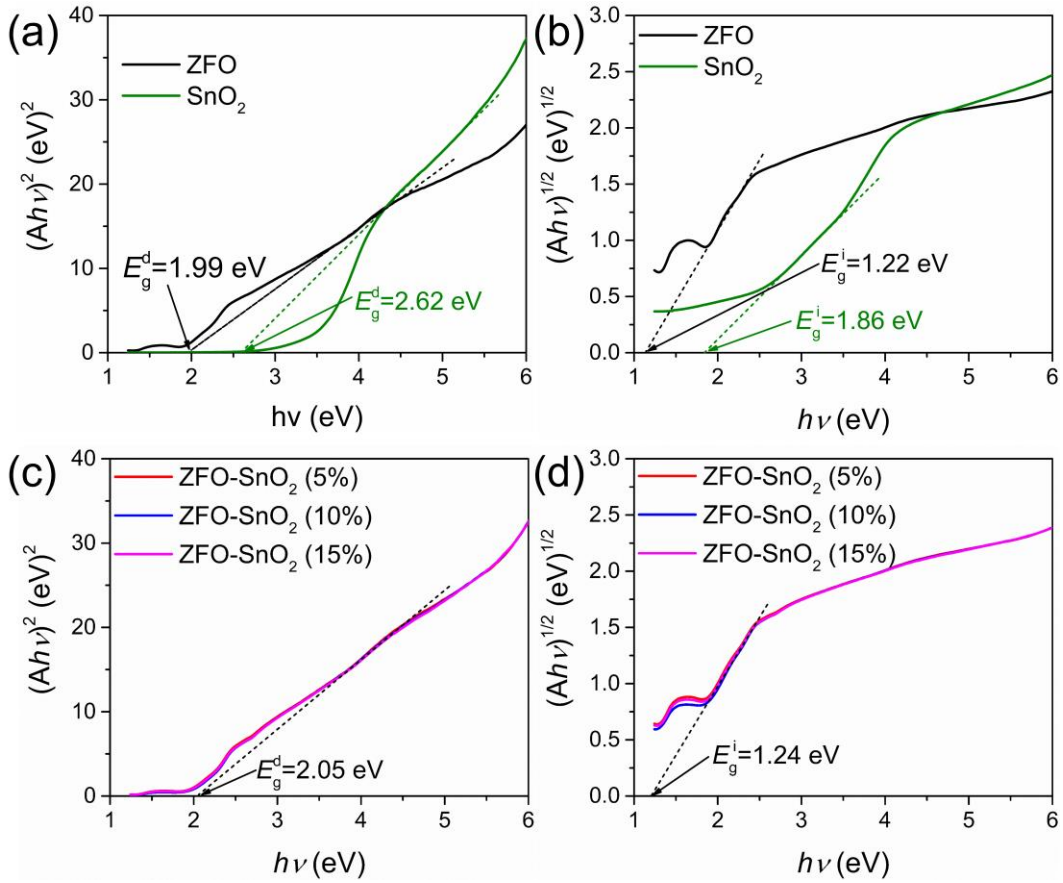

Figure 2.9 (a) Direct bandgap values estimation for ZFO and SnO_2, (b) Indirect bandgap values estimation for ZFO and SnO_2. (b) Direct bandgap values and (c) indirect bandgap values estimation for ZFO/SnO_2 composites.

2.3.6. Band alignment analysis

For the analysis of the band alignment over ZFO/SnO_2 composite, high-resolution XPS spectra at 0 eV surrounding were carried out and the valence band maximum (VBM) values

for single ZFO and SnO_2 samples were calculated via band XPS using a liner extrapolation method. From Figure 2.10, it can be seen that the VBM values of ZFO and SnO_2 were 0.90 and 2.60 eV, respectively. Figure 2.11a and b exhibited the core-level XPS spectra of Zn 2p and Sn 2d. After forming composite, the binding energies of Zn $2p_{3/2}$ and Sn $2d_{5/2}$ were shifted from 1021.4 to 1021.3 eV and from 486.1 to 486.2 eV, respectively. According to the bandgap values, VBM values, and core-level positions summarized in Table 2.1, the valence band offset (ΔE_V) between ZFO and SnO_2 was calculated by the following equations [47]:

$$\Delta E_V(ZFO/SnO_2) = (E_{Zn2p_{3/2}}-E_{VBM})_{ZFO} - \left(E_{Sn2d_{5/2}}-E_{VBM}\right)_{SnO_2} - \Delta E_{CL} \quad (2.5)$$

$$\Delta E_{CL} = (E_{Zn2p_{3/2}}-E_{Sn2d_{5/2}})_{ZFO/SnO_2} \quad (2.6)$$

where, $(E_{Zn2p_{3/2}}-E_{VBM})_{ZFO}$ is the energy difference between Zn $2p_{3/2}$ and VBM in the pure ZFO, $\left(E_{Sn2d_{5/2}}-E_{VBM}\right)_{SnO_2}$ is the energy difference between Sn $2d_{5/2}$ and VBN in the SnO_2, and ΔE_{CL} is the energy difference between two core levels in the ZFO/SnO_2 composite. In addition, the E_g^d values of ZFO and SnO_2 are selected for calculation. Similarly, the conduction band offset (ΔE_C) can be calculated by Equation (2.7). Hence, the measured ΔE_V and ΔE_C are found to be 1.90 and 1.27 eV, respectively.

$$\Delta E_C(ZFO/SnO_2) = E_g^d(ZFO) + \Delta E_V(ZFO/SnO_2) - E_g^d(SnO_2) \quad (2.7)$$

Table 2.1 Bandgap values, VBM and core level binding energy of ZFO, SnO_2 and ZFO/SnO_2 composite samples.

Samples	ZFO	SnO_2	ZFO/SnO_2
Direct band gap, Eg (eV)	1.99	2.62	2.05
Indirect band gap, Eg (eV)	1.22	1.86	1.24
VBM (eV)	0.90	2.60	—
Zn $2p_{3/2}$ (eV)	1021.4	---	1021.3
Sn $2d_{5/2}$ (eV)	---	486.1	486.2

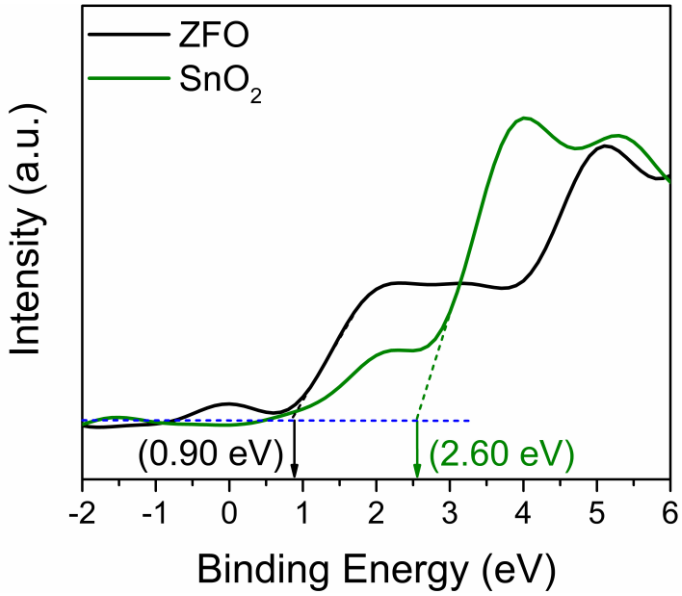

Figure 2.10 Valence band XPS spectra for ZFO and SnO_2

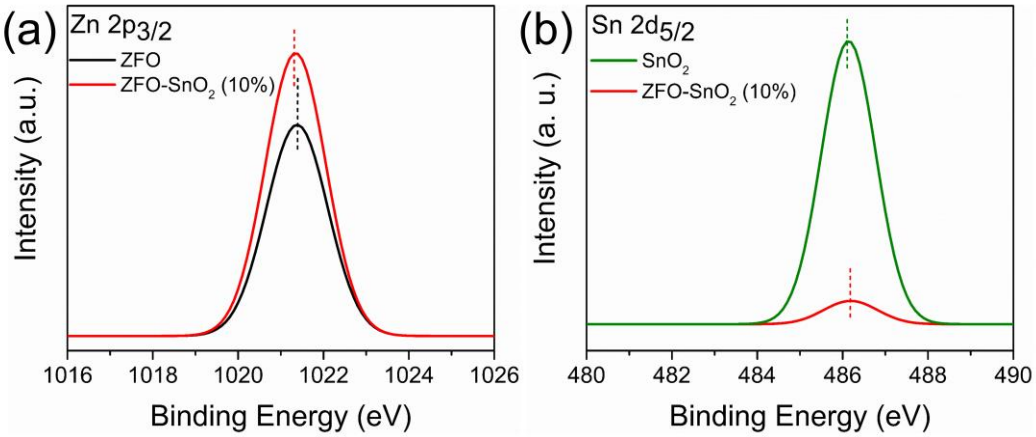

Figure 2.11 (a) Zn $2p_{3/2}$ core level peaks for ZFO and ZFO-SnO_2 (10%), (b) Sn $2d_{5/2}$ core level peaks for SnO_2 and ZFO-SnO_2 (10%).

2.3.7. Photocatalytic MB degradation

MB degradation experiments were performed to investigate the photocatalytic performance of as-fabricated catalysts. Figure 2.12 shows the MB degradation and the corresponding kinetics under different experimental conditions within 60 min. First, photocatalytic degradation and rate constants of ZFO, SnO_2, and ZFO/SnO_2 composites were carefully investigated to determine the optimization amount of SnO_2 in ZFO/SnO_2

composites. As shown in Figure 2.12a, single ZFO and SnO_2 catalyst can reach only 32.3% and 37.0% removal of MB under irradiation for 60 min, respectively. Compared to the single catalyst, composite catalysts show superior photocatalytic degradation performance. Specially, ZFO-SnO_2 (10%) shows the highest photocatalytic degradation efficiency (68.7%) in the composites. Herein, the process of MB degradation was analyzed by a pseudo-first-order kinetic reaction model, which can be described as the equation, $-\ln C_0/C = kt$ [48]. The kinetic curves are presented in Figure 2.12b and the corresponding rate constants k are shown in Figure 2.12e. The rate constant values of single ZFO and SnO_2 are 0.00640 and 0.00747 min^{-1}, respectively. Composites often showed enhanced reaction rate constant compared to single catalyst. Moreover, ZFO-SnO_2 (10%) catalyst shows the highest photocatalytic degradation rate constant of 0.01970 min^{-1} in the composites, about 3.08 and 2.64 times higher than that of single ZFO and SnO_2, respectively. According to Figure 2.12a and b, ZFO-SnO_2 (10%) is selected as a sample of the composite to further investigate its degradation property under H_2O_2 condition.

The photocatalytic and photo-Fenton MB degradation of ZFO and ZFO-SnO_2 (10%) samples were performed. As shown in Figure 2.12c, the MB degradation efficiency was only 10.1% under irradiation without any catalysts and H_2O_2, indicating that MB solution had a good photo-stability under irradiation. The addition of photocatalyst could slightly enhance the degradation efficiencies of MB due to its inferior properties of samples as mentioned above. Only 33.3% of MB was removed under irradiation by adding H_2O_2 due to the limited oxidation power of H_2O_2 [49]. When there was only catalyst and H_2O_2, its degradation efficiencies were 33.8% and 40.9% for ZFO/H_2O_2 (Dark) and ZFO-SnO_2 (10%)/H_2O_2 (Dark) conditions, respectively. This is because of the limited dark Fenton reaction of catalysts under experimental conditions [50]. Interestingly, the light-catalysts-

H_2O_2 systems usually show enhanced degradation efficiencies compared to the light-catalysts, catalysts-H_2O_2, and light-H_2O_2 systems. Typically, the ZFO/H_2O_2 and ZFO-SnO_2 (10%)/H_2O_2 shown improved MB degradation efficiencies of 65.8% and 95.2% within 60 min, respectively. To further study the improvement of MB degradation efficiencies for ZFO-SnO_2 (10%), the plots of ln(C_0/C) versus reaction time are shown in Figure 2.12d, and the corresponding rate constant k collected in Figure 2.12e were calculated according to the slope of the curves. Usually, the rate constants of light-catalysts-H_2O_2 systems are faster than that of light-catalysts and catalysts-H_2O_2 systems. Specially, the light ZFO/H_2O_2 condition shows MB degradation rate constant of 0.01783 min^{-1}, which is approximately 2.61 and 2.79 times higher than that of ZFO/H_2O_2 (Dark) and light ZFO conditions, respectively. While, the light ZFO-SnO_2 (10%)/H_2O_2 condition shows the rapidest MB degradation rate constant of 0.05301 min^{-1}, which is approximately 6.44 and 2.69 times higher than that of ZFO-SnO_2 (10%)/H_2O_2 (Dark) and light ZFO conditions, respectively.

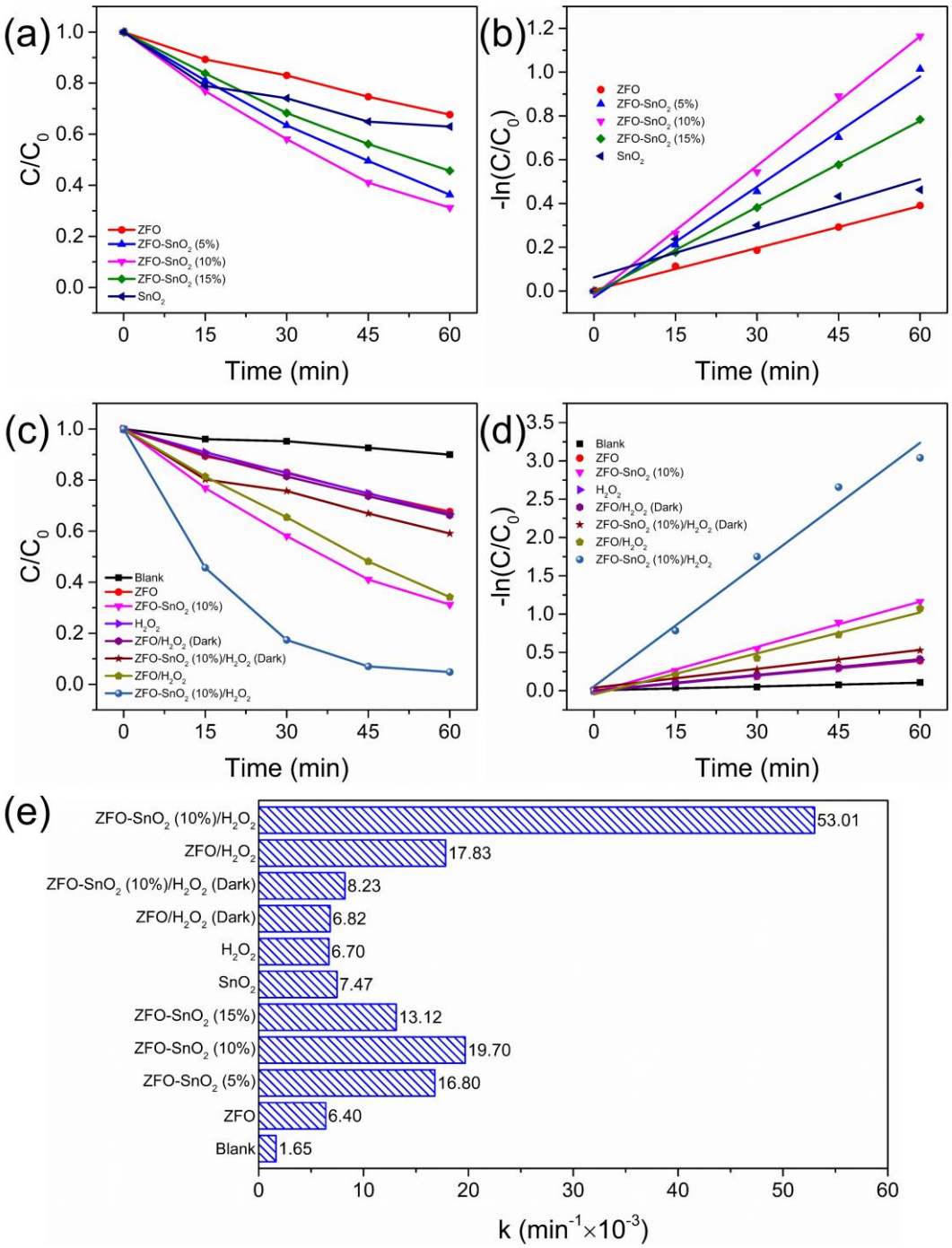

Figure 2.12 (a) Photocatalytic degradation and (b) the corresponding degradation kinetics of MB in optimization of SnO_2 number of ZFO/SnO_2 composites. (c) Degradation and (d) the corresponding degradation kinetics of MB in blank, catalysts, H_2O_2, catalysts/H_2O_2 (Dark), and catalysts/H_2O_2 conditions. (e) Rate constant *k* of MB degradation.

The band alignment of ZFO/SnO_2 composite and the corresponding schematic for the MB degradation process are shown in Figure 2.13. When the single photocatalyst (ZFO or SnO_2) was irradiated in the solution of MB, electron-hole pairs were generated in the bulk of semiconductor (Equations (2.8) and (2.9)). After separation and diffusion, few parts of photogenerated hole (h^+) will transfer to the surface and react with H_2O or the surface-adsorbed OH group to form ·OH (Equations (2.10) and (2.11)). However, only a few parts of photogenerated holes (h^+) and electrons (e^-) can be efficiently utilized due to the rapid recombination of charges in ZFO sample [51] and relatively large bandgap of SnO_2 semiconductor as mentioned above. Therefore, the photocatalytic degradation efficiencies of ZFO and SnO_2 were relatively low. According to the band alignment of ZFO/SnO_2 composite in Figure 2.13, the electrons in the conduction band (CB) and holes in the valence band (VB) will transfer in the opposite direction. This efficient configuration of band alignment will lead to a superior charge separation efficiency in ZFO/SnO_2 composites, resulting in more charges are utilized in the MB degradation process compared to single catalyst conditions [52]. Therefore, ZFO/SnO_2 composites show relatively superior photocatalytic degradation efficiencies than single catalyst. The addition of H_2O_2 is beneficial for MB degradation. The activity of H_2O_2 can be activated by Fe(II) through Equation (2.12) called dark Fenton reaction. However, the dark Fenton degradation efficiency was relatively low due to the limited cycle from Fe(III) to Fe(II). Meanwhile, Fe(III) on the surface of the photocatalyst can capture few parts of photogenerated e^- to form Fe(II) (Equation (2.13)). Under condition of H_2O_2, photogenerated e^- can be captured by H_2O_2 through Equation (2.14). On one hand, the H_2O_2 can produce more ·OH and OH^-. One the other hand, the consumption of e^- will also promote the separation efficiency of charge carrier pairs. Importantly, more and more Fe(II) and ·OH will be produced under

irradiation through the reaction of Fe(III) and OH^- (Equation (2.15)). The increase of Fe(II) will also promote the reaction of Equation (2.12) to produce more ·OH. Finally, the increase of ·OH will promote MB degradation (Equation (2.16)). According to the abovementioned analysis, ZFO-SnO_2 (10%) photo-catalysts shows the highest MB degradation efficiency with the addition of H_2O_2 under irradiation.

$$ZFO + h\nu \rightarrow h^+(ZFO) + e^-(ZFO) \quad (2.8)$$

$$SnO_2 + h\nu \rightarrow h^+(SnO_2) + e^-(SnO_2) \quad (2.9)$$

$$h^+ + H_2O \rightarrow H^+ + \cdot OH \quad (2.10)$$

$$h^+ + OH^- \rightarrow \cdot OH \quad (2.11)$$

$$Fe(III) + e^- \rightarrow Fe(II) \quad (2.12)$$

$$Fe(II) + H_2O_2 \rightarrow Fe(III) + OH^- + \cdot OH \quad (2.13)$$

$$H_2O_2 + e^- \rightarrow OH^- + \cdot OH \quad (2.14)$$

$$Fe(III) + OH\text{-} + h\nu \rightarrow Fe(II) + \cdot OH \quad (2.15)$$

$$\cdot OH + MB \rightarrow \text{decomposed products} \quad (2.16)$$

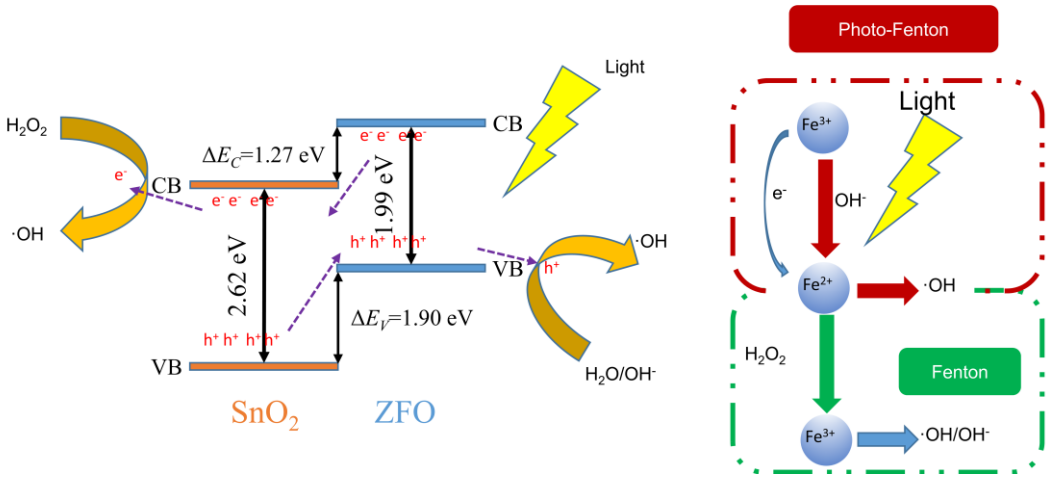

Figure 2.13 Schematic illustration for charge separation and transfer over ZFO/SnO_2 composite and MB degradation mechanism under light irradiation.

2.4. Conclusions

In summary, we have successfully fabricated the ZFO/SnO_2 composites through a facile solution combustion synthesis method for MB aqueous solution degradation. The characterizations of crystallite structure and morphology revealed that ZFO/SnO_2 composites showed relatively small crystallite and particle size, resulting in higher active surface area. The introduction of SnO_2 significantly improved the photocatalytic MB degradation efficiency of pure ZFO catalyst. Specifically, ZFO-SnO_2 (10%) catalyst exhibited the highest photocatalytic degradation rate constant of 0.01970 min^{-1} in the composites, approximately 3.08 and 2.64 times higher than that of single ZFO (0.00640 min^{-1}) and SnO_2 (0.00747 min^{-1}), respectively. The improvement of photocatalytic degradation performance was due to enhanced charge separation efficiency in the ZFO/SnO_2 composite based on the band alignment analysis. ZFO-SnO_2 (10%) with H_2O_2 showed the highest photo-Fenton degradation rate constant of 0.05301 min^{-1} and could remove 95.2% of MB within 60 min under irradiation. This work also provides an available strategy for constructing a ZFO based composite for high efficiency photocatalytic dye degradation.

References

1. C. Leal Marchena, L. Lerici, S. Renzini, et al. Synthesis and characterization of a novel tungstosilicic acid immobilized on zeolites catalyst for the photodegradation of methyl orange. *Applied Catalysis B: Environmental*. **2016** 23-30.
2. S. A. Hassanzadeh-Tabrizi, M. M. Motlagh, and S. Salahshour. Synthesis of ZnO/CuO nanocomposite immobilized on γ-Al_2O_3 and application for removal of methyl orange. *Applied Surface Science*. **2016** 237-243.
3. P. Wang, X. Wang, S. Yu, et al. Silica coated Fe_3O_4 magnetic nanospheres for high removal of organic pollutants from wastewater. *Chemical Engineering Journal*. **2016** 280-288.
4. I. Oller, S. Malato, and J. A. Sánchez-Pérez. Combination of advanced oxidation processes and biological treatments for wastewater decontamination-A review. *Science of the Total Environment*. **2011** (20) 4141-4166.
5. A.-K. Ghattas, F. Fischer, A. Wick, et al. Anaerobic biodegradation of (emerging) organic contaminants in the aquatic environment. *Water Research*. **2017** 268-295.
6. J. Xing, J. Du, X. Zhang, et al. A Ni-P@NiCo LDH core-shell nanorod-decorated nickel foam with enhanced areal specific capacitance for high-performance supercapacitors. *Dalton Transactions*. **2017** (30) 10064-10072.
7. M. Hartmann, S. Kullmann, and H. Keller. Wastewater treatment with heterogeneous Fenton-type catalysts based on porous materials. *Journal of Materials Chemistry*. **2010** (41) 9002-9017.
8. L. Zhang, X. Yuan, H. Wang, et al. Facile preparation of an Ag/$AgVO_3$/BiOCl composite and its enhanced photocatalytic behavior for methylene blue degradation. *RSC Advances*. **2015** (119) 98184-98193.

9. T. R. Sobahi and M. S. Amin. Synthesis of ZnO/$ZnFe_2O_4$/ Pt nanoparticles heterojunction photocatalysts with superior photocatalytic activity. *Ceramics International*. **2020** (3) 3558-3564.
10. H. Lin, H. Zhang, and L. Hou. Degradation of C. I. acid orange 7 in aqueous solution by a novel electro/Fe_3O_4/PDS process. *Journal of Hazardous Materials*. **2014** 182-191.
11. J. De Laat and H. Gallard. Catalytic decomposition of hydrogen peroxide by Fe(III) in homogeneous aqueous solution: Mechanism and kinetic modeling. *Environmental Science & Technology*. **1999** (16) 2726-2732.
12. R. Zhang, Q. Han, Y. Li, et al. Solvothermal synthesis of a peony flower-like dual Z-scheme PANI/BiOBr/$ZnFe_2O_4$ photocatalyst with excellent photocatalytic redox activity for organic pollutant under visible-light. *Separation and Purification Technology*. **2020** 116098.
13. C. Cai, Z. Zhang, J. Liu, et al. Visible light-assisted heterogeneous Fenton with $ZnFe_2O_4$ for the degradation of orange II in water. *Applied Catalysis B: Environmental*. **2016** 456-468.
14. S. Chandrasekaran, C. Bowen, P. Zhang, et al. Spinel photocatalysts for environmental remediation, hydrogen generation, CO_2 reduction and photoelectrochemical water splitting. *Journal of Materials Chemistry A*. **2018** (24) 11078-11104.
15. R.-G. Ciocarlan, E. M. Seftel, R. Gavrila, et al. Spinel nanoparticles on stick-like Freudenbergite nanocomposites as effective smart-removal photocatalysts for the degradation of organic pollutants under visible light. *Journal of Alloys and Compounds*. **2020** 153403.

16. C. G. Anchieta, E. C. Severo, C. Rigo, et al. Rapid and facile preparation of zinc ferrite ($ZnFe_2O_4$) oxide by microwave-solvothermal technique and its catalytic activity in heterogeneous photo-Fenton reaction. *Materials Chemistry and Physics*. **2015** 141-147.
17. W. Zhao, C. Liang, B. Wang, et al. Enhanced photocatalytic and Fenton-like performance of CuO_x-decorated $ZnFe_2O_4$. *ACS Applied Materials & Interfaces*. **2017** (48) 41927-41936.
18. Y. Li, Y. Li, Y. Yin, et al. Facile synthesis of highly efficient $ZnO/ZnFe_2O_4$ photocatalyst using earth-abundant sphalerite and its visible light photocatalytic activity. *Applied Catalysis B: Environmental*. **2018** 324-336.
19. Y. Ma, Q. Wang, and S. Xing. Insight into the catalytic mechanism of γ-$Fe_2O_3/ZnFe_2O_4$ for hydrogen peroxide activation under visible light. *Journal of Colloid and Interface Science*. **2018** 247-254.
20. X. Zhu, F. Zhang, M. Wang, et al. Facile synthesis, structure and visible light photocatalytic activity of recyclable $ZnFe_2O_4/TiO_2$. *Applied Surface Science*. **2014** 83-89.
21. Y. Yao, F. Lu, J. Qin, et al. Magnetic $ZnFe_2O_4$-C_3N_4 hybrid for photocatalytic degradation of aqueous organic pollutants by visible light. *Industrial & Engineering Chemistry Research*. **2014** (44) 17294-17302.
22. S. Li, H. Li, J. Liu, et al. Highly efficient degradation of organic dyes by palladium nanoparticles decorated on 2D magnetic reduced graphene oxide nanosheets. *Dalton Transactions*. **2015** (19) 9193-9199.
23. J. Wang, Q. Zhang, F. Deng, et al. Rapid toxicity elimination of organic pollutants by the photocatalysis of environment-friendly and magnetically recoverable step-scheme $SnFe_2O_4/ZnFe_2O_4$ nano-heterojunctions. *Chemical Engineering Journal*. **2020** 122264.

24. X. Wang, H. Fan, and P. Ren. Electrospinning derived hollow SnO_2 microtubes with highly photocatalytic property. *Catalysis Communications*. **2013** 37-41.
25. E. E. El-Katori, M. A. Ahmed, A. A. El-Bindary, et al. Impact of CdS/SnO_2 heterostructured nanoparticle as visible light active photocatalyst for the removal methylene blue dye. *Journal of Photochemistry and Photobiology A: Chemistry*. **2020** 112403.
26. B. Babu, V. V. N. Harish, R. Koutavarapu, et al. Enhanced visible-light-active photocatalytic performance using CdS nanorods decorated with colloidal SnO_2 quantum dots: Optimization of core-shell nanostructure. *Journal of Industrial and Engineering Chemistry*. **2019** 476-487.
27. M. T. Uddin, Y. Nicolas, C. Olivier, et al. Nanostructured SnO_2-ZnO heterojunction photocatalysts showing enhanced photocatalytic activity for the degradation of organic dyes. *Inorganic Chemistry*. **2012** (14) 7764-7773.
28. S. Zarrin and F. Heshmatpour. Facile preparation of new nanohybrids for enhancing photocatalytic activity toward removal of organic dyes under visible light irradiation. *Journal of Physics and Chemistry of Solids*. **2020** 109271.
29. Z. Zhang, M. F. Hossain, and T. Takahashi. Photoelectrochemical water splitting on highly smooth and ordered TiO_2 nanotube arrays for hydrogen generation. *International Journal of Hydrogen Energy*. **2010** (16) 8528-8535.
30. D. Lu, Y. Zhang, S. Lin, et al. Synthesis of magnetic $ZnFe_2O_4$/graphene composite and its application in photocatalytic degradation of dyes. *Journal of Alloys and Compounds*. **2013** 336-342.
31. H. Park, H. Choi, K. Nam, et al. Anode design based on microscale porous scaffolds for advanced lithium ion batteries. *Journal of Electronic Materials*. **2017** (6) 3789-3795.

32. J.-C. Wang, Y. Li, H. Li, et al. A novel synthesis of oleophylic Fe_2O_3/polystyrene fibers by γ-Ray irradiation for the enhanced photocatalysis of 4-chlorophenol and 4-nitrophenol degradation. *Journal of Hazardous Materials*. **2019** 120806.
33. L. Kőrösi and I. Dékány. Preparation and investigation of structural and photocatalytic properties of phosphate modified titanium dioxide. *Colloids and Surfaces A: Physicochemical and Engineering Aspects*. **2006** (1) 146-154.
34. M. Chen, D. Liu, Y. Deng, et al. Tailoring the porosity of ZnO/$ZnFe_2O_4$ composites for photocatalytic applications. *Ceramics International*. **2017** (17) 16027-16031.
35. A. N. Bondarchuk, I. Corrales-Mendoza, J. A. Aguilar-Martínez, et al. A $BiVO_4$ photoanode grown on porous and conductive SnO_2 ceramics for water splitting driven by solar energy. *Ceramics International*. **2020** (7) 9040-9049.
36. T. Yamashita and P. Hayes. Analysis of XPS spectra of Fe^{2+} and Fe^{3+} ions in oxide materials. *Applied Surface Science*. **2008** (8) 2441-2449.
37. J. Liu, M. Zeng, and R. Yu. Surfactant-free synthesis of octahedral ZnO/$ZnFe_2O_4$ heterostructure with ultrahigh and selective adsorption capacity of malachite green. *Scientific Reports*. **2016** (1) 25074.
38. Y. Huang, Y. Yu, Y. Yu, et al. Oxygen vacancy engineering in photocatalysis. *Solar RRL*. **2020** (8) 2000037.
39. J. H. Kim, Y. J. Jang, S. H. Choi, et al. A multitude of modifications strategy of $ZnFe_2O_4$ nanorod photoanodes for enhanced photoelectrochemical water splitting activity. *Journal of Materials Chemistry A*. **2018** (26) 12693-12700.
40. J. H. Kim, Y. J. Jang, J. H. Kim, et al. Defective $ZnFe_2O_4$ nanorods with oxygen vacancy for photoelectrochemical water splitting. *Nanoscale*. **2015** (45) 19144-19151.

41. N. Zhang, X. Li, H. Ye, et al. Oxide defect engineering enables to couple solar energy into oxygen activation. *Journal of the American Chemical Society*. **2016** (28) 8928-8935.
42. J. Gan, X. Lu, J. Wu, et al. Oxygen vacancies promoting photoelectrochemical performance of In_2O_3 nanocubes. *Scientific Reports*. **2013** (1) 1021.
43. S. Corby, L. Francàs, A. Kafizas, et al. Determining the role of oxygen vacancies in the photoelectrocatalytic performance of WO_3 for water oxidation. *Chemical Science*. **2020** (11) 2907-2914.
44. M. Sachs, J.-S. Park, E. Pastor, et al. Effect of oxygen deficiency on the excited state kinetics of WO_3 and implications for photocatalysis. *Chemical Science*. **2019** (22) 5667-5677.
45. X. Tao, W. Shi, B. Zeng, et al. Photoinduced surface activation of semiconductor photocatalysts under reaction conditions: A commonly overlooked phenomenon in photocatalysis. *ACS Catalysis*. **2020** (10) 5941-5948.
46. P. Makuła, M. Pacia, and W. Macyk. How to correctly determine the band gap energy of modified semiconductor photocatalysts based on UV-Vis spectra. *The Journal of Physical Chemistry Letters*. **2018** (23) 6814-6817.
47. B. Huang, W. Yang, Y. Wen, et al. Co_3O_4-modified TiO_2 nanotube arrays via atomic layer deposition for improved visible-light photoelectrochemical performance. *ACS Applied Materials & Interfaces*. **2015** (1) 422-431.
48. L. Ge and J. Liu. Efficient visible light-induced photocatalytic degradation of methyl orange by QDs sensitized CdS-Bi_2WO_6. *Applied Catalysis B: Environmental*. **2011** (3) 289-297.

49. X. Chen, W. Wang, H. Xiao, et al. Accelerated TiO_2 photocatalytic degradation of acid orange 7 under visible light mediated by peroxymonosulfate. *Chemical Engineering Journal*. **2012** 290-295.
50. M. Su, C. He, V. K. Sharma, et al. Mesoporous zinc ferrite: Synthesis, characterization, and photocatalytic activity with H_2O_2/visible light. *Journal of Hazardous Materials*. **2012** 95-103.
51. Y. Guo, Y. Guo, D. Tang, et al. Sol-gel synthesis of new $ZnFe_2O_4$/Na-bentonite composites for simultaneous oxidation of RhB and reduction of Cr(VI) under visible light irradiation. *Journal of Alloys and Compounds*. **2019** 1101-1109.
52. H. Wang, L. Zhang, Z. Chen, et al. Semiconductor heterojunction photocatalysts: Design, construction, and photocatalytic performances. *Chemical Society Reviews*. **2014** (15) 5234-5244.

Chapter 3 Effect of Fuels and Fuel Ratios on Photocatalytic Performance of $CaFe_2O_4$ by Solution Combustion Synthesis

3.0. Brief summary

$CaFe_2O_4$ (CFO) was fabricated by solution combustion synthesis (SCS) method using different fuels (urea and glucose) and fuel ratios (0.5, 1.0, and 1.5). CFO-Glucose shows a smaller crystallite size than CFO-Urea sample. CFO-1.0 presents the smallest crystallite size among various fuel ratios products. CFO-1.0 photocatalyst presents the best photocatalytic MB degradation with a kinetic constant of 0.00372 min^{-1} compared to CFO-Urea (0.00123 min^{-1}), CFO-0.5 (0.00176 min^{-1}), and CFO-2.0 (0.00249 min^{-1}). Based on the PL and XPS characterizations, the efficient photocatalytic performance of CFO-1.0 is attributed to the efficient charge separation and suitable photocatalyst surface state.

3.1. Introduction

Ternary metal oxide materials, such as perovskite type oxides (ABO_3) [1, 2], spinel type oxide (AB_2O_4) [3, 4], scheelite type oxides (ABO_4) [5] and other complex oxides [6], have attracted significant attentions in recent years. The preparation of ternary metal oxide materials used for solar energy conversion and solar-induced environmental remediation (such as solar photovoltaic, solar-induced photoelectrochemical water splitting and photocatalytic contaminant degradation) becomes increasingly important [7-9]. Among them, spinel ferrites are a promising family of ternary metal oxides that have recently drawn increasing attention for applications of solar energy conversion and solar-induced environmental remediation [10, 11]. $CaFe_2O_4$ (CFO) has received the most extensive research as an emerging photo-induced catalyst due to its appropriate band gap for full spectrum, abundant constituent elements and long-term photo stability under solar irradiation [12-15].

Compared to several conventional synthesis methods such as hydrothermal [16-18], co-precipitation [19-22] and mechanical ball-milling [23], solution combustion synthesis

(SCS) [24-26] indicates significant advantages for preparation of calcium ferrite, owing to its simple equipment and experimental procedure, relatively low calcination temperatures, high purity and high homogeneity degree, etc. Fuel kinds and fuel ratios of SCS have a great effect on the final product. Sheng reported that single phase of $K_{0.5}Na_{0.}5NbO3$ products can be successfully prepared in a one-step SCS by adjusting the glycine-nitrate ratio and also shown that the stoichiometric or slightly fuel-excess condition is good for the single step production [27]. However, there is not enough research on the influence of fuel type and fuel ratio on CFO.

Here, we study the synthesis of CFO by SCS process using different fuels (urea and glucose) and different fuel ratios (0.5, 1.0, 2.0). We amply investigate the effect of fuels and fuel ratios of SCS on the morphology, crystal phase composition, photocatalytic MB degradation activity of as-prepared CFO samples.

3.2. Experimental

3.2.1. Materials

All raw reagents used in this chapter were commercially available and used without further purification. Calcium nitrate tetrahydrate ($Ca(NO_3)_2{\cdot}4H_2O$, 98.0%), iron nitrate enneahydrate ($Fe(NO_3){\cdot}9H_2O$ 99.0%), urea (NH_2CONH_2, 99.0%), and glucose ($C_6H_{12}O_6$, 98.0%) were used as raw materials.

3.2.2. Solution combustion synthesis of $CaFe_2O_4$ by different fuels and fuel ratios

In a typical synthesis procedure, 1.446 g $Ca(NO_3)_2{\cdot}4H_2O$, 4.897 g $Fe(NO_3){\cdot}9H_2O$ and 2.427 g urea or 1.838 g glucose were dissolved in 30 mL of distilled water. After constant stirring with the speed of 400 rpm for 30 min at room temperature, a transparent and uniform solution precursor was formed in the alumina crucible. The solution precursor was directly put in a oven at 100 ^oC for 12 h, then 500 ^oC for 10 min. After cooling down to

room temperature and fully grinding, the samples were performed calcination process at 1000 ^{o}C for 2 h. The final products using urea and glucose as precursor are named as CFO-Urea and CFO-Glucose, respectively. To investigate the effect of fuel ratios, 0.919, 1.838, and 3.677 g glucose were added into the solution and the corresponding final products are named as CFO-0.5, CFO-1.0, and CFO-2.0, respectively. Then do the same procedure as above.

3.2.3. Materials characterization

The phase composition and crystal structure of the as-prepared samples were characterized by X-ray diffraction (XRD) analysis using an X-ray diffractometer (Rigaku Miniflex) with Cu Kα radiation. The morphology and microstructure of the as-prepared samples were inspected by a scanning electron microscopy (SEM, JEOL, JSM-7400F). A measuring device (GRAPHTEC midi LOGGER GL220) coupled with a K-type thermocouple was used to measure and record temperature changes over time during the ignition process. Further detailed morphology and microstructure of the as-fabricated samples were studied through transmission electron microscopy (TEM) using JEM-2000FX (JEOL, Japan) at operating voltage of 200 kV. The surface chemical state analysis was carried out at an X-ray photoelectron spectrometer (JEOL, JPS-9200) operated at 10 kV and 10 mA. A UV-Vis spectrometer (JASCO V-770) equipped with an integrating sphere attachment was performed to test the optical properties of samples. The photoluminescence (PL) spectra were collected through a luminescence spectrometer (JASCO FP-8600).

3.2.4. Photocatalytic performance characterization

The photocatalytic performance of as-fabricated CFO samples was characterized by MB solution degradation experiments. Typically, 50 mL MB solution (20 μL/L) was chosen as

degradation target. Before irradiation, the solution containing as-fabricated photocatalysts of 50 mg was magnetically stirred for 30 min in the dark to achieve adsorption-desorption equilibrium. A simulated solar light (HAL-320W, Asahi spectra) as a light source was used to provide an irradiation intensity of 100 mW/cm^2 from the top of the solution. Approximately 3 mL solution was taken every 30 min and centrifuged to remove the catalyst. The absorption spectra of the residual solution were collected by UV-Vis spectrometer (JASCO V-770). The peak intensity at 664 nm was chosen to indicate the concentration of solution.

3.3. Results and discussion

3.3.1. Crystalline structure and surface morphology

Powder XRD is used to identify the phase composition, crystal structure and crystallinity of the as-prepared materials. Figure 3.1 shows the XRD patterns of CFO photocatalysts synthesized by SCS method with different fuel kinds and fuel ratios. These sharp and strong peaks present great crystallinity of as-fabricated photocatalysts by virtue of a facile SCS method. As shown in Figure 3.1(a), all diffraction peaks of CFO-Urea and CFO-Glucose are perfectly matched to crystal plane of $CaFe_2O_4$ phase (JCPDS NO. 03-065-1333). Diffraction patterns of CFO photocatalysts with different fuel ratios are shown in Figure 3.1(b) and Figure 3.1(c) (enlarged view of corresponding part). When the fuel is insufficient ($\Phi = 0.5$), the final product (CFO-0.5) is only pure $CaFe_2O_4$ phase. However, when the fuel is excess, the impure phases were formed like $Ca_2Fe_2O_5$ (JCPDS NO. 01-071-2264) and Fe_2O_3 (JCPDS NO. 01-087-1166). The simple synthesis process of CFO by SCS method as follows. As the temperature increases, metal nitrates are converted into corresponding metal oxides (CaO and Fe_2O_3) then metal oxides form final products (CFO). When the fuel is excess, part $CaFe_2O_4$ is formed first and then CaO will continue react with $CaFe_2O_4$ to

form $Ca_2Fe_2O_5$. The average crystallite sizes of photocatalysts were calculated from the top three intensity planes of (302), (210), and (410) in $CaFe_2O_4$ based on the Debye-Scherrer equation [28]. CFO-Urea and CFO-Glucose present average crystallite sizes of 97.83 and 73.19 nm, respectively. Samples obtained at different fuel ratios also show different crystallite sizes of 75.41, 73.19, and 97.38 nm for CFO-0.5, CFO-1.0, and CFO-2.0, respectively. The sample of CFO-1.0 (CFO-Glucose) shows the smallest crystallite size.

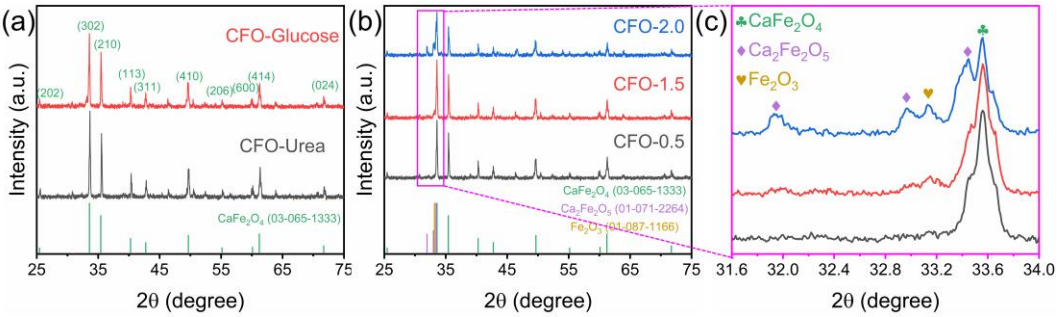

Figure 3.1 XRD of CFO samples prepared by different conditions

The typical surface figures of CFO are shown in Figure 3.2. It can be clearly seen that all samples are gathered together by small particles due to the high calcination temperature. Based on the XRD results, we can know that the average crystal sizes are below 100 nm. However, it is hard to see the clear crystallite sizes differences in SEM results. Therefore, all CFO samples are composed of multiple crystallites.

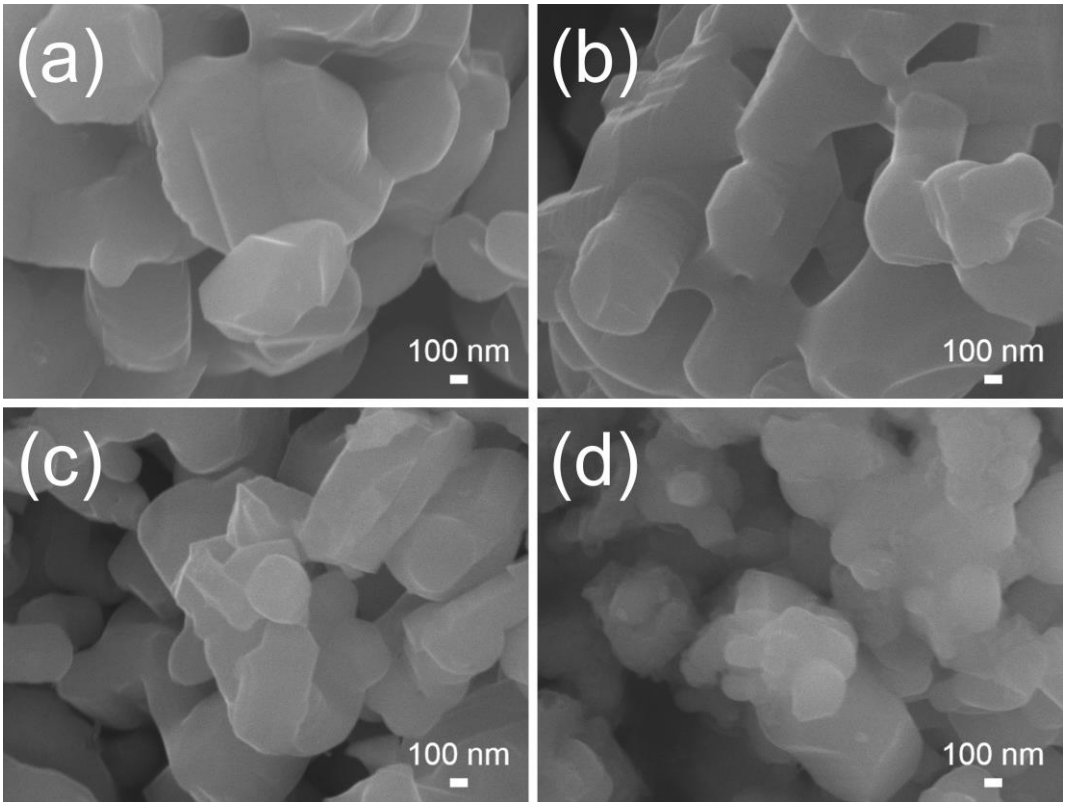

Figure 3.2 SEM figures of (a) CFO-Urea, (b) CFO-Glucose (CFO-1.0), (c) CFO-0.5, and (d) CFO-2.0

EDS was performed to indicate the elemental mappings of CFO-1.0 and CFO-2.0 in Figure 3.3. The molar ratios of Ca, Fe, and O for CFO-1.0 and CFO-2.0 are 17:45:38 and 19:39:42, respectively. Compared to CFO-1.0, CFO-2.0 shows a higher molar ratio of Ca due to the presence of $Ca_2Fe_2O_5$.

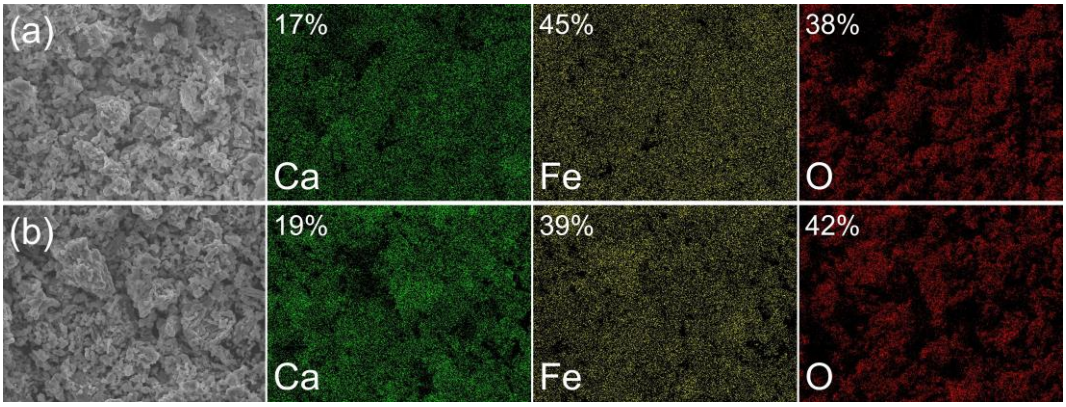

Figure 3.3 EDS elemental mappings of (a) CFO-1.0 and (b) CFO-2.0

3.3.2. Optical properties based on UV-Vis and PL results

The optical properties of the as-fabricated CFO photocatalysts were investigated by UV-Vis absorption spectra in Figure 3.4. CFO-Urea and CFO-Glucose show similar absorption onsets at wavelength of 650 nm in Figure 3.4(a). Compared to CFO-Urea, there is an absorption improvement above 650 nm for CFO-Glucose. CFO samples obtained at different fuel ratios also show different absorbance performance. CFO-0.5 sample presents lower absorbance ability than CFO-1.0 sample in the absorbance range of 500 to 650 nm. CFO-1.0 and CFO-2.0 show similar absorbance in the range of 500 to 650 nm. The absorbance above 650 nm of CFO-1.0 is higher than that of CFO-2.0. All bandgaps of photocatalysts were calculated through the Tauc plots [29]. As shown in Figure 3.4(c) and (d), the bandgap values for CFO-Urea, CFO-Glucose, CFO-0.5, CFO-1.0, and CFO-2.0 are 1.91, 1.90, 1.92, 1.90, and 1.91 eV, respectively.

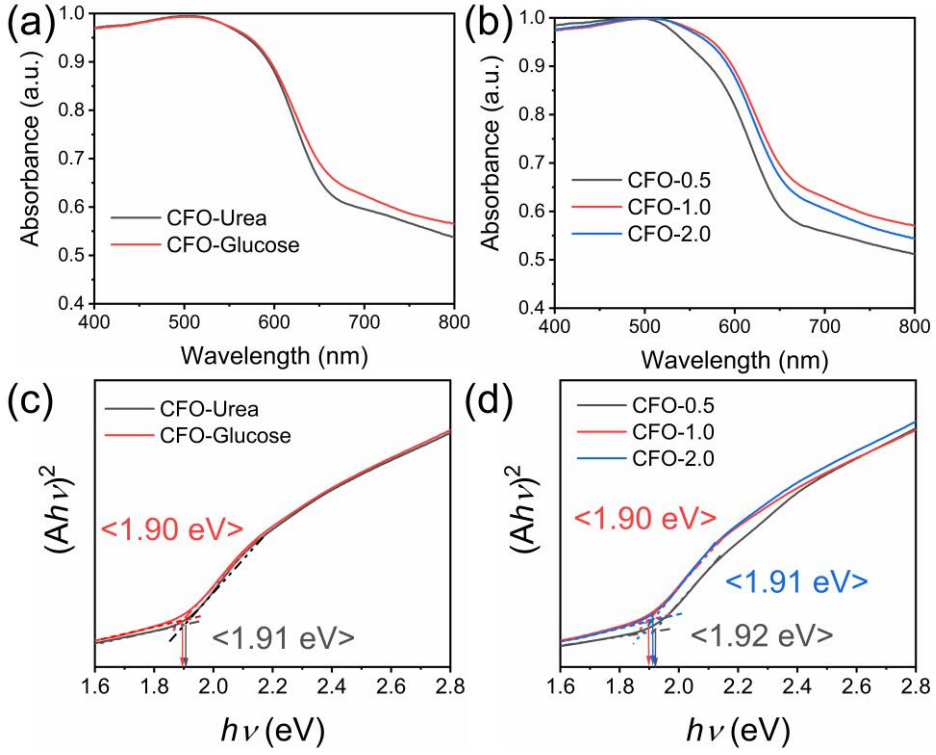

Figure 3.4 UV-Vis spectra of all CFO samples

PL emission spectra were obtained to show the charge recombination and separation behaviors of CFO samples. There are three main peaks at 467, 557, and 620 nm, respectively. The intensity of the PL spectra provides the information about photo-induced charge recombination. The higher the peak intensity, the more serious the charge recombination. The peak intensity of CFO-Urea is higher than that of CFO-Glucose, which means the more serious charge recombination of CFO-Urea than that of CFO-Glucose. In all photocatalysts obtained from various fuel ratios, CFO-1.0 exhibits the lowest peak intensity, which means that CFO-1.0 presents the best charge separation efficiency.

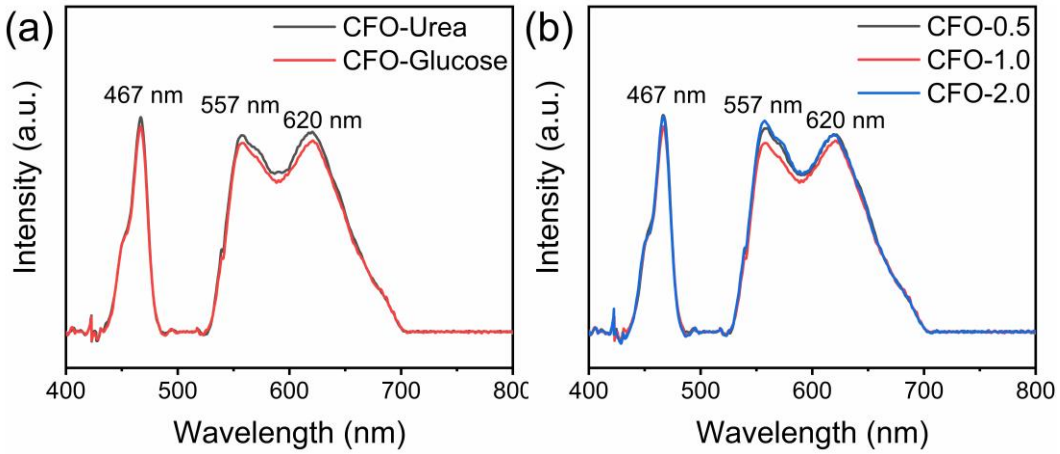

Figure 3.5 PL spectra of all CFO smaples

3.3.3. Surface state analysis based on XPS data

XPS data were collected to investigate the surface chemical composition and electronic valence state of CFO samples. The presence of Ca and Fe was confirmed by Figure 3.6(a) and (b), respectively. It is well known that the relative content of oxygen vacancy play a significant role in photocatalytic applications. The peaks related to metal-oxygen bonds from lattice (O_L) and oxygen vacancy (O_V) are two important factors influenced the photocatalytic performance of photocatalysts. The higher ratio of O_V in CFO-Urea than CFO-Glucose, resulting in lower photocatalytic performance of CFO-Urea than CFO-Glucose, as shown in Figure 3.6(c). Meanwhile, CFO-1.0 shows the lowest ratio of O_V

among samples prepared through different fuel ratios, as shown in Figure 3.6(d).

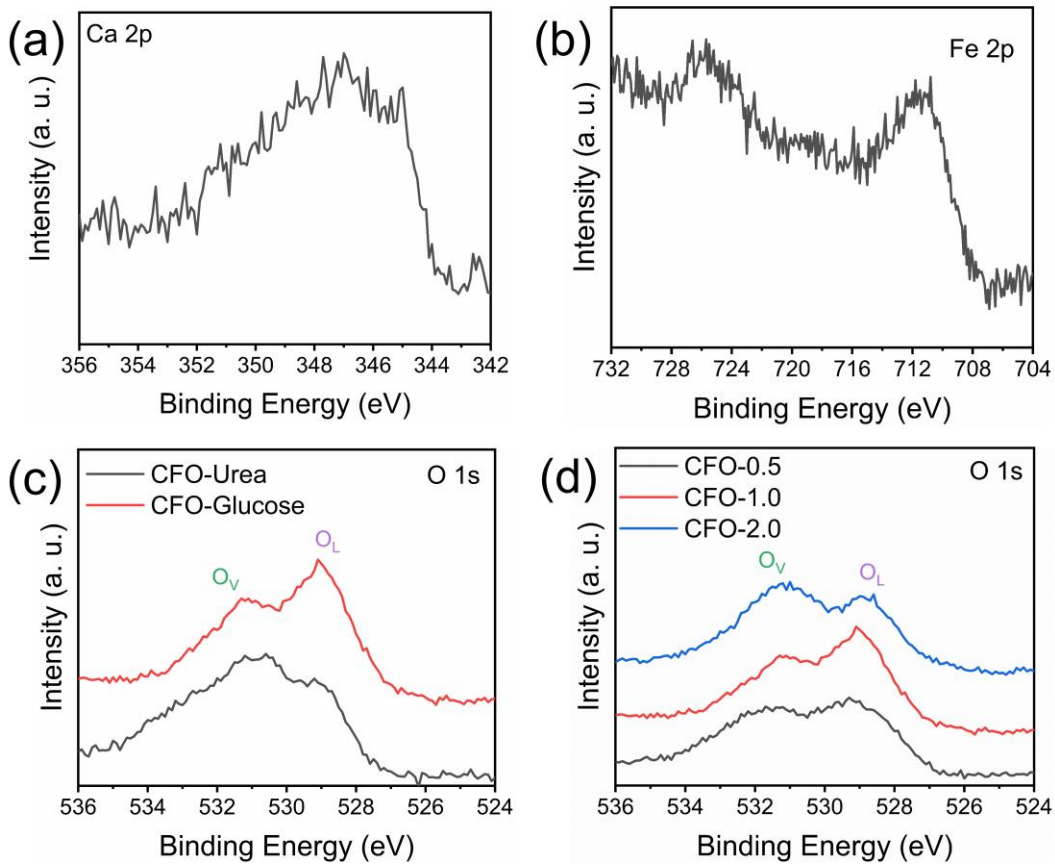

Figure 3.6 High-resolution XPS spectra of CFO-1.0 (a) Ca 2p and (b) Fe2p. O 1s spectra of (c) different fuels and (d) different fuel ratios.

3.3.4. Photocatalytic dye degradation

MB solution degradation experiments under irradiation were performed to indicate the photocatalytic properties of all CFO samples. The related data were shown in Figure 3.7. The MB degradation of CFO-Glucose is faster than that of CFO-Urea in Figure 3.7(a). For photocatalysts with different fuel ratios, CFO-1.0 presents the fastest MB degradation speed. More details about kinetics were calculated by plotting -ln(C/C_0) *vs*. time curves in Figure 3.7(c) and (d). Further, the kinetic constant *k* was calculated from the slop value of the kinetic curves. The kinetic constant values for CFO-Urea and CFO-Glucose are 0.00123 and 0.00372 min^{-1}, respectively. The kinetic constant of CFO-Glucose is three times that of CFO-Glucose. Meanwhile, the kinetic constant of CFO-1.0 (0.00372 min^{-1}) is higher

than that of CFO-0.5 (0.00176 min^{-1}) and CFO-2.0 (0.00249 min^{-1}). This is maybe because of the efficient charge separation and surface recombination and suitable amount of oxygen vacancy in CFO-1.0 sample.

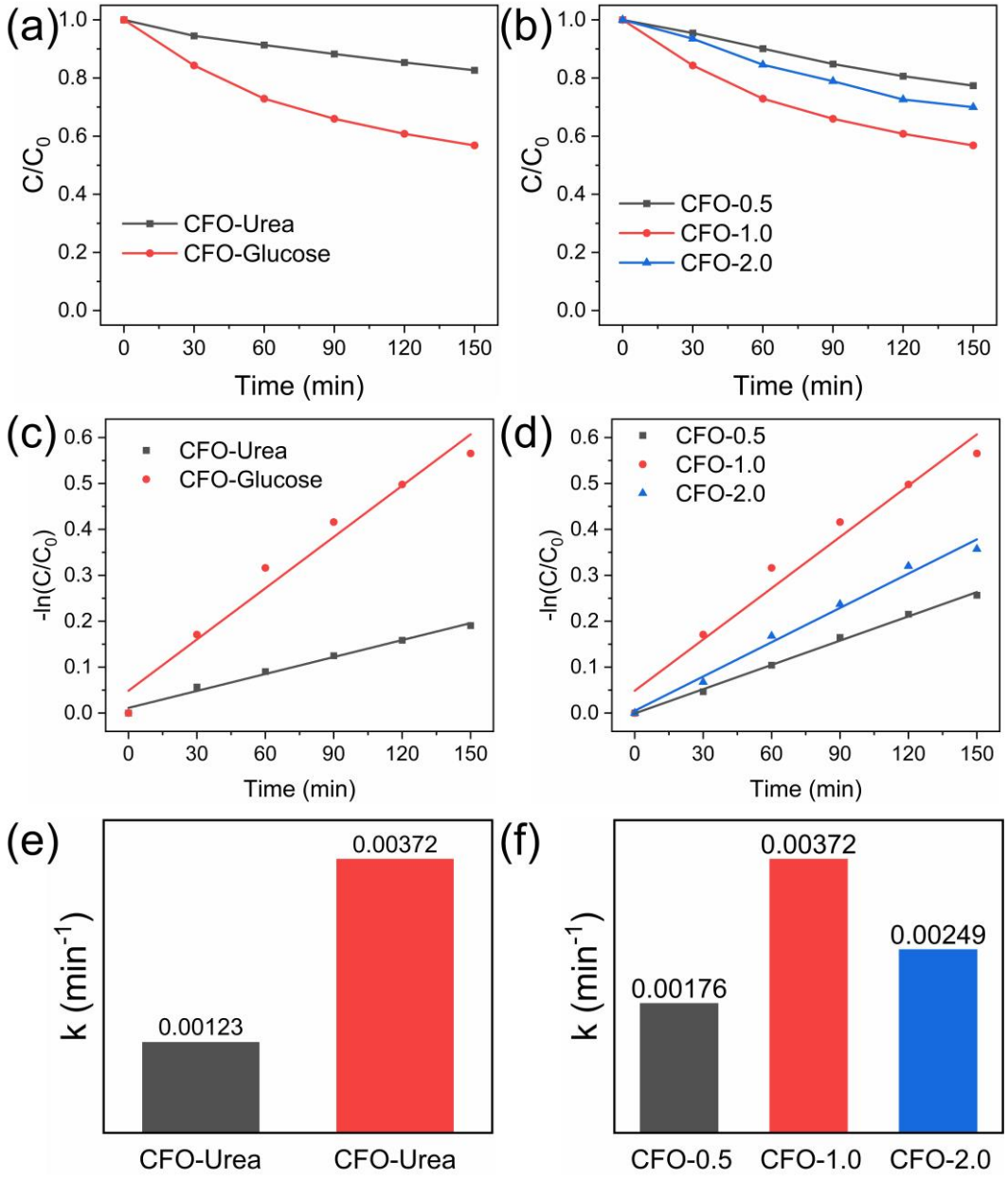

Figure 3.7 Photocatalytic degradation of MB by (a) different fuels samples and (b) different fuel ratios samples; (c) and (d) the kinetics fitting plots; (e) and (f) the kinetic constant *k*.

3.4. Conclusions

In summary, we have successfully fabricated CFO samples using urea and glucose as fuels, respectively. CFO-Glucose shows smaller crystallite sizes than CFO-Urea. We also fully investigated the effect of fuel ratios on the final products by SCS method using glucose as fuel. The XRD results clearly show that CFO-1.0 presents the smaller crystallite sizes. PL and XPS results show that CFO-1.0 present high separation efficiency and suitable amount of oxygen vacancy on the surface, resulting the best kinetic constant of 0.00372 min^{-1} among all CFO samples.

References

1. R. R. Kondakindi, K. Karan, and B. A. Peppley. A simple and efficient preparation of $LaFeO_3$ nanopowders by glycine–nitrate process: Effect of glycine concentration. *Ceramics International*. **2012** (1) 449-456.
2. G. Sierra Gallego, N. Marín Alzate, and O. Arnache. A novel $LaFeO_{3-X}N_X$ oxynitride. Synthesis and characterization. *Journal of Alloys and Compounds*. **2013** 163-169.
3. A. Laobuthee, S. Wongkasemjit, E. Traversa, et al. $MgAl_2O_4$ spinel powders from oxide one pot synthesis (OOPS) process for ceramic humidity sensors. *Journal of the European Ceramic Society*. **2000** (2) 91-97.
4. M. Su, C. He, V. K. Sharma, et al. Mesoporous zinc ferrite: Synthesis, characterization, and photocatalytic activity with H_2O_2/visible light. *Journal of Hazardous Materials*. **2012** 95-103.
5. H.-q. Jiang, H. Endo, H. Natori, et al. Fabrication and photoactivities of spherical-shaped $BiVO_4$ photocatalysts through solution combustion synthesis method. *Journal of the European Ceramic Society*. **2008** (15) 2955-2962.
6. S. J. Kim, T. Akbay, J. Matsuda, et al. Strain effects on oxygen reduction activity of Pr_2NiO_4 caused by gold bulk dispersion for low temperature solid oxide fuel cells. *ACS Applied Energy Materials*. **2019** (2) 1210-1220.
7. S. Chandrasekaran, C. Bowen, P. Zhang, et al. Spinel photocatalysts for environmental remediation, hydrogen generation, CO_2 reduction and photoelectrochemical water splitting. *Journal of Materials Chemistry A*. **2018** (24) 11078-11104.
8. A. Kudo and Y. Miseki. Heterogeneous photocatalyst materials for water splitting. *Chemical Society Reviews*. **2009** (1) 253-278.

9. F. E. Osterloh. Inorganic materials as catalysts for photochemical splitting of water. *Chemistry of Materials*. **2008** (1) 35-54.
10. H. T. Dereje, D. Ralf, C. U. Anna, et al. Photoelectrochemical and theoretical investigations of spinel type ferrites ($M_xFe_{3-x}O_4$) for water splitting: A mini-review. *Journal of Photonics for Energy*. **2016** (1) 1-25.
11. E. Z. Hegazy, S. A. Kosa, I. H. Abd Elmaksod, et al. Preparation, characterization and photocatalytic evaluation of aluminum doped metal ferrites. *Ceramics International*. **2019** (6) 7318-7327.
12. M. Israr, J. Iqbal, A. Arshad, et al. Sheet-on-sheet like calcium ferrite and graphene nanoplatelets nanocomposite: A multifunctional nanocomposite for high-performance supercapacitor and visible light driven photocatalysis. *Journal of Solid State Chemistry*. **2021** 121646.
13. A. Syed, A. H. Bahkali, and A. M. Elgorban. Enhanced antibacterial and visible light driven photocatalytic activity of $CaFe_2O_4$ doped CdO heterojunction nanohybrid particles prepared by sono-chemical method. *Optical Materials*. **2021** 110595.
14. K. S, P. Sathishkumar, P. N, et al. Heterogeneous sonocatalytic activation of peroxomonosulphate in the presence of $CoFe_2O_4/TiO_2$ nanocatalysts for the degradation of acid blue 113 in an aqueous environment. *Journal of Environmental Chemical Engineering*. **2020** (5) 104024.
15. P. Garcia-Muñoz, F. Fresno, V. A. de la Peña O'Shea, et al. Ferrite materials for photoassisted environmental and solar fuels applications. *Topics in Current Chemistry*. **2019** (1) 6.
16. L. Huang, Z. Fan, X. Li, et al. Facile synthesis of $CaFe_2O_4$ nanocubes for formaldehyde sensor. *Materials Letters*. **2021** 129351.

17. Y. Zhu, C. Peng, Z.-F. Gao, et al. Hydrothermal synthesis of $CaFe_2O_4$/α-Fe_2O_3 composite as photocatalyst and its photocatalytic activity. *Journal of Environmental Chemical Engineering*. **2018** (2) 3358-3365.
18. M. Goodarzi, S. Joukar, D. Ghanbari, et al. $CaFe_2O_4$-ZnO magnetic nanostructures: Photo-degradation of toxic azo-dyes under UV irradiation. *Journal of Materials Science: Materials in Electronics*. **2017** (17) 12823-12838.
19. M. Bhowmik, A. Debnath, and B. Saha. Fabrication of mixed phase $CaFe_2O_4$ and $MnFe_2O_4$ magnetic nanocomposite for enhanced and rapid adsorption of methyl orange dye: statistical modeling by neural network and response surface methodology. *Journal of Dispersion Science and Technology*. **2020** (13) 1937-1948.
20. B.-j. Xue, J. Luo, F. Zhang, et al. Biodiesel production from soybean and Jatropha oils by magnetic $CaFe_2O_4$-$Ca_2Fe_2O_5$-based catalyst. *Energy*. **2014** 584-591.
21. N. H. Sulaiman, M. J. Ghazali, J. Yunas, et al. Synthesis and characterization of $CaFe_2O_4$ nanoparticles via co-precipitation and auto-combustion methods. *Ceramics International*. **2018** (1) 46-50.
22. M. Bhowmik, A. Debnath, and B. Saha. Fabrication of mixed phase calcium ferrite and zirconia nanocomposite for abatement of methyl orange dye from aqua matrix: Optimization of process parameters. *Applied Organometallic Chemistry*. **2018** (12) e4607.
23. C. Shifu, Z. Wei, L. Wei, et al. Preparation, characterization and activity evaluation of p-n junction photocatalyst p-$CaFe_2O_4$/n-ZnO. *Chemical Engineering Journal*. **2009** (1) 466-473.

24. A. Behera, D. Kandi, S. Martha, et al. Constructive interfacial charge carrier separation of a p-$CaFe_2O_4$@n-$ZnFe_2O_4$ heterojunction architect photocatalyst toward photodegradation of antibiotics. *Inorganic Chemistry*. **2019** (24) 16592-16608.
25. H. Gao, H. Yang, and S. Wang. Comparative study on optical and electrochemical properties of MFe_2O_4 (M = Mg, Ca, Ba) nanoparticles. *Transactions of the Indian Ceramic Society*. **2018** (3) 150-160.
26. Z. Zhang and W. Wang. Solution combustion synthesis of $CaFe_2O_4$ nanocrystal as a magnetically separable photocatalyst. *Materials Letters*. **2014** 212-215.
27. N. Sheng, C.-g. Han, C. Zhu, et al. One-step solution combustion synthesis of $K_{0.5}Na_{0.5}NbO_3$ powders at a large-scale. *Ceramics International*. **2018** (15) 18279-18284.
28. Z. Zhang, M. F. Hossain, and T. Takahashi. Photoelectrochemical water splitting on highly smooth and ordered TiO_2 nanotube arrays for hydrogen generation. *International Journal of Hydrogen Energy*. **2010** (16) 8528-8535.
29. P. Makuła, M. Pacia, and W. Macyk. How to correctly determine the band gap energy of modified semiconductor photocatalysts based on UV–Vis spectra. *The Journal of Physical Chemistry Letters*. **2018** (23) 6814-6817.

Chapter 4 Molten Salt-assisted Shape Modification of $CaFe_2O_4$ Nanorods for Highly Efficient Photocatalytic Degradation of Methylene Blue

4.0. Brief summary

In this chapter, $CaFe_2O_4$ nanorods (CFO NRs) and aggregated particles (CFO APs) were fabricated with and without the help of molten salt-assisted shape modification, respectively. CFO APs present inferior photocatalytic performance due to the plenty of grain boundaries which hinder photogenerated charges transfer and act as charge recombination sites. Molten salt-assisted modification can easily change the shape of CFO NRs and significantly suppresses the formation of grain boundaries, facilitating photogenerated charges separation and transfer for highly efficient photocatalytic degradation of methylene blue (MB). Surface state investigation indicates a decreased amount of unsuitable oxygen vacancies and defects in CFO NRs, which is beneficial in alleviating the recombination of photogenerated charges in CFO NRs. The CFO NRs show a ten-time increased kinetic constant of MB degradation from 0.0013 to 0.013 min^{-1} by virtue of the alleviative charge recombination.

4.1. Introduction

With the massive use of organic dyes in industrial production, the residue of coloring wastewater has become a severe environmental problem, which is threatening drinking water safety and human health [1]. Among the various technologies used for pigment degradation, the semiconductor-based photocatalytic degradation is emerging as a high-efficiency and environmentally friendly approach because it only uses photocatalyst and solar energy [2, 3]. Therefore, the research and development of highly efficient photocatalyst becomes an urgent task on account of environmental remediation [4]. TiO_2 as the first investigated photocatalyst has been widely used in various fields, such as environmental pollutant degradation [5], water splitting [6], hazardous elements reduction [7], air treatment [8] and CO_2 reduction [9]. Nevertheless, TiO_2 with wide bandgap (3.2eV)

only shows high photocatalytic efficiency under ultraviolet (UV) light irradiation which only accounts for 4% of the solar spectrum [10, 11]. Hence, it is necessary to develop visible-light-active and property stable semiconductor photocatalysts with narrow bandgap to take full advantage of solar irradiation.

In recent years, spinel ferrite (MFe_2O_4, M represent divalent metal atoms such as Ca^{2+}, Zn^{2+}, Ba^{2+}, Co^{2+}, Mg^{2+}, Ni^{2+}, etc.) as an emerging visible-light-driven photocatalyst has been widely utilized as an attractive photocatalyst in many fields due to its relatively narrow bandgap (approximately 2.0 eV), low cost, and superior durability [12, 13]. Among them, $CaFe_2O_4$ (CFO) is an extraordinary one because it is a p-type semiconductor [14]. A great number of studies showed that the p-n heterojunction structure in the semiconductor is beneficial for the effective separation of photogenerated charge carrier pairs by virtue of the built-in electric fields at the interface [15-18]. Although plenty of semiconductor photocatalysts have been well developed, studies on p-type semiconductor photocatalysts are still limited. CFO catalysts have been successfully synthesized by numerous synthesis methods such as solution combustion synthesis [19], pulsed laser deposition [20], solid-state reaction [21], co-precipitation method [22], and so on. Various modifications have been applied for the performance enhancement of photocatalysts, such as structure improvement by metal doping [23], charge separation enhancement by forming heterojunction [24-28], and surface state adjustment through co-catalyst deposition [29]. Some studies indicated that shape modification is a feasible method for the improvement of photocatalytic performance of photocatalysts due to the efficient charge separation or increased surface area [30, 31]. However, the performance improvement of CFO by shape modification is still rare.

In addition, the high fabrication temperature is still an important factor limiting the

practical application of CFO samples. On the one hand, high temperature calls for higher requirements on the reactor. On the other hand, at high calcination temperature, nanoparticles may aggregate together to form grain boundaries, which will hinder the transfer and separation of photogenerated charges and affect their photocatalytic properties [32]. The molten salt synthesis method presents unique advantages in catalyst preparation, especially for materials with higher synthesis temperatures [33]. This method can not only lower the liquid phase forming temperature by the incorporation of low melting point inorganic salts, but also easily modify samples with the specific morphologies, such as rods [34, 35], wires [36], plates [37], flowers [38], etc. Recently, Liu et al. reported the synthesis of rod-form CFO using a NaCl-KCl molten salt method [39]. However, the studying on the effect of molten salt synthesis method on the photocatalysts structure and photocatalytic property is still limited.

Herein, CFO catalyst precursors were first synthesized by a facile polymerizable complex method followed by molten salt-assisted shape modification. The photocatalytic degradation studies of methylene blue (MB) solution were conducted under simulated solar irradiation. Compared to CFO APs, the CFO NRs show a ten-time enhanced degradation kinetic constant from 0.0013 to 0.013 min^{-1} by virtue of the single crystalline feature and the decreased amount of unsuitable oxygen vacancies and defects by detailed microstructural characterization and surface state investigation. The excellent enhancement of degradation performance paves the way for improving photocatalyst performance by molten salt-assisted shape modification.

4.2. Experimental

4.2.1. Chemical reagents

Calcium nitrate tetrahydrate ($Ca(NO_3)_2 \cdot 4H_2O$, 98.0%), iron nitrate enneahydrate

($Fe(NO_3)_3 \cdot 9H_2O$, 99.0%), citric acid monohydrate ($HOC(COOH)(CH_2COOH)_2 \cdot H_2O$, 99.5%), and ethylene glycol ($HOCH_2CH_2OH$, 99.0%) were purchased from Fujifilm Wako Pure Chemical Corporation. Potassium chloride (KCl, 99.5%) and sodium chloride (NaCl, 100%) were purchased from Kanto Chemical Co., Inc. All chemical reagents were directly used without further purification. During the whole fabrication process, deionized (DI) water was used.

4.2.2. Preparation of catalysts

Target catalysts were fabricated by two processes, including the CFO precursor fabrication process via a polymerizable complex method and crystallinity improvement or shape modification process [39]. For CFO precursor fabrication, 20 mmol of $Ca(NO_3)_2 \cdot 4H_2O$, 40 mmol of $Fe(NO_3)_3 \cdot 9H_2O$, and 40 mmol of citric acid monohydrate were sequentially added to a mixed solution of DI (20 mL) and ethylene glycol (8 mL). After stirring for 30 min at ambient temperature, the transparent CFO precursor solution was formed. After water evaporation and polyesterification at 130 ^oC for 20 h, the transparent solution became a dark green sphere in the crucible, followed by calcination at 500 ^oC for 2 h. The as-fabricated CFO precursor was fully ground and reserved for the following process. To improve crystallinity, as-fabricated CFO precursor was calcined in air at 900 ^oC for 6 h in a crucible. Due to the high calcination temperature, CFO precursors were aggregated together to form CFO aggregated particles, named as CFO APs. For CFO nanorods (CFO NRs) fabrication, 1.119 g of CFO precursors were blended with 1.873 g of KCl and 1.461 g of NaCl and fully grounded. The mixture was spread flat in the crucible with a square bottom, the thickness of the sample was about 3 mm. Then performed the same calcination process as the CFO APs fabrication process. After cooling to room temperature, as-synthesized samples were washed by DI under strong stirring for 12 h.

After centrifugation and drying at 50 ^{o}C, pure CFO NRs was obtained. The overview of the synthetic process for CFO APs and CFO NRs is illustrated in Figure 4.1.

4.2.3. Characterization

X-ray diffraction (XRD) patterns of as-fabricated catalysts were performed for the crystal structure study at a diffractometer (Miniflex 600, Rigaku) using Cu Kα radiation (λ=1.54060 Å). The surface morphology of samples was investigated by a scanning electron microscope (SEM) using JSM-7001FA (JEOL, Japan). Further detailed morphology and microstructure of the as-fabricated samples were studied through transmission electron microscopy (TEM) and high-resolution transmission electron microscopy (HRTEM) using JEM-2000FX (JEOL, Japan) and JEM-2010F (JEOL, Japan) at both operating voltage of 200 kV, respectively. The selected area electron diffraction (SAED) patterns were obtained at JEM-2000FX (JEOL, Japan). The Brunauer-Emmett-Teller (BET) specific surface areas were obtained by Autosorb 6AG based on the nitrogen adsorption isotherms at 77 K. An exhaust treatment was performed at 120 ^{o}C for 4 h. The surface chemical state analysis was carried out at an X-ray photoelectron spectrometer (JEOL, JPS-9200) operated at 10 kV and 10 mA. A UV-Vis spectrometer (JASCO V-770) equipped with an integrating sphere attachment was performed to test the optical properties of samples. The photoluminescence (PL) spectra were collected through a luminescence spectrometer (JASCO FP-8600).

4.2.4. Photocatalytic performance experiments

The photocatalytic performance of as-fabricated CFO APs and CFO NRs was characterized by MB solution degradation experiments. Typically, 50 mL MB solution (1 mg/L) was chosen as degradation target. Before irradiation, the solution containing as-fabricated photocatalysts of 50 mg was magnetically stirred for 30 min in the dark to

achieve adsorption-desorption equilibrium. A simulated solar light (HAL-320W, Asahi spectra) as a light source was used to provide an irradiation intensity of 100 mW/cm^2 from the top of the solution. Approximately 3 mL solution was taken every 30 min and centrifuged to remove the catalyst. The absorption spectra of the residual solution were collected by UV-Vis spectrometer (JASCO V-770). The peak intensity at 664 nm was chosen to indicate the concentration of solution. The residual relative amount was calculated according to the following Equation (4.1).

$$\text{Residual relative amount} = \frac{C}{C_0} \tag{4.1}$$

where C_0 and C represent the concentration of MB solution after stirring in the dark and residual concentration during irradiation at various time intervals, respectively.

4.3. Results and discussion

4.3.1. Fabrication of CFO APs and CFO NRs

As shown in Figure 4.1, CFO APs and CFO NRs were fabricated through two processes. CFO NRs were obtained by the NaCl and KCl molten salts-assisted shape modification method. CFO APs were just synthesized without adding molten salts. Compared with the conventional solid state approach with reaction temperature of 1100 ^{o}C [18], low-melting-point salt-assisted synthesis method can reduce the reaction temperature by 200 ^{o}C to 900 ^{o}C. XRD patterns of CFO APs and CFO NRs are presented in Figure 4.2. Both CFO APs and CFO NRs samples show sharp diffraction peaks, indicating the high crystallinity of as-fabricated samples. In addition, the background line noise was from the fluorescence of the Fe atoms [40]. All diffraction peaks can be perfectly matched to crystal plane of orthorhombic phase $CaFe_2O_4$ (JCPDS NO. 03-065-1333). The (302)/(210) peak intensity ratios of CFO APs and CFO NRs are 1.29 and 2.15, respectively. The different (302)/(210)

peak intensity ratios of as-fabricated samples indicate different product shapes, showing that the addition of molten salt can promote the shape modification of CFO as discussed in the following SEM results.

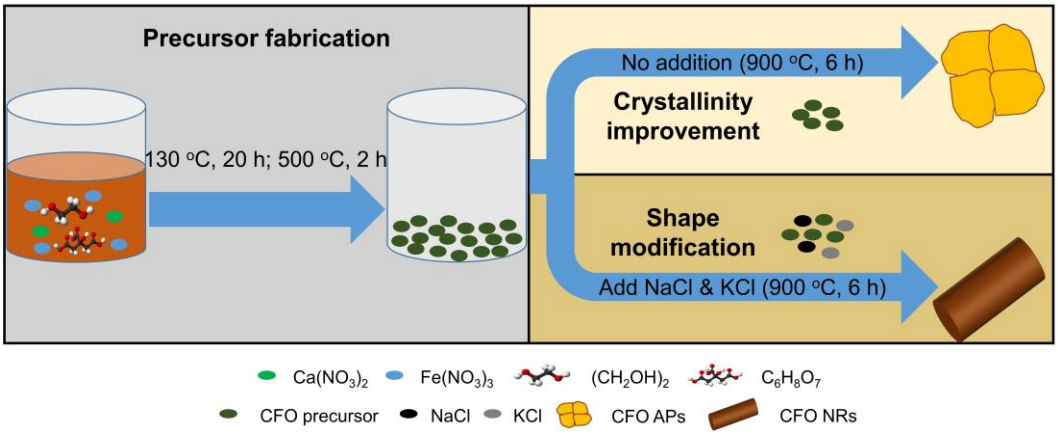

Figure 4.1 Schematics diagram of the synthesis process of CFO APs and CFO NRs.

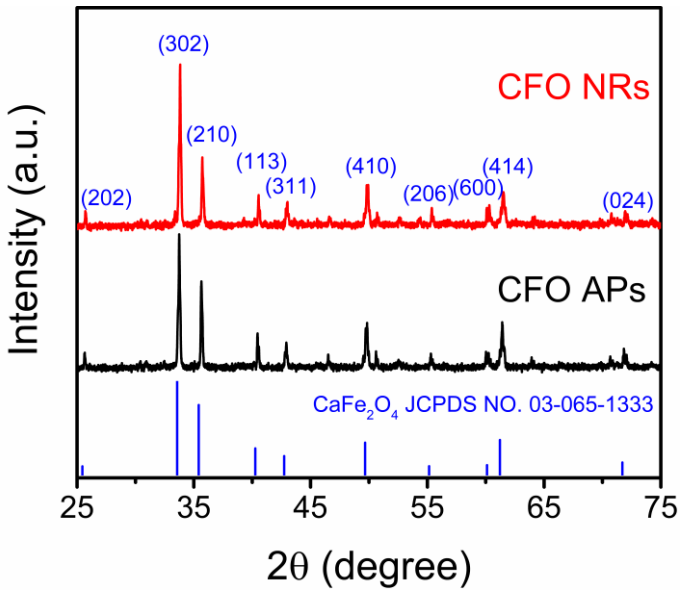

Figure 4.2 XRD patterns of CFO APs and CFO NRs.

4.3.2. Surface morphology

The typical surface morphologies of CFO APs and CFO NRs are shown in Figure 4.3. As shown in Figure 4.3(a), CFO APs are aggregated together by few nanoparticles due to the high calcination temperature, which is constant with other materials fabricated at high calcination temperature [41, 42]. The high magnification inset in Figure 4.3(a) further

clearly indicates that the aggregation is formed by several nanoparticles with widths of 200 to 400 nm in different directions. The junction in CFO APs may act as the place of photogenerated charge carriers recombination, which will result in low charge migrate rate and inferior charge separation efficiency. In contrast, CFO NRs show straight nanorod morphology with a smooth surface, as shown in Figure 4.3(b) and the lengths are about several micrometers. The widths of the CFO NRs are also about 200 to 400 nm as shown in the high magnification inset of Figure 4.3(b). In summary, as-fabricated CFO APs and CFO NRs catalysts have similar widths but different lengths under the same calcination temperature. Figure 4.4 shows the photos of CFO APs and CFO NRs before and after the calcination process. There is almost no difference except color for CFO APs by a conventional high temperature calcination method without the introduction of molten salts, indicating no molten phase formed during the calcination process. In contrast, obvious region changes that few separated parts formed in final products can be seen for CFO NRs before and after calcination process, which indicates that molten phases were formed during the high temperature calcination process. As mentioned above, the introduction of molten salt has two main effects. On the one hand, the addition of low melting point inorganic salt can easily form the liquid phase to improve the mobility during calcination process. On the other hand, the introduction of molten KCl and NaCl facilitates the formation of nanorods by changing the energy of specific crystal surface of CFO NRs [39].

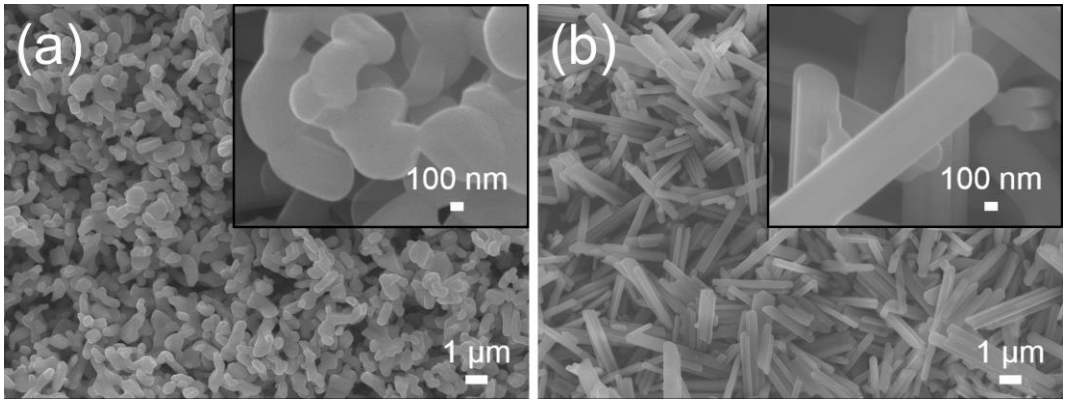

Figure 4.3 SEM images of (a) CFO APs and (b) CFO NRs. Insets are the corresponding images under high magnification.

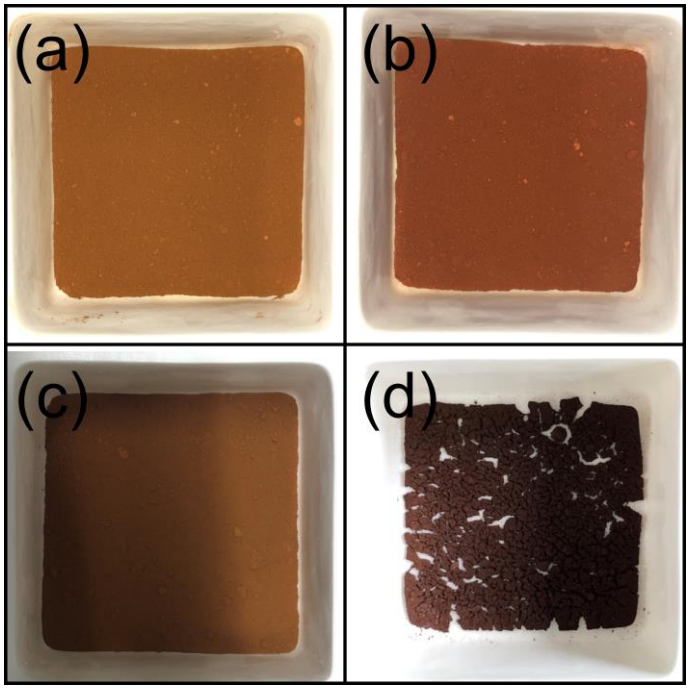

Figure 4.4 Optical pictures of CFO APs (a) before and (b) after calcination synthesis process and CFO NRs (c) before and (d) after calcination synthesis process.

4.3.3. Microstructure characterization

The detailed microstructure characterizations were further performed by TEM, HRTEM and SAED, as shown in Figure 4.5. Figure 4.5(a) demonstrates the typical image of CFO APs. It can be clearly seen that some nanoparticles gather together due to high calcination temperature. Figure 4.5(b) shows the HRTEM image of CFO APs. The lattice spacing values of 0.535 and 0.267 nm correspond to the (002) and (302) planes of CFO APs,

respectively. In addition, a clear grain boundary in CFO APs can be seen from HRTEM image. The grain boundary may hinder the photogenerated charge transfer and act as the recombination site. In contrast, CFO NRs in Figure 4.5(c) show a nanorod morphology with smooth surface. Meanwhile, the HRTEM images in Figure 4.5(d) and (e) clearly show that there are almost no obvious grain boundaries not only at the ends of the CFO NRs but also at the main body of the CFO NRs. The lattice spacing of 0.253 nm corresponds to (210) plane of $CaFe_2O_4$, indicating the growth direction of CFO NRs is along [210] direction. In addition, the SAED patterns obtained at f, g, and h parts (both ends and main body) of CFO NRs in Figure 4.5(c) show uniform patterns in Figure 4.5(f-h), which means that the as-fabricated CFO NRs are single crystalline. These features of grain boundary free and single crystalline of CFO NRs provide a free path for the charge carrier transfer and show an alleviative charge recombination. In summary, compared with the traditional method (high temperature calcination without molten salt) for improving crystallinity, the molten salt method can not only enhance the crystallinity, but also modify its shape.

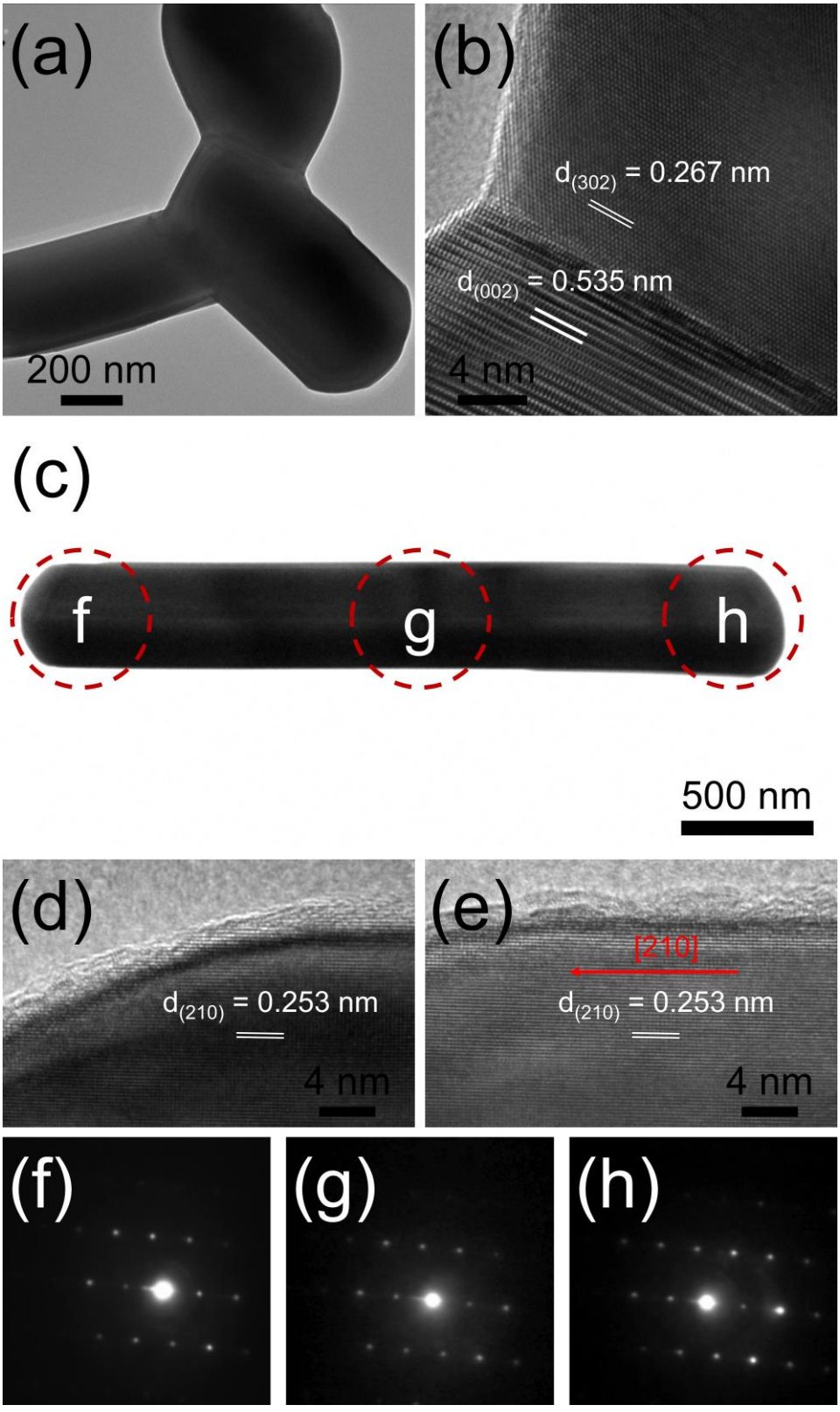

Figure 4.5 TEM images of (a) CFO APs and (c) CFO NRs. HRTEM images of (b) CFO APs, (d) the end and (e) the main body of CFO NRs. (f-h) SAED patterns of the selected parts in (c).

4.3.4. Surface area and pore characterization

The surface area and pore characterization of CFO APs and CFO NRs were investigate by conducting the N_2 adsorption and desorption isotherms as shown in Figure 4.6. As shown in Figure 4.6(a), the CFO APs possess a type IVa isotherm with a hysteresis loop of type H3, showing the presence of inter-particular voids between nanoparticles [43, 44]. However, the CFO NRs show a type III isotherm feature. The BET specific surface areas of CFO APs and CFO NRs are 3.40 and 2.50 m^2g^{-1}, respectively. Moreover, Barrett-Joyner-Halenda (BJH) method is used to determine the pore diameter distribution as shown in Figure 4.6(b). The average pore diameters of CFO APs and CFO NRs are 2.88 and 1.49 nm, respectively. The pore volumes for CFO APs and CFO NRs are 0.0181 and 0.0127 cm^3g^{-1}, respectively. As shown in Figure 4.3, CFO APs and CFO NRs are similar in width. The lengths of CFO NRs are longer than that of CFO APs. Therefore, CFO APs have more side surface than CFO NRs in terms of specific quality samples. Moreover, the pore volume of CFO APs is higher than that of CFO NRs. So, the surface areas of CFO APs are larger than that of CFO NRs.

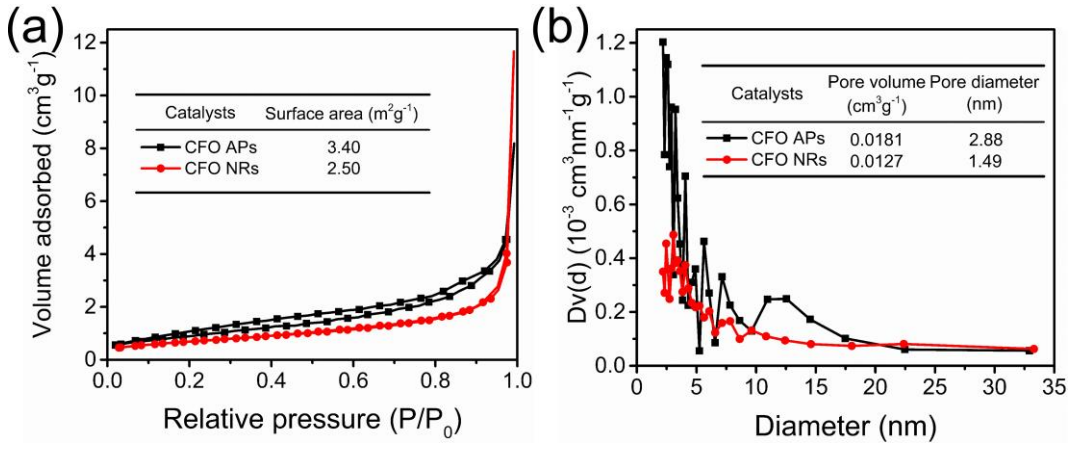

Figure 4.6 (a) The nitrogen adsorption-desorption isotherm and BET surface areas (inset). (b) BJH pore size distributions, pore volume (inset), and average pore diameter (inset) of CFO APs and CFO NRs.

4.3.5. Surface state based on XPS

Further investigation on the surface chemical composition and electronic valence state of as-fabricated samples was conducted by XPS. All the XPS data were performed calibration according to the adventitious carbon signal located at 284.8 eV [45]. The presence of Fe, O, and Ca was confirmed by the wide scan XPS spectrum in Figure 4.7(a). As shown in Figure 4.7(b), there are two peaks located at 351.7 and 348.3 eV, corresponding to Ca $2p_{1/2}$ and Ca $2p_{3/2}$, respectively, which is demonstrated as the oxidation state of +2 for Ca [46]. The Fe 2p spectra in Figure 4.7(c) present two main peaks located at around 723.8 and 710.6 eV can be assigned to Fe $2p_{1/2}$ and $2p_{3/2}$, respectively. After deconvolution, two satellite peaks at around 723.5 and 716.9 eV can be clearly seen, representing the presence of Fe^{3+} in both CFO APs and CFO NRs [47]. The two fitting peaks at 712.4 and 71.03 eV may be related to Fe at different sites [48]. Figure 4.7(d) presents the O 1s spectra of CFO APs and CFO NRs. It is well known that the state and relative content play a significant role in photocatalytic applications. Therefore, the deconvolution of O 1s spectrum was conducted to further investigate the effect of oxygen under various chemical states on photocatalytic performance. The deconvoluted peaks located at approximately 531.7 and 529.3 eV are related to the metal-oxygen bonds from lattice (O_L) and oxygen vacancy/defect (O_V), respectively [49]. The relative ratios based on the corresponding peak area values of O_V/O_L for CFO APs and CFO NRs are 42/58 and 39/61, respectively. The high ratio of O_V in CFO APs may result in low photocatalytic performance because these unsuitable oxygen vacancies or defects can act as recombination sites of photogenerated hole and electron charge carriers [50, 51]. However, that value for CFO NRs was decreased, which was beneficial to the enhancement of photocatalytic performance as mentioned below.

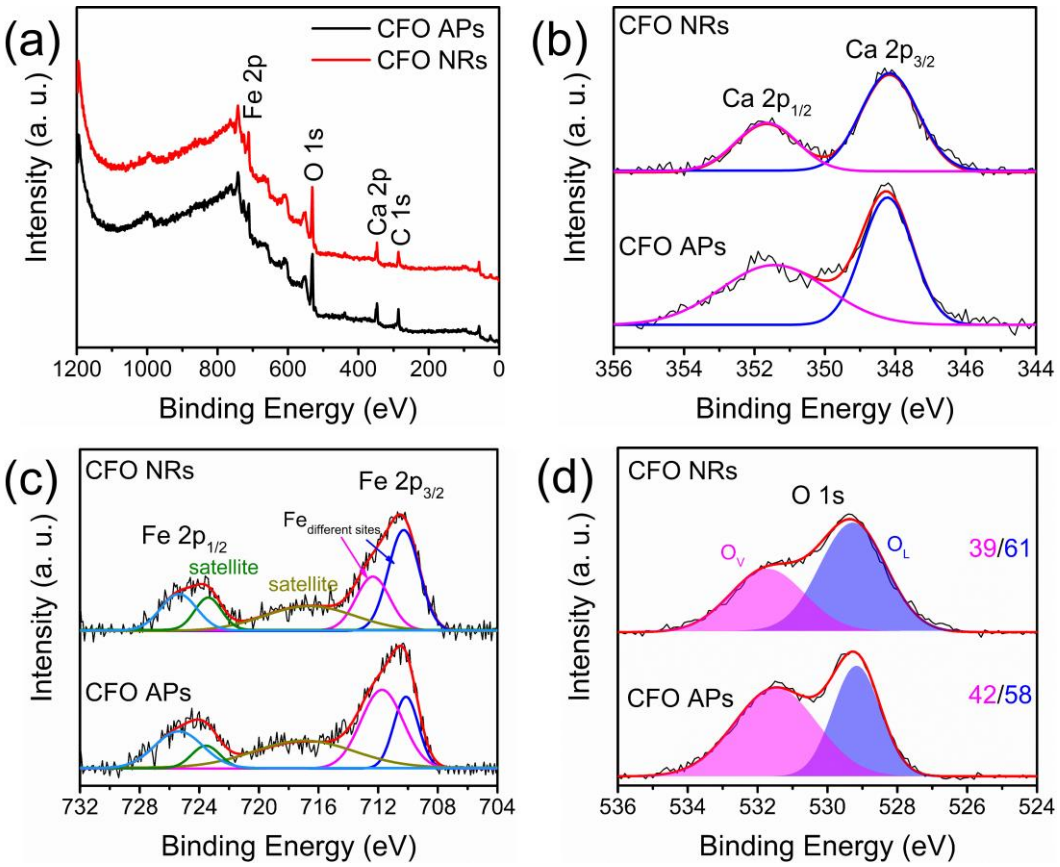

Figure 4.7(a) Wide XPS spectra; high-resolution XPS spectra of CFO APs and CFO NRs of typical elements (b) Ca 2p, (c) Fe 2p, and (d) O 1s. The area ratios of lattice-related (O_L, orange) and vacancy-related (O_V, blue) peaks are marked.

4.3.6. Optical properties

UV-Vis absorption spectra in Figure 4.8 demonstrate the optical properties of the as-fabricated photocatalyst. Both CFO APs and CFO NRs show visible light absorption onsets at wavelength of 650 nm. It can be clearly seen that there is an absorption enhancement above 650 nm for CFO NRs compared to CFO APs. However, the lifting in this range has almost no effect on the photocatalytic performance of the sample [52]. The bandgaps of photocatalysts were calculated using the Tauc plots [53] through Equation (4.2).

$$(\alpha h\nu)^{1/n} = A(h\nu - E_g) \tag{4.2}$$

where α represents the absorption coefficient, h represents the Planck constant, ν represents the photon's frequency, A is a constant, E_g is the optical bandgap energy of catalyst, and the

n value is 1/2 for the direct transition bandgap. As shown in the inset of Figure 4.8, the E_g values for CFO APs and CFO NRs are 1.95 and 1.94 eV, respectively. These bandgaps are consistent with the previously reported values [44]. Meanwhile, the bandgap values for CFO APs and CFO NRs are similar. Therefore, the bandgap values change may not be the main reason for the photocatalytic performance enhancement as discussed below.

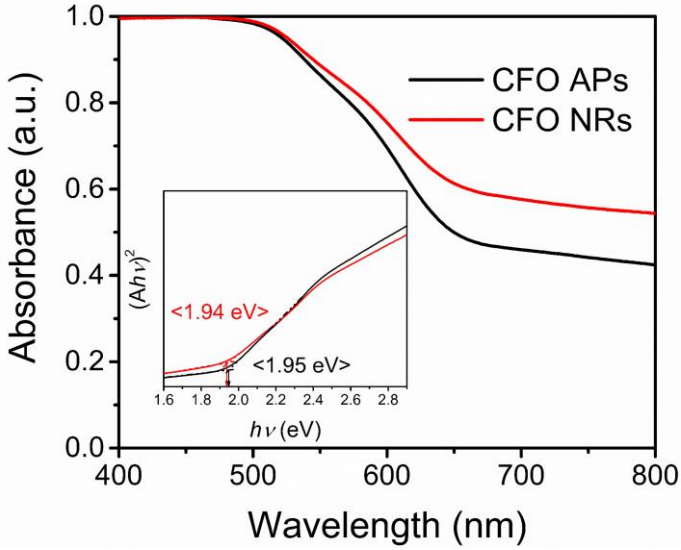

Figure 4.8 UV-Vis absorption spectra of CFO APs and CFO NRs (the inset is the corresponding direct bandgap obtained by the Tauc method).

To further investigate charge behavior of as-fabricated photocatalysts, PL emission spectra were obtained to show the separation efficiency of photogenerated charge carriers. This characterization can provide evidence for radiative recombination of photoexcited hole and electron pairs [54]. As presented in Figure 4.9, the peaks of CFO APs and CFO NRs located at 467 nm were selected for comparison. The intensity of the fluorescence peak of CFO APs was stronger than that of CFO NRs, which means more charge recombination occurs at CFO APs, resulting in relatively low photocatalytic performance of CFO APs as discussed below.

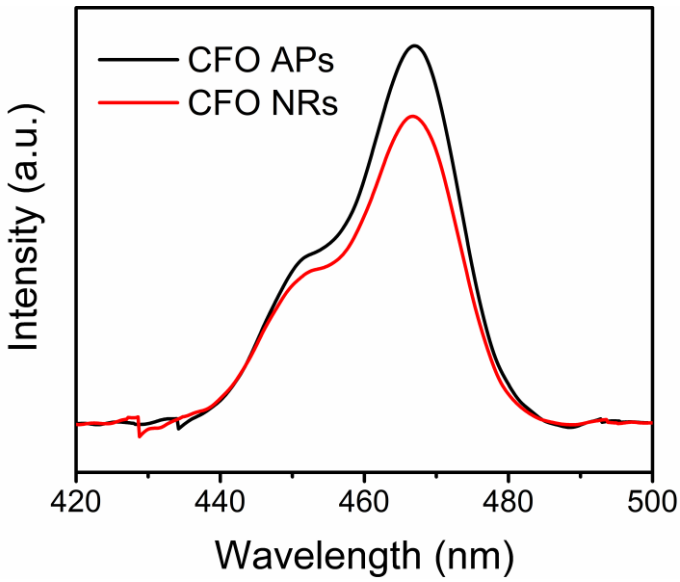

Figure 4.9 PL spectra of the photocatalysts.

4.3.7. Photocatalytic performance

The photocatalytic performance of as-fabricated catalysts was investigated by MB solution degradation experiments under simulated sunlight irradiation (AM 1.5G). Figure 4.10 (a) shows the photocatalytic degradation of MB using CFO APs and CFO NRs within 120 min. The photocatalytic degradation efficiency can be calculated using the following Equation (4.3) [55].

$$\%degradation = \left(1-\frac{C}{C_0}\right) \tag{4.3}$$

The photocatalytic degradation efficiency of CFO APs and CFO NRs are 14.1% and 77.2%, respectively. The analysis of MB degradation kinetics was further performed based on a pseudo-first-order reaction kinetics model as shown in Equation (4.4).

$$-\ln\frac{C}{C_0} = kt \tag{4.4}$$

where k and t are the apparent specific reaction time (min^{-1}) and irradiation time (min), respectively.

Figure 4.10(b) presents the corresponding pseudo-first-order kinetics fitting plots and the

comparison of the degradation rate constant *k* (inset) of CFO APs and CFO NRs. The kinetic constant values of CFO APs and CFO NRs are 0.0013 and 0.013 min^{-1}, respectively. Compared to CFO APs, the reaction kinetic constant of CFO NRs catalysts produced by molten salt assisted calcination method enhanced 10 times. The reusability of CFO NRs for MB degradation was evaluated. Figure 4.11 shows the recycling performance of CFO NRs for MB degradation. In the 4th MB degradation recycling, CFO NRs also present a kinetic constant of 0.011 min^{-1} as good kinetic constant as the fresh one. The results show that the synthesized samples have good reusability.

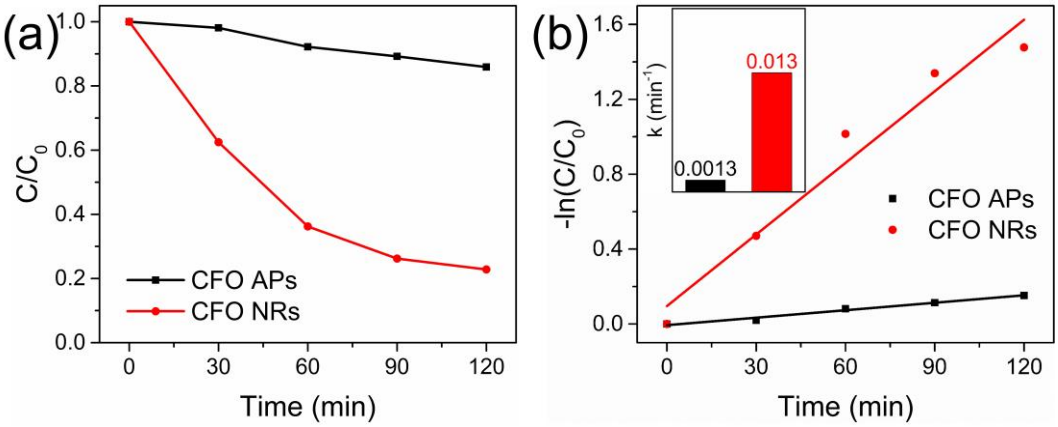

Figure 4.10 (a) Photocatalytic degradation of MB by as-prepared catalysts. (b) The corresponding pseudo-first-order kinetics fitting plots and comparison of the degradation rate constant k (inset).

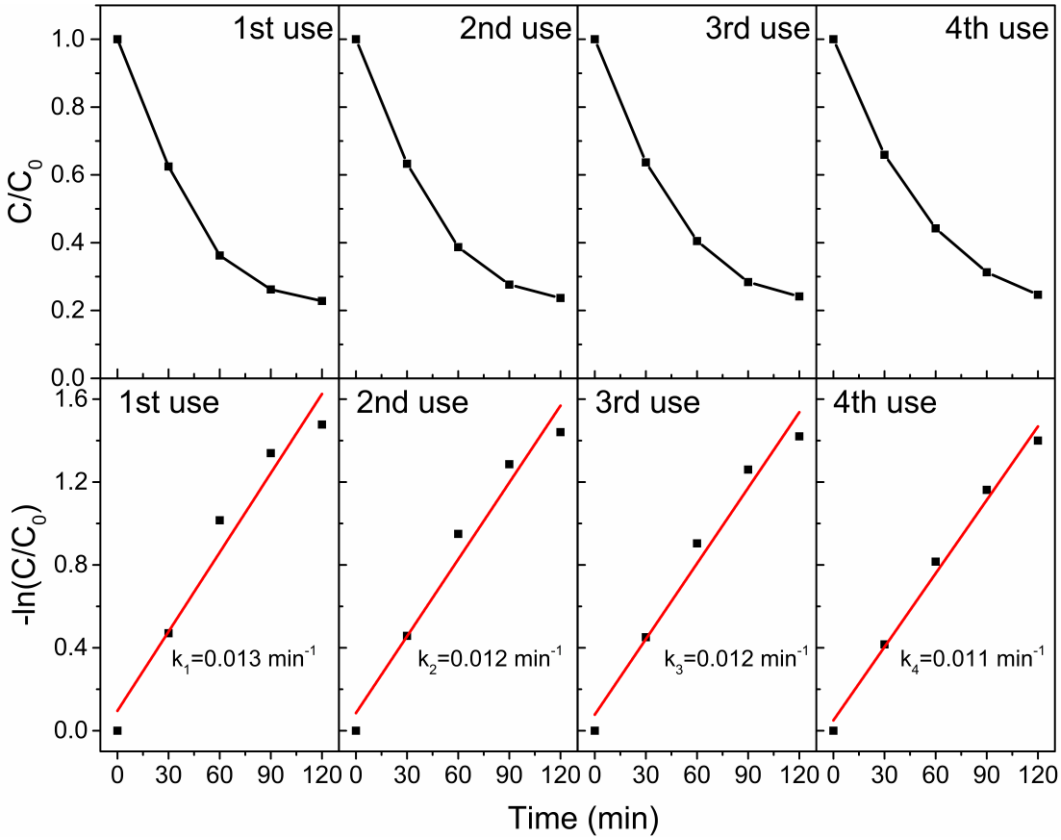

Figure 4.11 The reusability test results of (a) photocatalytic degradation and (b) kinetic constant.

To further understand the photocatalytic degradation process of MB solution and possible mechanism for the performance enhancement of CFO NRs, a brief schematic is presented in Figure 4.12. After irradiation, equal numbers of electrons and holes were formed in conduction band and valence band, respectively. The plenty of grain boundaries in CFO APs not only limit the transfer of charges, but also act as charges recombination sites. Only a small part of the photogenerated charges can be successfully transported to the surface. Meanwhile, the unsuitable oxygen vacancies and defects in CFO APs will also lead to high charges recombination. The two reasons mentioned above result in that only few charges can participate in the photocatalytic reaction, resulting inferior photocatalytic performance for MB degradation. On the contrary, CFO NRs present features of single crystalline without grain boundary and reduced oxygen defect amount by virtue of molten salt modification, which provide free path for charges separation and transfer. These

features enable more charges in CFO NRs can participate in the photocatalytic degradation process. These successfully separated and transferred holes (h^+) and electrons (e^-) can react with H_2O and O_2 to form hydroxyl radicals (•OH) and superoxide radical ($\cdot O_2^-$), respectively. These active radicals can effectively degrade the MB solution, resulting an enhanced degradation kinetic constant compared to CFO APs.

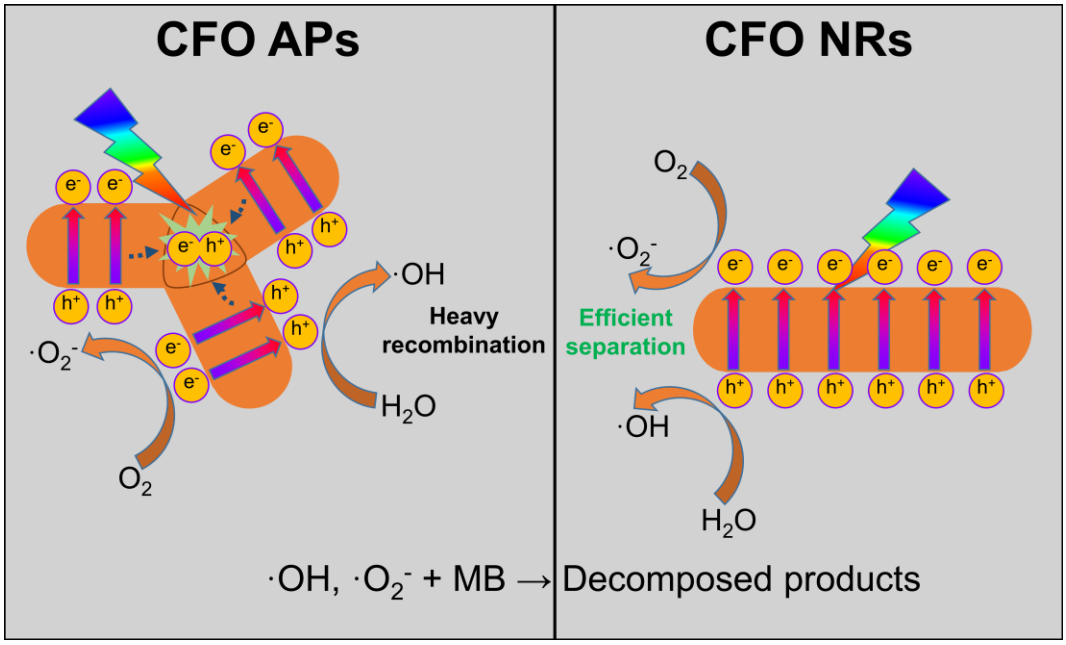

Figure 4.12 Mechanism schematic for MB photocatalytic degradation.

4.4. Conclusions

In summary, we have successfully synthesized single crystalline CFO NRs via a molten salt method for efficient photocatalytic MB degradation. CFO APs show inferior photocatalytic performance due to the plenty of grain boundaries. The molten salt-assisted modification not only change the shape of CFO NRs but also suppress the formation of grain boundaries, which are beneficial to photogenerated charges separation and transfer. In addition, the charge recombination of CFO NRs is lower than that of CFO APs based on the PL results. After shape modification, the kinetic constant of photocatalytic MB degradation for CFO NRs is 0.013 min^{-1}, which is 10 times of the kinetic constant of CFO

APs (0.0013 min^{-1}). This study also provides a feasible route for efficient photocatalysts fabrication by molten salt assisted shape modification method and a further understanding of the performance enhancement.

References

1. S. A. Hassanzadeh-Tabrizi, M. M. Motlagh, and S. Salahshour. Synthesis of ZnO/CuO nanocomposite immobilized on γ-Al_2O_3 and application for removal of methyl orange. *Applied Surface Science*. **2016** 237-243.
2. H. Anwer, A. Mahmood, J. Lee, et al. Photocatalysts for degradation of dyes in industrial effluents: Opportunities and challenges. *Nano Research*. **2019** (5) 955-972.
3. H. Wang, L. Zhang, Z. Chen, et al. Semiconductor heterojunction photocatalysts: Design, construction, and photocatalytic performances. *Chemical Society Reviews*. **2014** (15) 5234-5244.
4. N. Yahya, F. Aziz, N. A. Jamaludin, et al. A review of integrated photocatalyst adsorbents for wastewater treatment. *Journal of Environmental Chemical Engineering*. **2018** (6) 7411-7425.
5. A. Fujishima and K. Honda. Electrochemical photolysis of water at a semiconductor electrode. *Nature*. **1972** (5358) 37-38.
6. S. Chen, C. Li, and Z. Hou. The novel behavior of photoelectrochemical property of annealing TiO_2 nanorod arrays. *Journal of Materials Science*. **2020** (14) 5969-5981.
7. Y.-J. Lee, C.-G. Lee, J.-K. Kang, et al. Simple preparation method for styrofoam-TiO_2 composites and their photocatalytic application for dye oxidation and Cr(vi) reduction in industrial wastewater. *Environmental Science: Water Research & Technology*. **2021** (1) 222-230.
8. C. S. Lugo-Vega, B. Serrano-Rosales, and H. de Lasa. Immobilized particle coating for optimum photon and TiO_2 utilization in scaled air treatment photo reactors. *Applied Catalysis B: Environmental*. **2016** 211-223.

9. L. Guo, J. Cao, J. Zhang, et al. Photoelectrochemical CO_2 reduction by Cu_2O/Cu_2S hybrid catalyst immobilized in TiO_2 nanocavity arrays. *Journal of Materials Science*. **2019** (14) 10379-10388.
10. Y. Yang, L.-C. Yin, Y. Gong, et al. An unusual strong visible-light absorption band in red anatase TiO_2 photocatalyst induced by atomic hydrogen-occupied oxygen vacancies. *Advanced Materials*. **2018** (6) 1704479.
11. X. Y. Kong, Y. Y. Choo, S.-P. Chai, et al. Oxygen vacancy induced Bi_2WO_6 for the realization of photocatalytic CO_2 reduction over the full solar spectrum: From the UV to the NIR region. *Chemical Communications*. **2016** (99) 14242-14245.
12. T. Vijayaraghavan, S. P. Suriyaraj, R. Selvakumar, et al. Rapid and efficient visible light photocatalytic dye degradation using AFe_2O_4 (A = Ba, Ca and Sr) complex oxides. *Materials Science and Engineering: B*. **2016** 43-50.
13. K. K. Kefeni, B. B. Mamba, and T. A. M. Msagati. Application of spinel ferrite nanoparticles in water and wastewater treatment: A review. *Separation and Purification Technology*. **2017** 399-422.
14. A. Charles, M. R. Khan, K. H. Ng, et al. Facile synthesis of $CaFe_2O_4$ for visible light driven treatment of polluting palm oil mill effluent: Photokinetic and scavenging study. *Science of the Total Environment*. **2019** 522-530.
15. E. T. Anthony, I. A. Lawal, M. O. Bankole, et al. Solar active heterojunction of p-$CaFe_2O_4$/n-ZnO for photoredox reactions. *Environmental Technology & Innovation*. **2020** 101060.
16. L. Yang, S. Luo, Y. Li, et al. High efficient photocatalytic degradation of p-Nitrophenol on a unique Cu_2O/TiO_2 p-n heterojunction network catalyst. *Environmental Science & Technology*. **2010** (19) 7641-7646.

17. N. Liang, M. Wang, L. Jin, et al. Highly efficient $Ag_2O/Bi_2O_2CO_3$ p-n heterojunction photocatalysts with improved visible-light responsive activity. *ACS Applied Materials & Interfaces*. **2014** (14) 11698-11705.
18. E. S. Kim, N. Nishimura, G. Magesh, et al. Fabrication of $CaFe_2O_4$/TaON heterojunction photoanode for photoelectrochemical water oxidation. *Journal of the American Chemical Society*. **2013** (14) 5375-5383.
19. Z. Zhang and W. Wang. Solution combustion synthesis of $CaFe_2O_4$ nanocrystal as a magnetically separable photocatalyst. *Materials Letters*. **2014** 212-215.
20. J. Cao, T. Kako, P. Li, et al. Fabrication of p-type $CaFe_2O_4$ nanofilms for photoelectrochemical hydrogen generation. *Electrochemistry Communications*. **2011** (3) 275-278.
21. C. Shifu, Z. Wei, L. Wei, et al. Preparation, characterization and activity evaluation of p-n junction photocatalyst p-$CaFe_2O_4$/n-Ag_3VO_4 under visible light irradiation. *Journal of Hazardous Materials*. **2009** (2) 1415-1423.
22. A. Charles and C. K. Cheng. Photocatalytic treatment of palm oil mill effluent by visible light-active calcium ferrite: Effects of catalyst preparation technique. *Journal of Environmental Management*. **2019** 404-411.
23. K. Sekizawa, T. Nonaka, T. Arai, et al. Structural improvement of $CaFe_2O_4$ by metal doping toward enhanced cathodic photocurrent. *ACS Applied Materials & Interfaces*. **2014** (14) 10969-10973.
24. B. Tan, Y. Fang, Q. Chen, et al. Preparation of a $CaFe_2O_4/ZnCo_2O_4$ composite material and its photocatalytic degradation of tetracycline. *Optical Materials*. **2020** 110470.

25. S. Vadivel, D. Maruthamani, A. Habibi-Yangjeh, et al. Facile synthesis of novel $CaFe_2O_4$/g-C_3N_4 nanocomposites for degradation of methylene blue under visible-light irradiation. *Journal of Colloid and Interface Science*. **2016** 126-136.
26. A. K. R. Police, S. Basavaraju, D. K. Valluri, et al. $CaFe_2O_4$ sensitized hierarchical TiO_2 photo composite for hydrogen production under solar light irradiation. *Chemical Engineering Journal*. **2014** 152-160.
27. E. S. Kim, H. J. Kang, G. Magesh, et al. Improved photoelectrochemical activity of $CaFe_2O_4$/$BiVO_4$ heterojunction photoanode by reduced surface recombination in solar water oxidation. *ACS Applied Materials & Interfaces*. **2014** (20) 17762-17769.
28. N. K. Veldurthi, N. KrishnaRao Eswar, S. A. Singh, et al. Cooperative effect between $BaTiO_3$ and $CaFe_2O_4$ in a cocatalyst-free heterojunction composite for improved photochemical H_2 generation. *International Journal of Hydrogen Energy*. **2018** (51) 22929-22941.
29. X. Liu, Y. Zhang, Y. Jia, et al. Visible light-responsive carbon-decorated p-type semiconductor $CaFe_2O_4$ nanorod photocatalyst for efficient remediation of organic pollutants. *Chinese Journal of Catalysis*. **2017** (10) 1770-1779.
30. A. Kajbafvala, H. Ghorbani, A. Paravar, et al. Effects of morphology on photocatalytic performance of zinc oxide nanostructures synthesized by rapid microwave irradiation methods. *Superlattices and Microstructures*. **2012** (4) 512-522.
31. C. Adán, J. Marugán, E. Sánchez, et al. Understanding the effect of morphology on the photocatalytic activity of TiO_2 nanotube array electrodes. *Electrochimica Acta*. **2016** 521-529.
32. T. Vijayaraghavan, N. Lakshmana Reddy, M. V. Shankar, et al. A co-catalyst free, eco-friendly, novel visible light absorbing iron based complex oxide nanocomposites for

enhanced photocatalytic hydrogen evolution. *International Journal of Hydrogen Energy*. **2018** (31) 14417-14426.

33. X. Liu, N. Fechler, and M. Antonietti. Salt melt synthesis of ceramics, semiconductors and carbon nanostructures. *Chemical Society Reviews*. **2013** (21) 8237-8265.
34. C.-Y. Xu, L. Zhen, R. Yang, et al. Synthesis of single-crystalline niobate nanorods via ion-exchange based on molten-salt reaction. *Journal of the American Chemical Society*. **2007** (50) 15444-15445.
35. X. Zhu, A. Yamamoto, S. Imai, et al. Facet-selective deposition of a silver-manganese dual cocatalyst on potassium hexatitanate photocatalyst for highly selective reduction of carbon dioxide by water. *Applied Catalysis B: Environmental*. **2020** 119085.
36. Y. Mao, X. Yang, W. Gong, et al. A dopant replacement-driven molten salt method toward the synthesis of sub-5-nm-sized ultrathin nanowires. *Small*. **2020** (23) 2001098.
37. Z. Li-hui and H. Qing-wei. Morphology control of α-Al_2O_3 platelets by molten salt synthesis. *Ceramics International*. **2011** (1) 249-255.
38. X. Wang, C. Hu, H. Liu, et al. Synthesis of CuO nanostructures and their application for nonenzymatic glucose sensing. *Sensors and Actuators B: Chemical*. **2010** (1) 220-225.
39. X. Liu, J. Jiang, Y. Jia, et al. p-Type $CaFe_2O_4$ semiconductor nanorods controllably synthesized by molten salt method. *Journal of Energy Chemistry*. **2016** (3) 381-386.
40. G. Fan, Z. Gu, L. Yang, et al. Nanocrystalline zinc ferrite photocatalysts formed using the colloid mill and hydrothermal technique. *Chemical Engineering Journal*. **2009** (1) 534-541.

41. S. Guo, Z. Yang, H. Zhang, et al. Enhanced photocatalytic degradation of organic contaminants over $CaFe_2O_4$ under visible LED light irradiation mediated by peroxymonosulfate. *Journal of Materials Science & Technology*. **2021** 34-43.
42. L. Guo, N. Okinaka, L. Zhang, et al. Facile synthesis of $ZnFe_2O_4/SnO_2$ composites for efficient photocatalytic degradation of methylene blue. *Materials Chemistry and Physics*. **2021** 124273.
43. M. Thommes, K. Kaneko, A. V. Neimark, et al. Physisorption of gases, with special reference to the evaluation of surface area and pore size distribution (IUPAC technical report). *Pure and Applied Chemistry*. **2015** (9-10) 1051-1069.
44. A. Bloesser, J. Timm, H. Kurz, et al. A novel synthesis yielding macroporous $CaFe_2O_4$ sponges for solar energy conversion. *Solar RRL*. **2020** (8) 1900570.
45. L. Trotochaud, S. L. Young, J. K. Ranney, et al. Nickel-iron oxyhydroxide oxygen-evolution electrocatalysts: The role of intentional and incidental iron incorporation. *Journal of the American Chemical Society*. **2014** (18) 6744-6753.
46. M. G. Ahmed, T. A. Kandiel, A. Y. Ahmed, et al. Enhanced photoelectrochemical water oxidation on nanostructured hematite photoanodes via p-$CaFe_2O_4$/n-Fe_2O_3 heterojunction formation. *The Journal of Physical Chemistry C*. **2015** (11) 5864-5871.
47. T. Yamashita and P. Hayes. Analysis of XPS spectra of Fe^{2+} and Fe^{3+} ions in oxide materials. *Applied Surface Science*. **2008** (8) 2441-2449.
48. S. K. Sundriyal and Y. Sharma. Revealing the effect of oxygen defects and morphology on Li-storage performance of calcium iron oxide. *Journal of the Electrochemical Society*. **2020** (11) 110526.
49. Y. Huang, Y. Yu, Y. Yu, et al. Oxygen vacancy engineering in photocatalysis. *Solar RRL*. **2020** (8) 2000037.

50. M. Sachs, J.-S. Park, E. Pastor, et al. Effect of oxygen deficiency on the excited state kinetics of WO_3 and implications for photocatalysis. *Chemical Science*. **2019** (22) 5667-5677.
51. S. Corby, L. Francàs, A. Kafizas, et al. Determining the role of oxygen vacancies in the photoelectrocatalytic performance of WO_3 for water oxidation. *Chemical Science*. **2020** (11) 2907-2914.
52. X. Tao, W. Shi, B. Zeng, et al. Photoinduced surface activation of semiconductor photocatalysts under reaction conditions: A commonly overlooked phenomenon in photocatalysis. *ACS Catalysis*. **2020** (10) 5941-5948.
53. P. Makuła, M. Pacia, and W. Macyk. How to correctly determine the band gap energy of modified semiconductor photocatalysts based on UV-Vis spectra. *The Journal of Physical Chemistry Letters*. **2018** (23) 6814-6817.
54. Z. Wang, J. Wang, Y. Pan, et al. Preparation and characterization of a novel and recyclable $InVO_4/ZnFe_2O_4$ composite for methylene blue removal by adsorption and visible-light photocatalytic degradation. *Applied Surface Science*. **2020** 144006.
55. Q. Wu, H. Zhang, L. Zhou, et al. Synthesis and application of $rGO/CoFe_2O_4$ composite for catalytic degradation of methylene blue on heterogeneous Fenton-like oxidation. *Journal of the Taiwan Institute of Chemical Engineers*. **2016** 484-494.

Chapter 5 Summary

5.1. General conclusions

The research topic of this dissertation is the design and modification of spinel type ferrites ($ZnFe_2O_4$ and $CaFe_2O_4$) for highly efficient photocatalytic application. A facile SCS method was used to synthesized CFO and ZFO. A heterojunction of ZFO/SnO_2 was made to enhance the photocatalytic properties of pure ZFO. A detailed study on the effect of fuels and fuel ratios on the final CFO product was performed. Moreover, a molten salt-assisted shape modification of $CaFe_2O_4$ nanorods was fabricated for highly efficient photocatalytic degradation of methylene blue.

In Chapter 2, I successfully synthesized the ZFO/SnO_2 composites through a facile solution combustion synthesis method for MB aqueous solution degradation. The characterizations of crystallite structure and morphology revealed that ZFO/SnO_2 composites showed relatively small crystallite and particle size, resulting in higher active surface area. The introduction of SnO_2 significantly improved the photocatalytic MB degradation efficiency of pure ZFO catalyst. Specifically, ZFO-SnO_2 (10%) catalyst exhibited the highest photocatalytic degradation rate constant of 0.01970 min^{-1} in the composites, approximately 3.08 and 2.64 times higher than that of single ZFO (0.00640 min^{-1}) and SnO_2 (0.00747 min^{-1}), respectively. The improvement of photocatalytic degradation performance was due to enhanced charge separation efficiency in the ZFO/SnO_2 composite based on the band alignment analysis. ZFO-SnO_2 (10%) with H_2O_2 showed the highest photo-Fenton degradation rate constant of 0.05301 min^{-1} and could remove 95.2% of MB within 60 min under irradiation. This work also provides an available strategy for constructing a ZFO based composite for high efficiency photocatalytic dye degradation.

In Chapter 3, I have successfully fabricated CFO samples using urea and glucose as

fuels, respectively. CFO-Glucose shows smaller crystallite sizes than CFO-Urea. I also fully investigated the effect of fuel ratios on the final products by SCS method using glucose as fuel. The XRD results clearly show that CFO-1.0 presents the smaller crystallite sizes. PL and XPS results show that CFO-1.0 present high separation efficiency and suitable amount of oxygen vacancy on the surface, resulting the best kinetic constant of 0.00372 min^{-1} among all CFO samples.

In Chapter 4, I have successfully synthesized single crystalline CFO NRs via a molten salt method for efficient photocatalytic MB degradation. CFO APs show inferior photocatalytic performance due to the plenty of grain boundaries. The molten salt-assisted modification not only change the shape of CFO NRs but also suppress the formation of grain boundaries, which are beneficial to photogenerated charges separation and transfer. In addition, the charge recombination of CFO NRs is lower than that of CFO APs based on the PL results. After shape modification, the kinetic constant of photocatalytic MB degradation for CFO NRs is 0.013 min^{-1}, which is 10 times of the kinetic constant of CFO APs (0.0013 min^{-1}). This study also provides a feasible route for efficient photocatalysts fabrication by molten salt assisted shape modification method and a further understanding of the performance enhancement.

5.2. Future prospects

Although some modifications have been made in improving the photocatalytic properties of ZFO and CFO for efficient dye degradation catalysts. There are also some spaces to enhance their properties, one of them is to modify the photocatalyst sample by Ag co-catalyst through photodeposition method.

5.2.1. Photo-deposition of Ag as a co-catalyst on CFO NRs

A photodeposition setup is shown in Figure 5.1. The photodeposition process as follows.

CFO NRs of 300 mg was dispersed in a sealed vial with photodeposition precursor solution (H_2O of 20 mL, methanol of 20 mL, and 0.01 M $AgNO_3$ of 10 mL). Before irradiation, the solution was bubbled with N_2 gas for 30 min to remove air and keep insert atmosphere. The deposition time is set as 12 h. After photodeposition, the product was washed with distilled water and dried in a drying oven at 50 ^oC for 12 h and named as CFO-NRs-12.

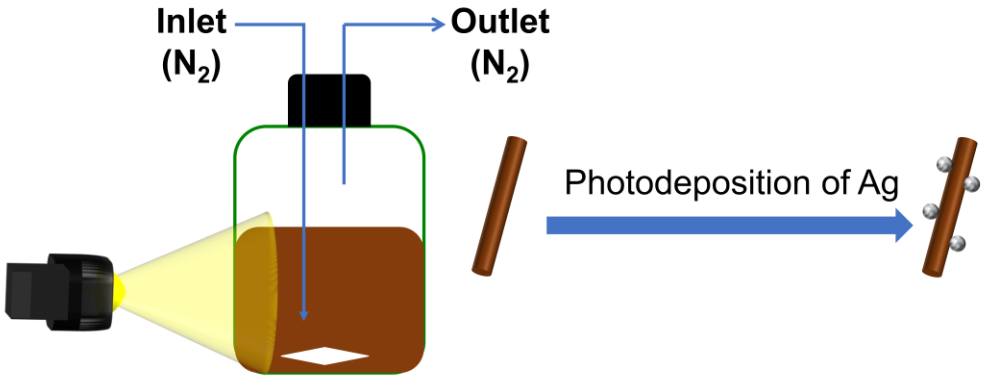

Figure 5.1 Photo-deposition of Ag on CFO NRs figure

5.2.2. Characterization of presence of Ag

Some tests are performed to show the presence of Ag on CFO-NRs by photodeposition. SEM and TEM figures were collected in Figure 5.2 and Figure 5.3, respectively. We can clearly see the presence of Ag on the CFO NRs sample. XPS data in Figure 5.4 also show the peaks from Ag. However, the amount of Ag is low. This result can also be seen from XRD figure in Figure 5.5. There are no Ag peaks shown in CFO-NRs-12 sample. However, there is no obvious change in the UV-Vis curves, as shown in Figure 5.6. This also means that the amount of Ag by photodeposition on CFO NRs-12 is not enough to affect the optical properties of CFO NRs-12 sample.

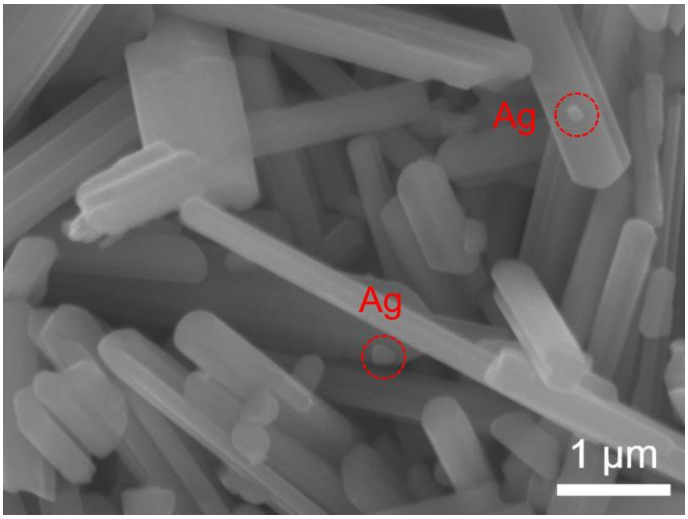

Figure 5.2 SEM figure of Ag deposited CFO NRs

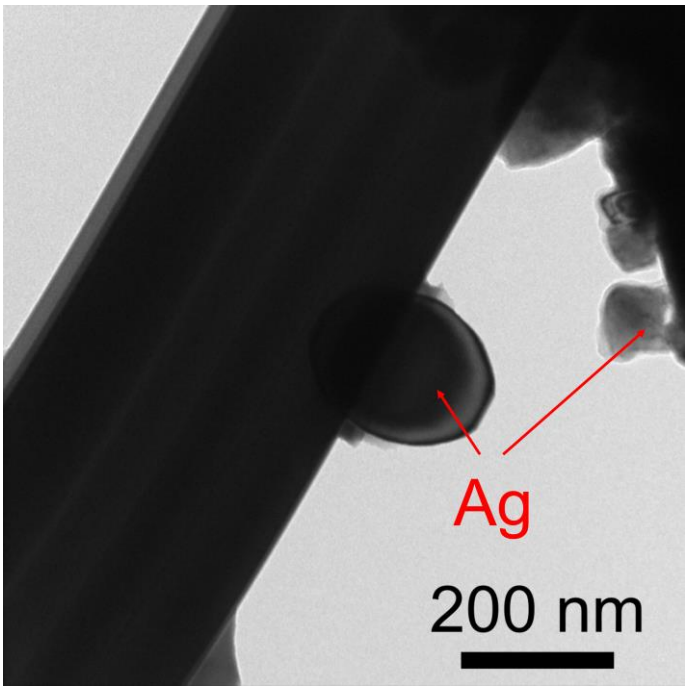

Figure 5.3 TEM figure of Ag deposited CFO NRs

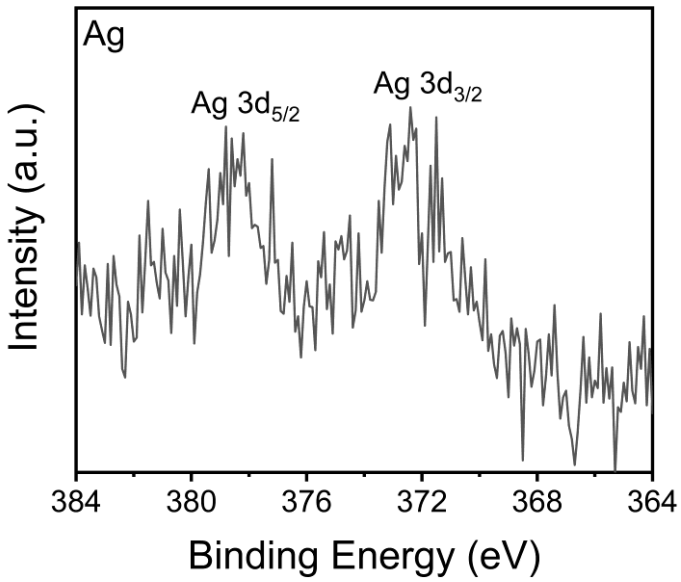

Figure 5.4 XPS of Ag deposited on CFO NRs

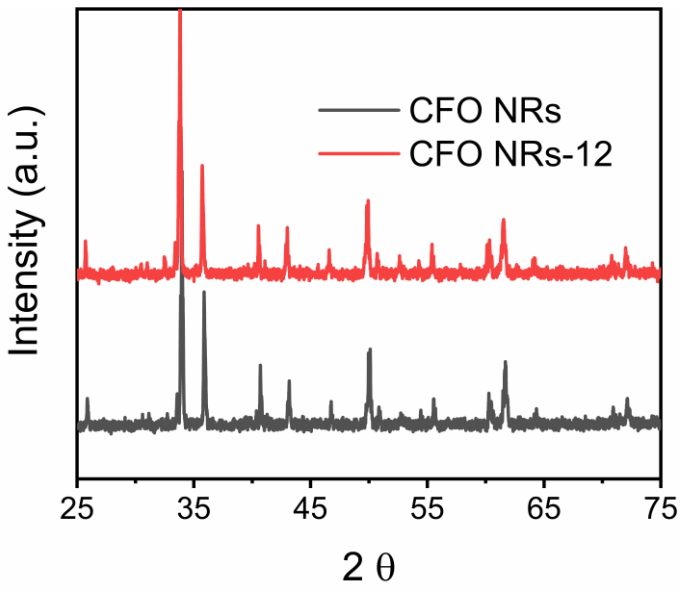

Figure 5.5 XRD patterns of CFO-NRs and CFO-NRs-12

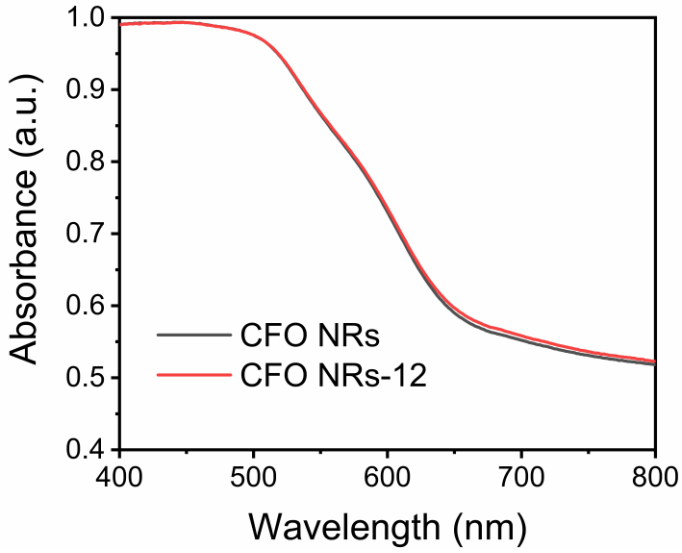

Figure 5.6 UV-Vis of CFO NRs and CFO NRs-12

5.2.3. Possible solution

It is a possible method to enhance the amount of Ag deposited on CFO NRs by increasing methanol volume and irradiation time

Academic Achievements

1. Publications

[1] **L. Guo**, N. Okinaka, L. Zhang, S. Watanabe. Facile synthesis of $ZnFe_2O_4/SnO_2$ composites for efficient photocatalytic degradation of methylene blue. *Materials Chemistry and Physics*. **2021** (262) 124273.

[2] **L. Guo**, N. Okinaka, L. Zhang, S. Watanabe. Molten Salt-assisted Shape Modification of $CaFe_2O_4$ Nanorods for Highly Efficient Photocatalytic Degradation of Methylene Blue. *Optical Materials*. **2021** (119) 111295.

2. Presentations

[1] **L. Guo**, et al., "*Facile Synthesis of $ZnFe_2O_4/SnO_2$ Composite for Enhanced Photocatalytic and Photo-Fenton Reaction*" The 2019 annual winter meeting of The Iron and Steel Institute of Japan, Jan. 16-17, 2019, Hokkaido, Japan.

[2] **L. Guo**, et al., "*Facile Synthesis of $ZnFe_2O_4/SnO_2$ Composite for Enhanced Photocatalytic and Photo-Fenton Reaction*" The 2020 annual autumn meeting of The Japan Institute of Metals and Materials, Sep. 15-18, 2020, Online.

Acknowledgement

First and foremost, I would like to express my sincerest gratitude to my supervisor, Associate Prof. Noriyuki Okinaka, who introduced me into the field of photocatalysis and gave me such convenient experimental conditions and patient instruction. These allow me to have fun exploring my Ph. D program. I am grateful for the opportunity to do a Ph. D in this research group.

I would like to give a special thanks to Prof. Seiichi Watanabe who give me so many helps in paper writing and experimental analysis. He also provided ample research funding so that I could explore my experiments without any worries. I might not be able to do the experiments so smoothly without his help.

I also must thank Assistant Prof. Lihua Zhang who not only gave me detailed directions of experiments and paper writing but also offered a lot of help about my living in Japan. I am also grateful to Dr. Melbert Jeem and Dr. Shilei Zhu for their help in my experiments and paper writing. I would like to say thanks to Dr. Subing Yang for his help in experimental facilities.

I am very thankful to Mr. Keita Suzuki for his training in XPS facility, Mr. Kenji Ohkubo for his help in using SEM, Mr. Takashi Tanioka for his help in TEM facility and other technical staffs.

I also thank secretary Ms. Kishimoto Aiko and Ms. Kaori Mitomo for their attention and care regarding office matters. I would like to extend my gratitude to previous and present members in Laboratory of Photon & Thermal Conversion Materials: Yuki Takahashi, Shuntaro Murakami, Zhehan Yu, Akinori Takeda, Souta Fuji, Ryouya Hoshino, Tomoya Gotoh, Kento Hiraiwa, Jun-ichi Mizuno, Takuya Moriyama, Atsuki Toda, Yu Tanase, Mitsuru Ishiguro, Keita Omori, Junpei Tsukamura, Tomohiro Masuda, Hsueh-I Lin,

Masaya Osawa, Satoshi Takai, Ryota Noto, Yukihiro Fukushima, Kazutaro Yamazaki, Ayaka Hayano, Keisuke Abe, Tatsuya Sakai, Mahiro Nishimura, and Hiroto Miyashita.